U. S. DEPARTMENT OF COMMERCE
Charles Sawyer, Secretary
NATIONAL BUREAU OF STANDARDS
E. U. Condon, Director

JULY 1950
VOLUME • 45
NUMBER 1

JOURNAL OF RESEARCH

of the

NATIONAL BUREAU OF STANDARDS

Contents

RP		Page
2108	Calibration of precision airplane mapping cameras. Francis E. Washer and Frank A. Case. (Price 10 cents)	1
2109	A permeammeter for magnetic testing at magnetizing forces up to 300 oersteds. Raymond L. Sanford and Philip H. Winter. (Price 10 cents)	17
2110	Heat capacity of sodium between 0° and 900° C, the triple point and heat of fusion. Defoe C. Ginnings, Thomas B. Douglas, and Anne F. Ball. (Price 10 cents)	23
2111	High-temperature X-ray study of the system $Fe_3O_4-Mn_3O_4$. H. F. McMurdie, Barbara M. Sullivan, and Floyd A. Mauer. (Price 10 cents)	35
2112	A quantitative study of the carbon monoxide formed during the absorption of oxygen by alkaline pyrogallol. Marthada V. Kilday. (Price 15 cents)	43
2113	Tracing of skew rays. Donald P. Feder. (Price 5 cents)	61
2114	Strength of heat-resistant laminated plastics up to 300° C. Benjamin M. Axilrod and Martha A. Sherman. (Price 15 cents)	65
2115	Attenuation of oscillatory pressures in instrument lines. Arthur S. Iberall (Price 15 cents)	85

For sale by the Superintendent of Documents, U. S. Government Printing Office, Washington 23, D. C. • Price 75 cents
$4.50 per year on subscription

UNITED STATES GOVERNMENT PRINTING OFFICE, WASHINGTON : 1950

U. S. Department of Commerce
National Bureau of Standards

Research Paper RP2108
Volume 45, July 1950

Part of the Journal of Research of the National Bureau of Standards

Calibration of Precision Airplane Mapping Cameras

By Francis E. Washer and Frank A. Case

An instrument is described that permits the registration of all the information necessary to calibrate a precision airplane camera on a single negative. Twenty-five collimators arranged at 7.5° intervals along two meridians at right angles provide optically distant targets. These targets are photographed by means of the camera to be tested. Measurements made on the negative yield information on the equivalent focal length, distortion, resolving power, prism effect, orientation of the lines joining opposite pairs of collimation index markers, and location of the principal point. This instrument was designed and built to make the calibration of precision cameras required for all precision cameras used in Government mapping projects. A brief account of the calibration of a typical camera and a discussion of the physical significance of calibrated focal length are given.

I. Introduction

The number of precision airplane mapping cameras submitted to the National Bureau of Standards for calibration has increased steadily since the first formal specification covering this type of camera was promulgated by the United States Department of Agriculture in March 1940. [1].[1] The demand for calibration of precision mapping cameras has increased so rapidly since 1945, that new equipment [2] for this work has been developed and built to supplement the precision lens testing camera that has been in use since 1935 [3]. The precision lens testing camera was primarily developed for use in photographically determining the equivalent focal length, distortion, and resolving power of lenses mounted in barrels or shutters. The instrument was later adapted to measuring these optical quantities for lenses mounted in cameras and further to locate the principal point in airplane mapping cameras [4].

With increased volume of work, it was evident that the method of calibration involving use of the precision lens testing camera possesses several deficiencies. First, four negatives are required, the making of which is a time consuming operation. Second, different sizes and shapes of the various makes of cameras cause difficulties in mounting them for test. Third, the entire field of the camera cannot be covered with a single photograph. The new camera calibrator was therefore designed to remedy these difficulties.

Inasmuch as the optical characteristics of lenses intended for use in airplane mapping cameras can be measured on the old precision-testing camera prior to their installation in cameras, the new calibrator was designed primarily as a pointing instrument. It provides 25 beams of parallel light from known directions. The information derived from it is therefore mainly of a directional nature and includes data on the uniformity or lack of uniformity in the distortion characteristics of lens-cone combinations. It permits more rapid and accurate location of the principal point, together with a determination of the equivalent focal length of the lens as mounted in the camera. It provides quantitative information on the magnitude of the prism effect and tangential distortion. Moreover it provides all this information on a single negative, thus avoiding possible changes that result from small movements between successive exposures. It provides a more stable support for the camera during test and also greater versatility in the types of cameras that can be tested.

The scope of the present paper is limited to a description of the instrument and the instruments

[1] Figures in brackets indicate the literature references at the end of this paper.

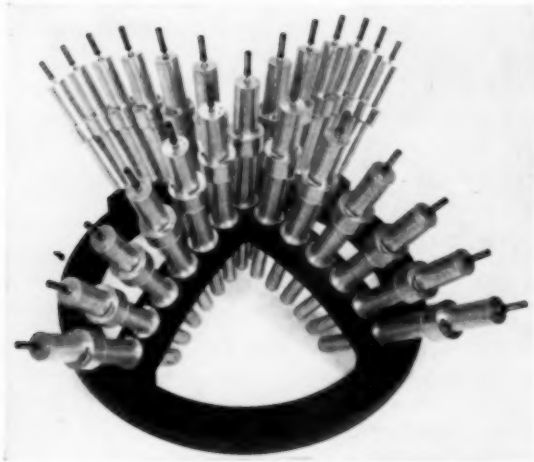

FIGURE 1. *Collimator bank of camera calibrator.*

Collimator bank before installation in the instrument. It consists of 25 collimators arranged in the form of a cross. When mounted in the camera calibrator, the central collimator points vertically upward with the remaining 24 collimators spaced at 7.5° intervals along the two meridians.

developed for use in its calibration. In addition, the calibration of a precision airplane mapping camera as conducted on the new calibrator is described. The manner of interpreting the negative is given for completeness.

II. Description of the Camera Calibrator

The camera calibrator and the details of its construction are shown in figures 1 and 2. Figure 1 shows the heart of the new instrument, which is a bank of 25 collimators arranged in the form of a cross. In use, it is mounted beneath a table as shown in figure 2. The central collimator points vertically upward, and the remaining 24 collimators are spaced at 7.5° intervals along the four arms of the cross from 0° to 45°. Departure from the 5° interval used in the Bureau's lens testing camera [3] is necessitated by space limitations. The collimators are of the fixed-focus type with the tubes cut to proper length so that each reticle lies in the focal plane of the corresponding objective. The collimators are mounted in a special casting, whose inner and outer envelopes are spherical. The collimator axes are normal to the spherical surfaces and correspondingly point toward the center of curvature. Accuracy of pointing of the collimators depends to a large extent upon the accuracy of counterbored holes and flanges by which the collimators are mounted, but the reticles may be moved about a little in the focal planes of the collimators so as to correct small deviations in the pointings. These adjustments are made with capstan screws, so arranged as to afford complete translational freedom of the reticle. After adjustments, clamping by appropriate screws guards against any subsequent movement. The clear apertures of the collimators are 18 mm in diameter, which is somewhat smaller than those of the lenses commonly used on precision mapping cameras. This, however, does not impair the instrument so far as its main purpose is concerned. To guard the collimators against disturbance the lamp housings, mounted independently on the arms of the cross, completely surround the target end of the collimators but do not touch them at any point. A 6-v. frosted flashlight bulb serves to illuminate the reticle. Provision is made for the insertion of a filter and glass diffusing screen between the lamp and the target.

The complete instrument is shown in figure 2. The table top is a flat steel plate having a large

FIGURE 2. *Camera calibrator.*

Instrument as arranged for use. The camera under test points vertically downward. Its proper orientation is effected by the autocollimating telescope and the plane-parallel piece of glass placed on the focal plane of the camera. Images on a finished negative appear every 7.5° along each diagonal, with the collimation index markers registered on each side of the negative.

circular opening in its center. The collimator bank is mounted beneath the table and centered with respect to this opening in the table top. The camera holder consists of a tripod placed over the central opening in the table. A circular opening in the center of the tripod permits the light from the 25 collimators to reach the lens of any camera placed on the holder. The focal plane of the camera can be adjusted to normality with the axis of the central collimator with the aid of the adjusting screws on the tripod and the autocollimating telescope, whose axis is bent 90° by the prism mounted in front of its objective. The adjusting screws also provide a limited amount of vertical adjustment to compensate differences in distance between the front surface of the camera lens and the front end of the camera of the various types of camera. Four flashlight bulbs mounted on adjustable arms reaching out into the circular opening of the table top serve to illuminate the collimation index markers of the camera under test.

III. Test Chart

The test charts of the new instrument include resolving power patterns, although the limited size of the collimator objectives precludes the evaluation of the resolving power of the camera lens at its maximum aperture. However, the inclusion of the chart does permit study of the resolving power at reduced aperture. Since a new test chart for use in the precision lens testing camera had been under consideration for some time, it was decided to make a new chart at this time and to use a reduced version of it as the target reticle of the camera calibrator. This new test chart is shown in figure 3. The chart was first made on a large scale and then photographed to the desired size, using Eastman high resolution plates, type 649GH. The size of the target in the 0° collimator is 8 mm square. Large scale charts are also made and subsequently reduced for each of the various angular separations from the axis, so that the cosine correction in the vertical dimensions and cosine-squared correction in the horizontal dimension of each target pattern can be made. These corrections are necessary in order that the corresponding patterns will all be imaged at the same size regardless of angular separation from the axis for a given lens-camera combination. The three-line patterns reduce in size in a geometrical progression, the ratio being $\sqrt[4]{2}$, or approximately 1.189. Closer steps in the series are admittedly desirable, for example $\sqrt[8]{2}$, but this smaller ratio could only have been achieved at the expense of compressing the range of permissible values because of the small size of the reticle. The spacings present in the patterns in the reticle range from 2.3 to 161 lines per millimeter in 26 steps. These patterns, when imaged by the lens under test, are changed by the ratio of the focal length of collimator lens and lens under test. Table 1 shows the range of resolution in the image plane for the three focal lengths most frequently encountered. The nominal maximum *f*-number of the lenses are given. Since the diameter of the collimator lens reduces the effective aperture of the lens under test, the effective operating *f*-number is given for each lens. The line showing limit of resolution shows the maximum theoretical resolving power for each lens at its effective *f*-number. With this chart therefore, the upper limit of resolution is determined by the performance of the lens and limitations of the emulsion of the photographic plate and not by insufficient range of the resolving power patterns. A considerable amount of work has been done in other laboratories, wherein a circular target is used instead of a line target.

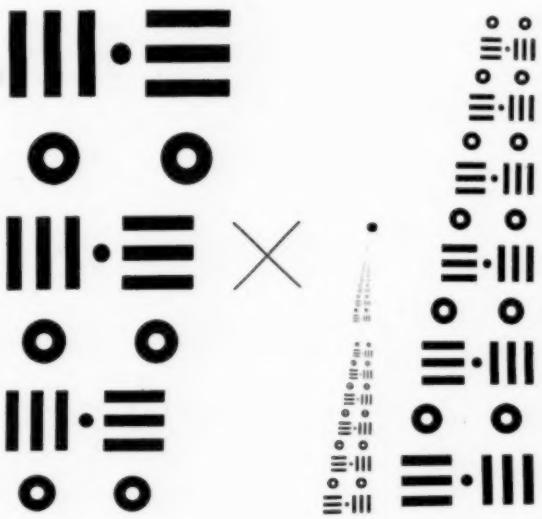

FIGURE 3. *Test chart.*

The test chart that is used in preparing the reticle for use in each collimator consists of patterns of parallel lines in two orientations with spaces varying in geometric progression by steps equal to $\sqrt[4]{2}$. The circle targets are included for comparative study of line and circle targets.

TABLE 1. *Limits placed on effective f-number by the diameter of the collimator objectives of the camera calibrator for three lenses of different focal lengths; the maximum theoretical resolution of these lenses operating at these f-numbers, and the range of the resolving powers obtainable for these different focal lengths provided by the test charts of the camera calibrator*

Equivalent focal length, mm	130	150	210
Usual nominal *f*-number	6.3	6.3	6.8
Effective *f*-number	7.2	8.3	11.7
Maximum theoretical resolution in lines per mm, as determined by effective *f*-number	198	172	122
Minimum resolution in lines per mm provided by test chart	4.7	4.1	2.9
Maximum resolution in lines per mm provided by test chart	332	289	205

A series of circular patterns is therefore included in the test chart for comparison of results obtained with it with the results obtained with the 3-line patterns.

The cross in the center of the chart is the fiducial mark with reference to which the angles separating the collimators are measured. When imaged on a camera test negative, the measured separations of the crosses for various collimators serve for the determination of equivalent focal length and distortion.

The National Bureau of Standards is at present using a high-contrast target and high-contrast fine-grained plates in the testing of photographic objectives and airplane mapping cameras. This is being done because existing Government specifications require that lenses for use in aerial mapping projects be tested under these conditions. It is recognized that there may be merit in the procedures followed in other laboratories that require the use of low-contrast targets and fast emulsions comparable to those used in actual aerial photography. Investigations are now in progress at this Bureau on the effect of contrast of target on performance of lenses. When this investigation is concluded, it is probable that a different type of target will be recommended for use in the testing of photographic objectives and cameras with corresponding changes in the required values of the resolving power for certification of lenses for Government use.

IV. Calibration of the Instrument

Adjustment of the angular relationships and measurement of the angles separating the collimators in each meridian is necessary before the instrument can be used in the calibration of precision cameras.

1. Adjustment of Angular Relationships

It is required that the angles between corresponding collimators on opposite sides of the center be as nearly equal as possible, and moreover that the axes of the beams of parallel light emerging from the collimator in a given meridian be parallel to and in near coincidence with a common plane. This adjustment is made before the collimator bank is mounted under the table. The collimator bank is placed face downward over the opening in the table top, as shown in figure 4. The lamp housings are removed to expose the target reticles. A front surface mirror is placed at the center of curvature of the spherical casting. The mirror, shown at *A*, is mounted in a special device that permits easy leveling and rotation about a horizontal axis.

A microscope equipped with a vertical illuminator is mounted over the reticle of the central collimator, and the mirror surface is brought into a position normal to the axis of the central collimator by means of the leveling screws, with the collimator, mirror, and microscope serving as an autocollimator. If now the −7.5° reticle on one side is illuminated with the desk lamp, the

FIGURE 4. *Arrangement of apparatus for adjusting the angular relationships.*

second microscope may be used to view the reticle of the +7.5° collimator on the opposite side while adjusting the reticle to bring it into coincidence with the reflected image of the −7.5° reticle. The two 7.5° angles are then equal, and the axes of the +7.5°, 0°, and −7.5° collimators fall in one plane. The microscope with the vertical illuminator is then brought over the +7.5° reticle and the mirror rotated and made normal to the axis of this collimator. The +15° and +22.5° collimators are then adjusted. The process is repeated by using the +22.5° collimator as the autocollimator to adjust the +30°, +37.5°, and +45° collimators. On returning and using the 0° collimator as autocollimator, all of the remaining collimators on the same meridian can be adjusted. Following this adjustment it can be stated that the axes of all collimators in a given meridian lie in the same plane, opposite angles are equal, and moreover angles between adjacent collimators are equal. The entire process is repeated to adjust the collimators on the meridian at right angles to the first meridian. It must be mentioned that, although the angles separating collimators along a given meridian are equal, the corresponding angles between collimators in different meridians are not exactly equal. The accuracy of the initial boring of the casting is attested by the fact that no difficulty was encountered in equalizing the angles and making the collimators coplanar, although the amount of lateral adjustment available was less than 1 mm.

2. Measurement of the Angles

The angles between adjacent collimators are determined by a comparison method using a reflecting biprism and telescope, as shown in figure 5. The standard of comparison is a biprism having a known angle between the two surfaces forming the obtuse angle. The two surfaces are aluminized and form two mirrors that maintain a constant angle with respect to one another. The angle formed between one surface and the extension of the other is 3.7600°. Ideally this angle should be one-half of the 7.5° angle between the collimators, but its present value is sufficiently close, and moreover the amount of departure from 3.75° is known. The biprism is mounted in a special device that permits rotation of the biprism about a horizontal axis coincident with the edge separating the two aluminized surfaces. As shown in figure 5, this device is mounted on the camera holder in such a manner that the edge of the biprism coincides with the center of curvature and is normal to the plane in which the collimator axes for a given meridian lie. The error that arises from unsymmetrical use of the collimator objectives is made negligibly small by the use of collimator objectives that have very small longitudinal spherical aberration and making certain that the reticles lie in the focal plane of the objectives.

To measure an angle, the telescope, equipped with a micrometer for varying its pointing, is sighted at the center line of the biprism. The biprism is rotated about its edge until the image

FIGURE 5. *Reflecting biprism for measurement of angles.*

reflected by one face of the biprism of the reticle in one collimator coincides with the cross-hairs of the viewing telescope. The lower telescope micrometer reading is recorded. The reticle of the first collimator is darkened and the second one illuminated. The image reflected by the second face of the biprism then appears in the field of view of the telescope. If the angle between collimators is exactly twice the biprism angle, no shift is evident. If the second image is shifted, the lower telescope micrometer is used to correct the pointing and the difference in micrometer reading noted. The difference in micrometer reading for the two pointings when translated into angular shift gives the difference in angle between the telescope and twice the biprism angle By rotating the biprism, the angles separating

TABLE 2. *Values of the individual angles separating adjacent collimators and their deviation from 7.5° for each collimator bank*

Collimator bank	I		II		III		IV	
Nominal angle	Angle	Deviation	Angle	Deviation	Angle	Deviation	Angle	Deviatioh
0 to 7.5	7.4963	−0.0037	7.4946	−0.0054	7.5032	+0.0032	7.5041	+0.0041
7.5 to 15	7.4972	−.0028	7.4978	−.0022	7.5038	+.0038	7.5038	+.0038
15 to 22.5	7.4985	−.0015	7.4960	−.0040	7.5061	+.0061	7.5096	+.0096
22.5 to 30	7.4937	−.0063	7.4955	−.0045	7.5021	+.0021	7.5138	+.0138
30 to 37.5	7.4940	−.0060	7.4930	−.0070	7.5069	+.0069	7.5080	+.0080
37.5 to 45	7.4981	−.0019	7.4992	−.0008	7.5070	+.0070	7.5082	+.0082

each successive collimator can be determined for all the collimators lying in the meridian. The biprism holder and viewing telescope are then rotated 90° about a vertical axis, and the above process is repeated to obtain the angular separations of the collimators in the second meridian. The measured values of the angles are given in table 2 to show the agreement between the various angles, together with their departure from 7.5°. The tolerance on angle for boring the casting was ±1 min. (±0.0167°); the table shows that the results obtained indicate the accuracy of boring was amply close.

V. Operation of the Camera Calibrator

To calibrate a camera on the instrument, one must be sure that the focal plane of the camera is normal to the axis of the central collimator. To do this the operator adjusts the micrometers on the viewing telescope until the image of the center cross on the 0° collimator coincides with the cross-hairs of the viewing telescope. The camera cone is then placed on the camera holder, adjusted laterally until the lens of the camera is coaxial with the 0° collimator. The camera is then adjusted vertically until the images formed by the outer collimators show a minimum of vignetting, the camera cone is rotated until the two diameters along which the two perpendicular rows of images fall coincide with the diagonals of the focal plane. The camera is then clamped to prevent its further motion. An optically flat plane-parallel glass plate aluminized on its upper surface, is placed on the focal plane of the camera. Then using the viewing telescope as an autocollimating telescope, the focal plane of the camera is adjusted to normality with the axis of the autocollimating telescope by small adjustments of the screws supporting the camera holder. Flashlight bulbs attached to the ends of small rods supported by the table top are then moved about until the light from the bulbs illuminate each of the four collimation index markers mounted in the camera cone. The rods are then clamped. The plane parallel is removed; the room is darkened, and a photographic plate is placed on the focal plane of the camera, and an exposure is made. It is customary to place a heavy piece of flat glass over the photographic plate during exposure to hold the plate in place and help to flatten it.

The finished negative shows the images of the targets every 7.5° from the center to the corner along each diagonal. A schematic drawing of a finished negative is shown in figure 6. The collimation markers are registered on the sides of the negative, so that there is little likelihood of the target images being fogged by the light that registers the markers.

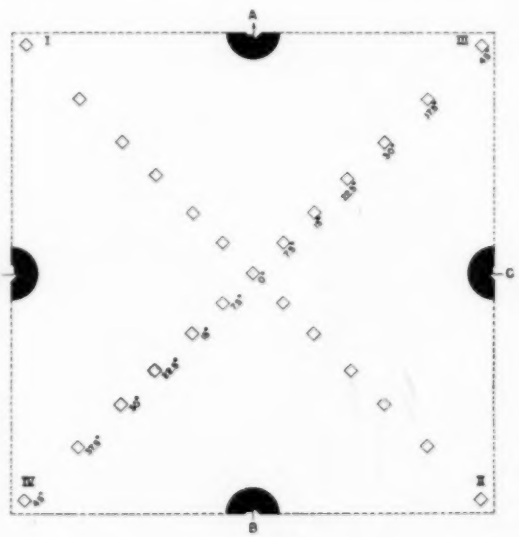

FIGURE 6. *Schematic drawing of test negative obtained with camera calibrator.*

Eastman V–G spectroscopic plates are generally used. In those instances, where a precision camera is to be used for infrared photography, Eastman IV–R spectroscopic plates are used.

VI. Calibration of a Precision Camera

Calibration of a precision camera consists of the location of the principal point with respect to the collimation index markers, determination of the angle formed by the intersection of lines joining opposite pairs of collimation index markers, determination of the equivalent focal length of the lens as mounted in the camera, determination of the distortion, and resolving power from the center to the corner of the image plane. Detail requirements relating to all these quantities are contained in specifications set up by various governmental mapping agencies concerning cameras that are to be used in Government mapping projects [5]. It is further stipulated that precision type cameras intended for use in these projects be tested for compliance with specifications by this Bureau.

It frequently happens that a camera on final examination does not comply with the requirements, but that it can be brought into compliance with the requirements by small lateral movements of the lens with respect to the collimation index markers or by small movements of the markers themselves. Following these adjustments, a recheck of the camera shows that it complies. To ensure that nothing can then happen to change this adjustment, holes are drilled and dowels placed so that the movable members remain fixed with respect to one another.

VII. Interpretation of the Negative

With the new camera calibrator, all of the information necessary to evaluate performance of the lens-cone combination is contained in a single negative. However, it is customary to make two negatives and combine the results of measurements from these to minimize any possible error. A schematic drawing of a typical negative is shown in figure 6. The markers are designated *A*, *B*, *C*, and *D* for convenience. The letter *A* is reserved for the markers bearing the arrow indicating direction of flight. The Roman numerals *I*, *II*, *III*, and *IV* serve to designate the rows of images formed by the four collimator

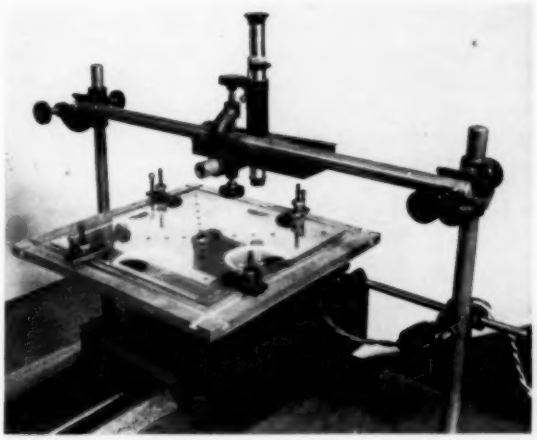

FIGURE 7. *Equipment used in the determination of the 90° condition.*

banks radiating out from the center. The central image formed by the 0° collimator is designated the center cross (*C*. *C*.). The intersection of lines joining opposite pairs of collimation index markers is designated the center of collimation, (*C* of *C*).

1. Determination of the 90° Condition

The first measurements on a given negative are made to determine whether or not the lines *AB* and *CD* are perpendicular within ±1 min. This determination is made on a special device shown in figure 7.[2] The central feature of this device consists of a piece of plate glass bearing four short radial diamond lines cut in the surface near the end of a 4.5-in. radius. The error in the positioning of the lines does not exceed ±5 sec. This plate is embedded with the lines uppermost in the metal frame that bears the plate clamps, so that the surface of the metal frame and the upper surface of the glass lie in the same plane. The negative is placed, emulsion side down, over the glass plate in such a manner that the index lines of the collimation markers and the four diamond lines are in near coincidence. The negative is then clamped down, so that no relative movement can occur during measurement. The metal frame is mounted on a spindle, so that a given marker can be brought under the viewing microscope. The separation of

[2] The authors wish to express appreciation to William P. Tayman, who developed this device for holding the 90° standard plate and the negative in contact during measurement, which represents a definite advance over the earlier equipment used in making this determination.

diamond line and index line on the negative are then measured. This process is repeated for the remaining three markers. From these four measurements, the departure and the direction of departure of the collimation index markers from the 90° condition can be determined.

2. Location of the Center Cross with Respect to the Center of Collimation

The center cross, as used herein, is the point where an infinitely distant object point lying on a line perpendicular to the focal plane is imaged by the camera lens. The coordinates of the center cross are determined with respect to the rectangular coordinate system formed by the lines joining opposite pairs of collimation index markers having the center of collimation as origin. These measurements are made with the aid of the device shown in figure 8. The negative is placed, emulsion side uppermost, upon the flat metal plate and so oriented that the line AB is approximately parallel to the bench ways upon which the slide rests. The negative is then clamped to prevent any movement with respect to the metal plate. By moving the slide along the bench ways, the measuring microscope can be set in turn on marker A, center cross, and marker B and readings taken. From this data the lateral displacement of the center cross from the line AB can be obtained. The negative is then rotated

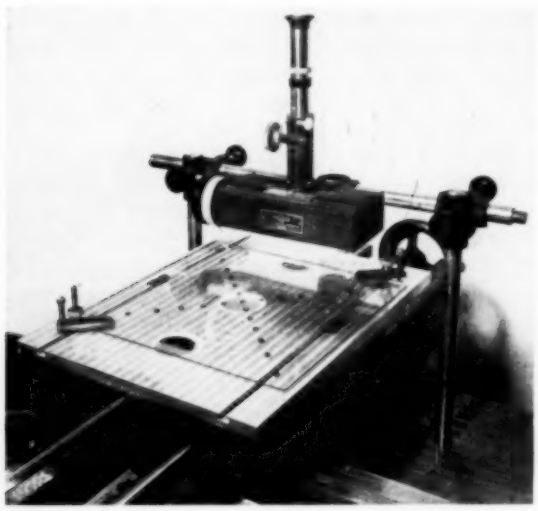

FIGURE 8. *Equipment used in locating the center cross with respect to the center of collimation.*

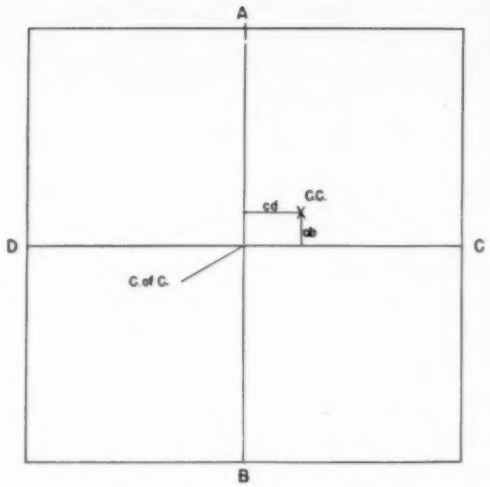

FIGURE 9. *Schematic drawing showing the center cross with respect to the center of the collimation.*

90° and similar settings made to determine the lateral displacement from the line CD. The results of measurement on a typical negative are shown schematically in figure 9. The magnitudes of the displacement are exaggerated for purposes of clarity in the figure.

3. Location of the Principal Point with Respect to the Center Cross

The principal point of precision-type aerial mapping camera is defined as that point where a perpendicular dropped from the near nodal point of the lens meets the focal plane [6]. For an ideal lens, the principal point and the center cross coincide. In practice, however, the center cross is shifted away from the principal point either because of prism effect in the lens or because of nonparallelism of the surfaces of the filter on the front of the lens, which forms a part of the optical system of the camera. This is illustrated in figure 10, which is a schematic drawing showing the displacement of the axial ray and rays inclined at angle β with the axis before and after placing a prism in front of an ideal lens.

In figure 10, O is the principal point and is the point where light from an infinitely distant object point lying on the axis of an ideal lens would be imaged if no prism effect is present. On interposing a prism having a refractive index of 1.5 and angle α the axial ray is bent away from the

normal by an amount $\epsilon_0=\alpha/2$ and now cuts the focal plane at O', which is now referred to as the center cross. To locate the position of the principal point with respect to the center cross the distance $O'O$ must be determined.

The determination of $O'O$ is made possible because the rays inclined at angle β are also displaced by amounts ϵ_1 and ϵ_2, and cut the focal plane at points X_1' and X_2' instead of X_1 and X_2. By assuming that the ray passing through the prism and meeting the focal plane at O' is near the region of minimum deviation, it follows that we may regard ϵ_1 as equal to ϵ_2 and can compute the relative magnitude of $\bar{\epsilon}$ in terms of ϵ_0. The magnitude of $\bar{\epsilon}$ is the average value of ϵ_1 and ϵ_2 and always greater than ϵ_0 and $X_2' X_2=X_1' X_1>O'O$. None of these quantities can be measured directly, but their magnitudes may be obtained as follows: From the figure,

$$O'X_2'=f[\tan(\beta+\epsilon_2)-\tan\epsilon_0]=OX_2'-O'O$$
$$O'X_1'=f[\tan(\beta-\epsilon_1)+\tan\epsilon_0]=OX_1'+O'O$$

or

$$O'X_2'=OX_2+X_2'X_2-O'O$$
$$O'X_1'=OX_1-X_1'X_1+O'O,$$

and

$$O'X_2'-O'X_1'=2(X_2'X_2-O'O)=\Delta D$$

since

$$X_2'X_2=X_1'X_1 \text{ and } OX_1=OX_2.$$

In the case of an actual lens having prism effect, X_1', O', and X_2' are the observed images and the separations $O'X_1'$ and $O'X_2'$ can be measured. Consequently, the value of ΔD can be determined for each pair of equal known angular separations from the axis from measurements on the negative. This information is used most conveniently by comparing the measured values of ΔD with values of ΔD computed for a definite set of values of prism angle, α, focal length f, and separation angle β. The computations can be readily performed and the observed values of ΔD can be interpreted in items of α sufficiently accurately by this process, because ΔD is linear in α for a fixed angle β for small value of prism angle α. Table 3 gives the computed values of $\bar{\epsilon}$, $X_2'X_2$, $O'O$, and ΔD for the case of a lens having a focal length of 150 mm combined with a prism of index 1.5 having an angle α of 0.05°. It may be noted from the table that ΔD increases rapidly with increasing β. For the case shown, ΔD is negligible at 7.5° but increases to 0.3 mm at 45°. It is evident from the table that the value of $O'O$ deduced at the wider angles is more sensitive than the value determined at the narrow angles. It is also clear that the presence of appreciably large prism effect may cause marked asymmetric distortion.

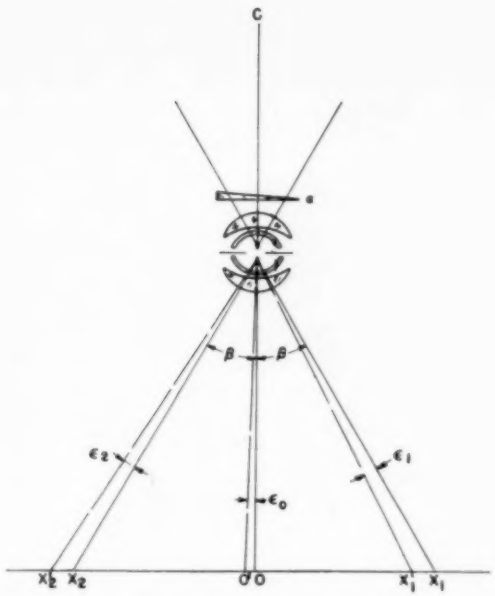

FIGURE 10. *Schematic drawing showing the image shift produced by interposing a thin prism in front of an ideal lens.*

TABLE 3. *Image displacements of various points in the focal plane for a prism of index 1.5 and angle $\alpha=0.05°$ combined with a lens whose focal length is 150 mm*

β	$\bar{\epsilon}$	$X_2'X_2=X_1'X_1$	$O'O$	$\Delta D=O'X_2'-O'X_1'$
Degrees	*Degrees*	*mm*	*mm*	*mm*
0	0.0250	0.065	0.065	0.000
7.5	.0254	.068	.065	.006
15	.0265	.074	.065	.018
22.5	.0283	.086	.065	.042
30	.0316	.110	.065	.090
37.5	.0364	.151	.065	.172
45	.0435	.228	.065	.326

Although it is feasible to determine the prism effect from a single negative from the camera calibrator by this process, it is customary to combine the results from two negatives with the camera being rotated 180° about its axis of symmetry between the marking of each negative. This procedure increases the accuracy and simpli-

fies some of the computations. The coordinates of the principal point $P.\ P.$, with respect to the center cross, are measured along the diagonals of the focal plane, as indicated in figure 11, because the calibrator is so constructed that the images from the various collimations lie along the diagonals.

4. Location of Principal Point with Respect to Center of Collimation

To locate the principal point with respect to the center of collimation, it is only necessary to combine the results obtained in section VII, 2 and 3. Care must be taken to avoid errors in sign and to make allowance for the fact that the measurements are made in two coordinate systems rotated 45° with respect to one another. Figure 12 shows the resultant obtained by combining the measurements illustrated in figures 9 and 11.

The usual requirement in precision mapping cameras is that the principal point must not be distant from the center of collimation by more than 0.03 mm. In the event that this requirement is not met, it is customary to adjust the markers with respect to the lens until the separation of principal point and center of collimation is less than 0.03 mm. When this has been done, dowels are placed so that no relative movement of principal point and center of collimation can occur.

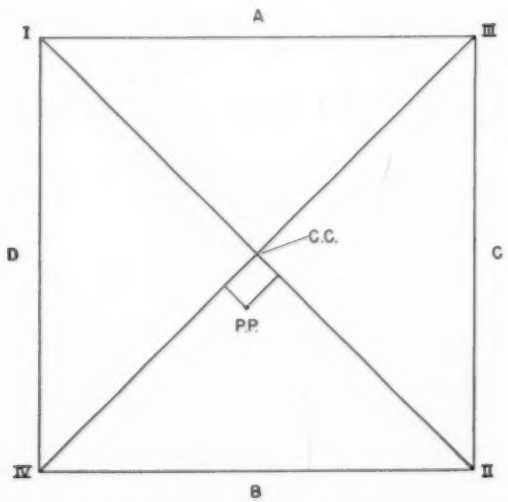

FIGURE 11. *Schematic drawing showing the principal point with respect to the center cross.*

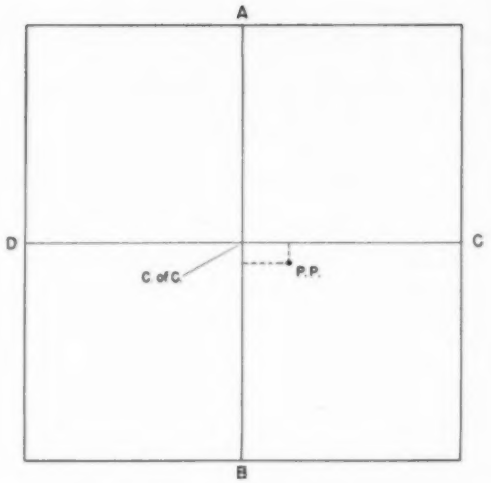

FIGURE 12. *Schematic drawing showing the principal point with respect to the center of collimation.*

5. Determination of Equivalent Focal Length and Distortion

The same negative from which the location of principal point is made is used to determine the equivalent focal length and distortion. In fact the same measurements, described in section VII, 3, for use in locating the principal point with respect to the center cross are used.

The equivalent focal length [6] is defined theoretically by the equation

$$f=\lim_{\beta\to 0}\frac{y'}{\tan\beta} \qquad (1)$$

where y' is the distance from the principal focus to the center of the image in the image space focal plane of an infinitely distant object point that lies in a direction making an angle β with the axis of the objective. If a photographic objective were free from distortion, the quotient would be invariant with respect to β. For many photographic objectives, the distortion is negligible for points distant from the center of the useful field by not more than one-fifth of its radius. Consequently, it is often possible to obtain a satisfactorily accurate value of f by a single determination of β and y' for a point lying near the axis.

The negative made for an airplane camera cone on the camera calibrator has images at the center of the field and at six known angles proceeding in 7.5° steps from the center to the edge of the useful

field. Consequently, on substituting the measured separation from the 0° to 7.5° image and the measured value of tan β into eq 1., the value of the equivalent focal length can be determined. The 0° to 7.5° separation occurs four times on the negative along radii separated by 90° of azimuth, so that four independent determinations of f are possible from a single negative. The accuracy of this determination is further increased by the fact that the measurements made on opposite sides along the same diameter automatically compensate for any error of plate tipping. It must be mentioned that practically the term equivalent focal length as used for a lens cone combination is actually the scale factor for use in interpreting distances measured on our aerial photograph in the central area. Inasmuch as photographic objectives are mounted in the aerial camera in such manner as to yield best over-all definition, it is clear that the equivalent focal length as above determined is the scale factor for the plane of best average definition.

Having established the value of the equivalent focal length for the lens camera combination, the distortion referred to the equivalent focal length can be readily found. To evaluate the distortion let y_1', y_2', y_3', . . . be the separation of the images on the negative from the central image corresponding to the angles in the object space β_1, β_2, β_3. Let products f tan β_1, f tan β_2, f tan β_3, be computed. Then the values of the distortion D_1, D_2, D_3 . . ., are given by the relation

$$D_1 = y_1' - f \tan \beta_1$$

$$D_2 = y_2' - f \tan \beta_2$$

$$D_3 = y_3' - f \tan \beta_3$$

. . . . .

Positive values of the distortion indicates a displacement of the image away from the center of the negative.

6. Determination of Calibrated Focal Length

The lenses used in aerial mapping are not free from distortion. Consequently the value of the equivalent focal length determined for the vicinity of the axis is not necessarily the best scale factor for use in interpreting measurements made on the negative at points well removed from the axial area. If one holds fast to the value of equivalent focal length determined for the axial region, the measurements made on the negative in the axial region are free from distortion, whereas in the extra-axial regions the errors from distortion may become serious.

The customary procedure for alleviating this condition is to use a new scale factor that provides a better over-all accuracy in interpreting distances measured on the negative, although it does so at the expense of introducing negligibly small errors in the axial region. This new scale factor is called the calibrated focal length [6]. The term calibrated focal length, its significance, and the manner of its evaluation have been sources of considerable misunderstanding in photogrammetric circles since the inception of the term. It is proposed in the following paragraphs to present a study of the variation of equivalent focal length and distortion that occur for a lens affected with distortion when the equivalent focal length is based on the expression

$$f = \frac{y'}{\tan \beta},$$

and β is allowed to take any value at finite intervals between 7.5° and 45°. It is hoped that careful consideration of this analysis will lead to better understanding of the physical significance of the calibrated focal length.

In table 4, the row marked y' lists the measured separations from the axial image of the images occurring at 7.5° intervals out to 45°. These measurements are from an actual negative made on a lens-cone combination. In the second row, values of f, the equivalent focal length, are given where each value of f is obtained from the equation

$$f = \frac{y'}{\tan \beta}.$$

It is clear that a different value of f is obtained for each value of β. This variation in f appears because of the distortion in the lens. It is possible to determine the values of the distortion for each of the values of f at each angular separation from the axis. This has been done, and the results are shown in the table. One of the natural consequences of this procedure is that, for whatever value of the equivalent focal length is determined, the distortion is necessarily zero for that value of β when the distortion is evaluated with respect

to that particular focal length. The location and the magnitude of the positions of maximum positive and negative values also change for each value of f. These effects are shown graphically in figure 13. It may be noted in figure 13 that the curves of distortion are very similar, and that the

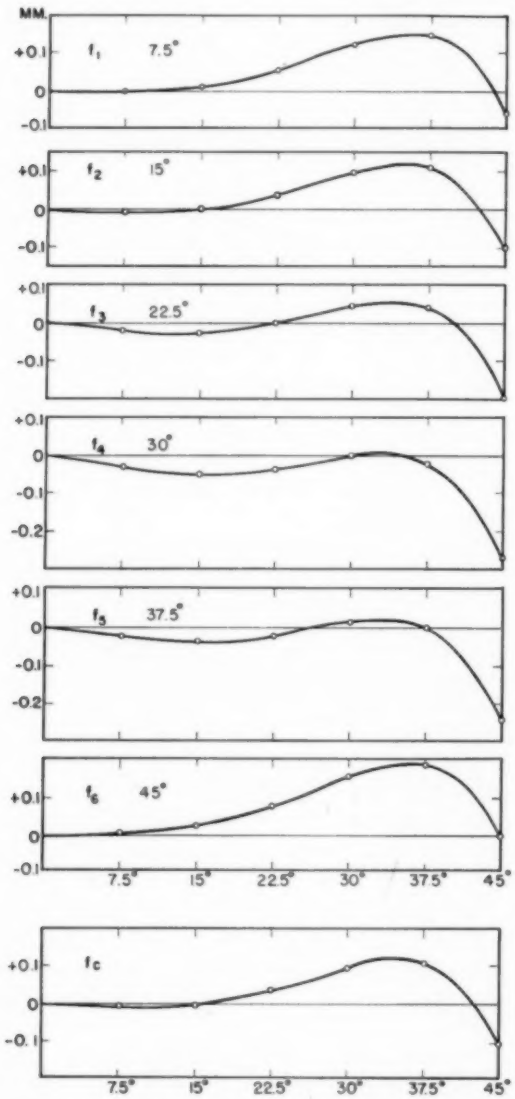

FIGURE 13. *Variation of distortion in the same image plane with equivalent focal length computed from the relation $f=y'/\tan\beta$ for varying angles of β.*

The lowest curve showing the distortion referred to the calibrated focal length indicates that the calibrated focal length is equal to the equivalent focal length for values of β of approximately 16° and 42.5°.

TABLE 4. *Variation of the values of equivalent focal length and distortion with angle upon which the computations are based for a typical lens*

	7.5°	15°	22.5°	30°	37.50°	45°
	y'_1	y'_2	y'_3	y'_4	y'_5	y'_6
y'	mm 20.064	mm 40.487	mm 62.182	mm 88.112	mm 117.086	mm 152.345
$f=\frac{y'}{\tan\beta}$	f_1 152.400	f_2 152.443	f_3 152.535	f_4 152.614	f_5 152.589	f_6 152.345
Distortion referred to the equivalent focal length $f=y'/\tan\beta$						
	7.5°	15°	22.5°	30°	37.50°	45°
f_1	0.000	0.012	0.056	0.124	0.145	−0.055
f_2	−.006	.000	.038	.099	.112	−.098
f_3	−.018	−.025	.000	.046	.042	−.190
f_4	−.028	−.046	−.033	.000	−.019	−.269
f_5	−.025	−.039	−.022	.015	.000	−.244
f_6	.007	.026	.079	.156	.188	.000
Distortion referred to the calibrated focal length f_c=152.451 mm						
f_c	0.006	−0.002	0.035	0.094	0.106	−0.106

variation of the curves is very like that which would be produced by rotating the entire curve above the 0° point.

The map maker is primarily interested in the scale factor that introduces the least error wherever used throughout the entire area of the photograph. Thus, while use of the scale factor equal to the equivalent focal length at 7.5° gives zero error within the 7.5° zone, it is at the expense of large error in the 37.5° zone. Inasmuch as there is usually no preferred area in a given photograph, it is obvious that it would be preferable to use a scale factor that would reduce error in the region of large error even if a small error were introduced in the region of zero error. Considering the curves in figure 13, it is clear that use of f_2 instead of f_1 as a scale factor will give reduced distortion in the 37.5° zone with the introduction of a small amount of distortion at 7.5°. Selection of one of the other values of f changes the error pattern either for the better or for the worse.

It is, at present, standard practice to consider the preferred error pattern as that one for which the absolute values of maximum positive and maximum negative distortion are equal. The preferred value of equivalent focal length for which

this condition prevails is called the Calibrated Focal Length. It seldom happens that the calibrated focal length coincides with the equivalent focal length at one of the fixed angles (i. e. one of the 7.5° intervals) so that it is necessary to compute the increment Δf that must be added to the equivalent focal length determined at one of the fixed angles (usually the 7.5° angle) to yield the calibrated focal length. This may be done with the aid of the following formula:

$$\Delta f = \frac{D_m + D_n}{\tan \beta_m + \tan \beta_n},$$

where D_m and D_n are the values of distortion existing at the angles β_m and β_n referred to the equivalent focal length f. The calibrated focal length f_c is then obtained from the relation

$$f_c = f + \Delta f.$$

The above formula is a general one, and the new values of distortion referred to the calibrated focal length at angles β_m and β_n are equal in magnitude and opposite in sign. Usually β_m and β_n are the angles at which maximum positive and maximum negative distortion occur. These equations are essentially the same as those reported in a paper by Sewell [8].

The values of the distortion referred to the calibrated focal length are shown in table 4 and figure 13. The computation is made for $\beta_m = 37.5°$ and $\beta_n = 45°$. It may be noted that the same value of f_c will be obtained regardless of which value of f is selected as a base of computation, so long as the corresponding values of distortion are used.

It must be emphasized that the determination of the calibrated focal length involves no shift whatever of the position of the focal plane of the camera cone with respect to the lens. The calibrated focal length is simply that value of the equivalent focal length that serves as the preferred scale factor in interpreting distances measured on the photograph.

7. Determination of the Resolving Power

The camera calibrator provides an excellent means of checking whether or not the camera lens as mounted in the camera is capable of producing usable definition from the center to each corner of the field. If, as sometimes happens, the resolution along the four radii from the center to the corners of the field is not uniformly good this will be detected on the negative and thus minimize the possibility of a camera being certified as satisfactory when the resolution satisfies minimum definition requirements along one diameter of the field but does not do so at some points along the diameter at right angles to the first. Table 5 lists the observed values of the resolving power for a typical 6-in. lens in the focal plane of the camera in which it is mounted. These resolvings powers are measured at effective aperture $f/8.3$ and may be slightly higher than the values that would be found at maximum aperature.

It is clear from this table that some variation exists in the values of the resolving power for the same angular separation from the axis on different meridians. For the lens shown, the variations are not such as to bring the resolving power down at any point to values lower than the usually specified minimum of 15 lines per millimeter for this type of lens.

TABLE 5. *Observed values of resolving power for a typical 6-in. lens as determined from a negative made with the camera calibrator*

Collimator bank	Resolving power for tangential lines in lines per millimeter with angular separation from the axis of—						
	0°	7.5°	15°	22.5°	30°	37.5°	45°
I	53	53	32	27	32	27	23
II	53	27	27	23	32	23	23
III	53	32	27	27	32	27	19
IV	53	39	27	19	27	23	23
Average	53	38	28	24	31	25	22
	Resolving power for radial lines in lines per millimeter with angular separation from the axis of—						
	0°	7.5°	15°	22.5°	30°	37.5°	45°
I	53	53	39	46	39	32	27
II	53	27	32	27	39	27	27
III	53	32	32	39	39	32	23
IV	53	39	32	32	39	32	27
Average	53	38	34	36	39	31	26

8. Flatness of Platen

The specifications for precision airplane mapping cameras [5] usually contain the requirement that the surface of the platen shall not depart from a

plane by more than ± 0.0005 in. The platen is the flat surface against which the film is pressed to ensure its planeness during the instant of exposure. This requirement is included in the specifications, because small departures from flatness in this locating surface would be imparted to the film and would in turn affect the location of images on the final negative.

It is therefore customary in the course of calibration of a precision camera to check the platen for flatness. It has not been considered expedient at this laboratory to make a detailed contour map of the entire platen surface. Instead the practice here has been to check the platen for flatness along selected lines or diameters of the platen and to conclude that the platen is satisfactorily plane if no departure from planes in excess of the specified tolerance occurs along these lines.

A simple device, shown in figure 14, has been constructed that permits a rapid measurement of the departure from flatness along a selected line with an accuracy of ± 0.0001 in. The device consists of a metal beam supported by two legs set 8 in. apart. Midway between these two legs, a sensitive dial indicator gage is mounted with the lower end of the plunger, which motivates the gage lying in the line common to the two main outer supports. The two outer supports and the central plunger have convex spherical surfaces at the lower portions, which touch the surface to be tested. The two smaller supports serve only to hold the instrument in a vertical position and to prevent the instrument from tipping over. The instrument may be rocked on the two outer legs. In use the small front leg is in contact with the surface being tested, and the movement of the plunger is in a direction closely perpendicular to the surface.

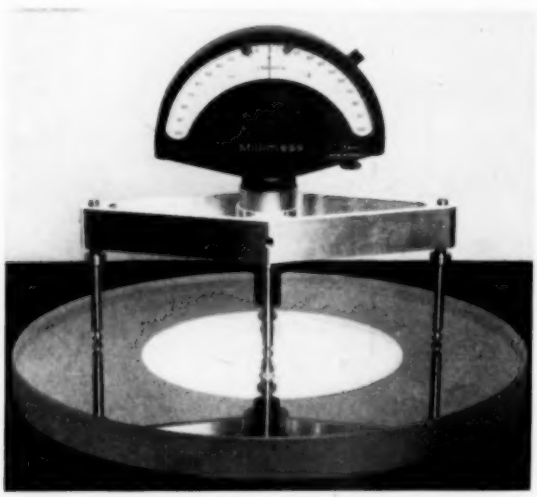

FIGURE 14. *Dial indicator device used for checking flatness of platen.*

The instrument is graduated in microns and permits the rapid measurement of departures from flatness with an accuracy of ± 0.0001 in.

The instrument is graduated in microns. Before each use, it is placed on an optical flat to ensure that the gage reads zero for a truly flat surface. It is then placed on the platen under test and the reading noted. The instrument is moved across the platen, rotated 90°, and moved across again. It is also moved about the platen in other orientations. If the pointer on the gage does not depart from zero by more than $\pm 13\mu$ during the course of this operation, the platen is adjudged satisfactory.

VIII. Discussion

The method used at this Bureau for determining the location of the principal point of airplane cameras has been in use for some years. This type of work was first performed on the precision lens testing camera and it is now being performed on the new camera calibrator. In recent years, the question has been raised whether the principal point as herein defined and determined is the proper point to use in the photogrammetric sense in the interpretation of aerial photographs. In the absence of lens distortion, particularly of the asymmetric type induced by prism effect, there can be no question of the adequacy of the method and its interpretation.

However, in the presence of unbalanced distortion, there may be some merit in the criticisms that have been directed at this concept of the principal point. It is not the aim of the present authors either to refute or concur in the various other suggested concepts of what constitutes the best definition of principal point in cameras in the presence of asymmetric distortion. Rather, these matters are included in the present paper to show that cognizance of these alternative procedures is being taken; and it is hoped that ultimately some common basis may be found wherein these differences can be reconciled.

The most recent publication dealing with one of the alternative definitions of principal point is that of P. D. Carman of the National Research Council of Canada [9]. In that paper a proof is presented that indicates that a point having properties identical with the center cross as defined in section VII, 2 of the present paper, ought to be used as the principal point. This definition of principal point is accepted in Canada as evidenced by a paper by R. H. Field [10], who describes the method of locating the principal point used at the National Research Laboratories at Ottawa.

In the September 1948 issue of Photogrammetric Engineering, E. D. Sewell [8] presents the concept of a "Point of symmetry," which is a point about which all radial distortions are to be symmetrical. This point does not coincide with either the center cross or principal point as defined in the present paper, although all three points coincide in the absence of asymmetrical distortion.

To illustrate the differing locations of these points, consider the following case. A camera whose lens showed negligible prism effect was calibrated at this laboratory and the principal point and center of collimation brought into coincidence. Following this, a thin prism was placed in front of the lens with its base facing the direction A, and a test negative was made. The center cross was found to be displaced in the direction A by 0.239 mm. The principal point, as determined by the method described in this paper, was found to coincide still with the center of collimation within ± 0.002 mm. The point of symmetry was found to be displaced in the direction A by 0.496 mm (the computation being based on targets separated 37.5° from the axis and the 0° target following the method described by Sewell). The values herein given are far greater than one likely to be found in practice, as the angle of the prism used was approximately 12 min.

It is probable that in lens-cone combinations where little asymmetric distortion exists there is little to be said in favor of any one of these concepts over the others. When appreciable asymmetric distortion is present, the authors are not in a position to state which of these points ought to be used in photo-interpretation. This must be said in favor of the principal point as located by this Bureau: It is an invariant point for a given lens-cone combination; its location is not appreciably affected by placing filters of differing prismatic power in front of the lens; it is possible that our present procedure of reporting, however, should be amended to include magnitude of the prism deviation and its direction for a given lens-cone-filter combination so that the center cross can be located by those users who prefer it in their interpretation processes.

In the opinion of the authors, there are three courses that may be followed to eliminate these difficulties. The first course is to set an upper limit to the amount of prism deviation permissible on a lens-cone combination, possibly 0.015 mm for the axial ray. A lens-cone combination that has excessive prism deviation would then be unacceptable unless it were reworked to reduce the effect. That such a course is practicable is evidenced by the discussion contained in a paper [11] by J. V. Sharp and H. H. Hayes.

The second course of action is to make accurate measurements of the prism effect, either on the lens as mounted in its camera cone or on the lens alone. Having accurate knowledge of the magnitude and direction of the prism deviation, it should then be possible to neutralize the effect by using a filter on the front of the lens, which is itself a thin prism instead of the usual plane parallel. Other researches in progress at this laboratory indicate that such a course is feasible. It is possible that small residual effects may still remain, but it is believed that such residual effects will be negligible compared to the asymmetric distortions known to be produced by the prism effect.

The third course of action resembles the first, except that an upper limit on "tangential distortion" rather than prism deviation is set. This is preferred by J. V. Sharp, because it allows for the possibility [3] of the existence of a form of "tangential distortion" that deviates from the pattern predicted by the hypothesis that tangential distortion is produced by prism effect. Even in this case it is possible that a compromise involving partial neutralization of the prism effect may be advantageous.

The authors express their appreciation to other members of the staff of the National Bureau of Standards for assistance rendered during the vari-

[3] This possibility was brought to the senior author's attention in the course of an informal discussion.

ous phases of development of this equipment. Robert E. Ward of the Instrument Shop did a major portion of the machine work and in particular performed the highly accurate boring operation on the casting that holds the collimators in alinement. George L. Buzas constructed the target holders and the devices used in calibrating the instrument. Edgar C. Watts assisted in the design of testing devices and made the drawings used in this paper. William P. Tayman made the reticles used as targets in the collimators and is the principal operator of the completed instrument. Arthur A. Magill, Roland V. Shack, Irving Malitsky, and William P. Tayman assisted in the calibration of the instrument. Wilbur W. Brannon made the biprism used for calibration of the instrument.

IX. References

[1] United States Department of Agriculture Specification No. A–APC–1102 (as approved March 1940).

[2] F. E. Washer and F. A. Case, New precision camera calibrator, NBS Technical News Bulletin **33,** 8 (1949).

[3] I. C. Gardner and F. A. Case, Precision camera for testing lenses, J. Research NBS **18,** 449 (1937) RP984.

[4] F. E. Washer, Locating the principal point of precision airplane mapping cameras, J. Research NBS **27,** 405 (1941) RP1428.

[5] Manual of Photogrammetry by the American Society of Photogrammetry, p. 130 and 136 (Pittman Publishing Corp., New York and Chicago, 1940).

[6] ASA Standard No. Z38.4.21–1948. American Standard methods of designating and measuring focal lengths and focal distances of photographic lenses.

[7] I. C. Gardner, Relation of camera error to photogrammetric mapping, J. Research NBS **22,** 209 (1939) RP1177.

[8] E. D. Sewell, Field calibration of aerial mapping cameras. Photogrammetric Engineering, XIV, 363 (1948).

[9] P. D. Carman, Photogrammetric errors from camera lens decentering, J. Opt. Soc. Am. **39,** 951 (1949).

[10] R. H. Field, A device for locating the principal point markers of air cameras, The Canadian Surveyor (July 1949). (N. R. C. No. 1979.)

[11] J. V. Sharp and H. H. Hayes, Effect on map production of distortions in photogrammetric systems, Photogrammetric Eng. **XV,** 159 (1949).

Washington, February 7, 1950.

U. S. Department of Commerce
National Bureau of Standards

Research Paper RP2109
Volume 45, July 1950

Part of the Journal of Research of the National Bureau of Standards

A Permeameter for Magnetic Testing at Magnetizing Forces up to 300 Oersteds

By Raymond L. Sanford and Philip H. Winter

A permeameter is described for magnetic testing at values of magnetizing force up to 300 oersteds. It is designed to test specimens of rectangular cross section up to 3 cm wide and 1 cm thick, with a preferred length of 28 cm. The instrument requires only a single specimen and is more simple and rapid to operate than the Burrows permeameter, which for many years has been generally accepted as the standard instrument for magnetic testing in this range. It is an absolute instrument, in that its constants are derived from its own dimensions so that it does not require calibration by any other permeameter. It is estimated that the values of magnetizing force and induction, which are obtained, are accurate within 1 percent, except that for very low values of magnetizing force the precision is the determining factor, and the uncertainty may be of the order of 0.05 oersted.

I. Introduction

For many years the Burrows Compensated Double-Yoke permeameter, either in its original form,[1] or as modified by Gokhale,[2] has been generally accepted as a standard instrument for the magnetic testing of straight bars. As it is an absolute instrument in the sense that its constants are derived from its own dimensions, it does not require calibration by reference to any other permeameter. For this reason, it has usually been employed for the calibration of test bars to be used as reference standards for calibrating and checking the performance of other permeameters.

However, the Burrows permeameter has certain disadvantages. It is somewhat complicated and tedious to operate and requires duplicate specimens, one of which is used as an auxiliary. Furthermore, it is extremely sensitive to the effect of magnetic nonuniformity along the length of the specimen which leads to errors which are indeterminate and may be large. Consequently, its use in recent years has been limited in general to the testing of magnetically uniform bars to be used as standards for calibration purposes.

For some time there has been a need for an absolute permeameter that would have an accuracy comparable with that of the Burrows instrument but which would be less complicated to operate. For this reason the development of such an instrument was undertaken. The result is the *MH* permeameter,[3] designed to operate at magnetizing forces up to 300 oersteds. It is capable of testing specimens of rectangular cross section up to 3 cm wide and 1 cm thick, with a preferred length of 28 cm, although specimens 24 cm in length can be tested satisfactorily. It is absolute in that its constants can be derived from its own dimensions, so that it does not require calibration by any other permeameter. It is estimated that values of either magnetizing force or induction can be determined to within 1 percent, except that for very low values of magnetizing force, the uncertainty due to lack of precision may be of the order of 0.05 oersted. It is simple and rapid to operate and requires only a single specimen.

II. Description of the Permeameter

The permeameter is shown in figure 1. The specimen, of rectangular cross section, is surrounded by the main magnetizing coil. The magnetic circuit is completed by symmetrical

[1] C. W. Burrows, The determination of the magnetic induction in straight bars, Bul. BS **6**, 31 (1909) S117.
[2] U. S. Patent 1,559,085 (1925).
[3] The designation M*H* stands for medium *H* (magnetizing force).

U-shaped yokes that are supported by end pieces, which in turn are supported by four Bakelite blocks. These end pieces also support the specimen and provide for close contact between the yoke and the specimen. The symmetrical yoke structure is of advantage because it promotes a uniform cross-sectional distribution of magnetic flux in the specimen. This is especially important in determining points on the hysteresis loop where the magnetizing force and the induction are in opposite directions. Auxiliary magnetizing coils are located around the ends of the yokes and supporting end pieces that make contact with the specimen. These auxiliary coils are of advantage because they promote a uniform longitudinal distribution of flux in the specimen by overcoming the contact reluctance between the specimen and the yoke. The flux distribution in the region adjacent to the center section of the bar is thereby improved, and since the value of the magnetizing force is obtained by measurements in this region, the accuracy of the measurements depends upon the degree of uniformity that can be obtained.

Values of flux-density, B, are obtained by means of a test coil surrounding the bar at the middle. An auxiliary test coil whose area-turn value is adjusted to be equal to that of the B-coil is located adjacent to the B-coil, but not surrounding the specimen, and connected in series opposing the B-coil. Thus the galvanometer deflections observed are a measure of the intrinsic flux density, B_i, rather than the total flux density. This obviates the necessity of calculating the air-flux correction for bars of different cross-sectional area.

Values of magnetizing force, H, are obtained by means of H-coils so mounted that they can be made to rotate 180° in the region adjacent to the center section of the bar. There are two H-coils mounted one above the other on a rotating brass table and adjusted to equal area-turn values. When these coils are connected in series, opposing, with their axes parallel to the specimen, and rotated through 180°, the galvanometer deflection observed is proportional to the gradient of the field with respect to the distance from the surface of the specimen, which will be referred to as the radial gradient. The value of H as measured by the deflection when only the upper coil is connected to the galvanometer is extrapolated to the surface of the specimen by using the observed value of the radial gradient.

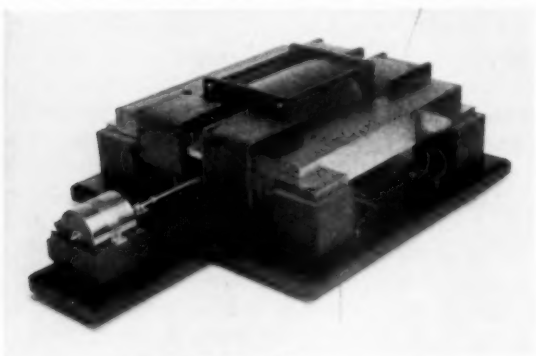

FIGURE 1. *The MH permeameter.*

The use of rotatable H-coils, or "flip-coils," has been found to have certain definite advantages over the use of stationary H-coils. Identity in the observed values of magnetizing force for both directions of the magnetizing current is a good criterion of a satisfactorily demagnetized condition. Also, values of magnetizing force for points on the hysteresis loop can be obtained by direct observation instead of by calculation in terms of the difference between two large quantities. This improves both the precision and the accuracy of the measurements.

The magnetic circuit is shown in detail in figure 2. The laminated yokes are of No. 16 gage silicon sheet of armature grade and are 4 by 5 cm in cross section. The specimen rests on end pieces that extend between the supporting Bakelite blocks. This provides a good magnetic contact between the yokes and the flat surface of the specimen at the ends. The ends of the U-shaped sections are recessed to fit over and slide on the end pieces so that contact is made at the edges of the specimen. This construction provides good contact between the yokes and the specimen without the necessity of clamping. This is an important feature, especially when strain-sensitive materials are to be tested. A supporting platform associated with the test-coil assembly prevents strains that might result from sagging of the specimen. The over-all length of the yokes is 28 cm, and the specimen is preferably of this length. However, bars as short as 24 cm can be tested if necessary.

The main magnetizing coil is 13.8 cm long, wound on a Bakelite form whose inside diameter is 7 cm. The winding is of No. 18 AWG Formex-insulated magnet wire and has 1,540 turns uniformly wound in 12 layers. The four compensat-

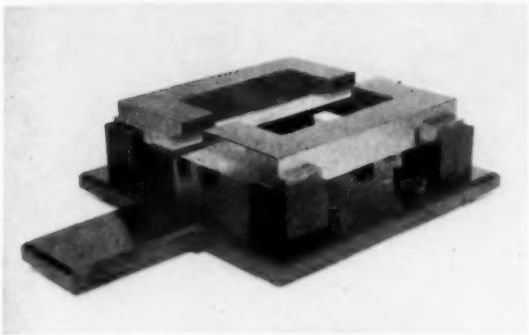

FIGURE 2. *Magnetic circuit of the MH permeameter.*

ing coils on the yokes are 5.8 cm long, and each has 430 turns of No. 18 Formex-insulated wire wound in eight layers. As it was desired to avoid the complication of having to adjust the compensating current for each point to be determined, the effect of the compensating coils on the degree of uniformity of the field adjacent to the specimen was determined for various ratios of the number of turns in the main and compensating coils. Although perfect compensation could not be obtained over the whole range for a single ratio of turns, that ratio which appeared to give the best results on the average was adopted and the coils were connected in series with the main magnetizing coil. Observations of the radial gradient were then made for different types of specimen as related to the value of magnetizing force. It was found that, within the experimental error, the percentage correction to the magnetizing force varies linearly with the permeability of the specimen, as shown in figure 3. It was also found that, although under some conditions the gradient was not quite linear, the variation from

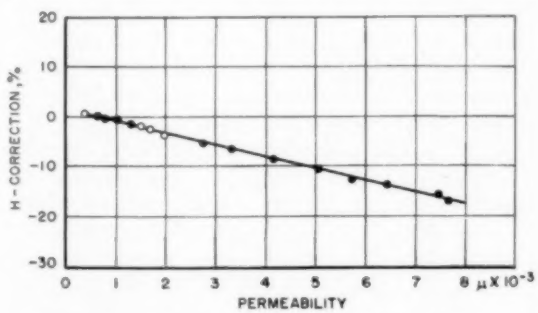

FIGURE 3. *Relation of H-correction to permeability.*

Open circles relate to cold-rolled carbon steel. Closed circles relate to silicon steel.

linearity was so small that no significant error is introduced from this cause.

The test-coil assembly is shown in figure 4. It is held in position within the main magnetizing coil form by Bakelite rings. The platform extending between these rings supports the specimen and is recessed at the middle so that the upper H coil can be located close to the surface of the specimen. The two H coils are mounted below the specimen on a small table that is rotated by a horizontal rod through a rack and pinion gear by an iron-clad solenoid and plunger located far enough away from the magnetic circuit to avoid interference. Adjustable stops limit the rotation of these "flip-coils" to 180°. The upper coil has an area-turn value of approximately 8,250 cm^2-turns. The lower coil has a slightly greater area-turn value and is shunted with a resistance so as to make its effective value equal to that of the upper coil. Each coil is approximately 2.9 cm long, 4.44 cm wide, and 1.11 cm thick. The axes of the coils are 1.11 cm apart, and the axis of the upper coil is 0.87 cm from the surface of the specimen. The windings are of No. 34 Formex-insulated magnet wire wound on Micarta forms.

The B-coil, of the same length as the H-coil, is wound on a Micarta form and surrounds the specimen. It has 100 turns of No. 31 single silk and enamel-insulated wire. The inside dimensions are such as to accommodate a specimen 3 cm wide and 1 cm thick. The compensating coil of the same area-turn value as the B-coil is mounted above it and is connected in series, opposing.

The usual switches and rheostats are employed to control the magnetizing current supplied by a storage battery. The measurements are made with a heavily overdamped ballistic galvanometer calibrated by means of a standard mutual inductor in the regular way.[4]

III. Performance

The use of a symmetrical yoke structure promotes uniformity of flux distribution, particularly across the section of the specimen. However, magnetic leakage due to the presence of joints in the magnetic circuit causes a certain lack of uniformity of the field near the surface of the specimen in the region occupied by the H-coils. Many tests were made to determine whether or

[4] NBS Circular C456, p. 23 (1946).

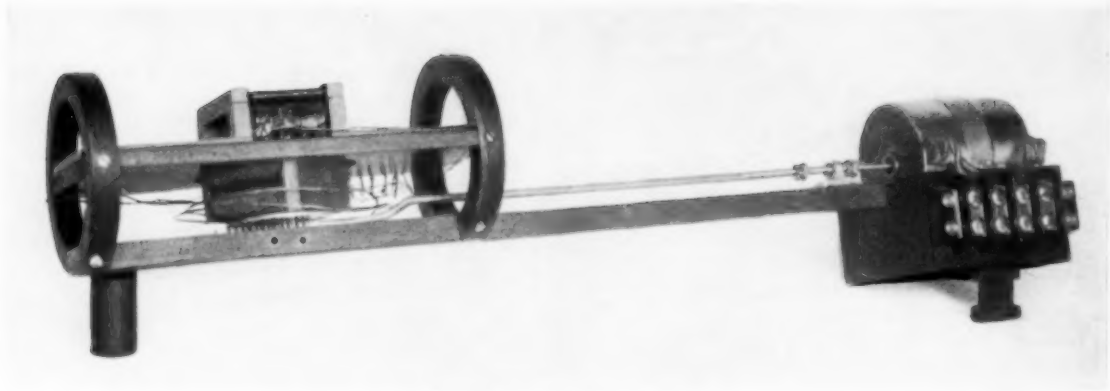

FIGURE 4. *Test-coil assembly.*

not properly located auxiliary magnetizing coils would be effective in improving the distribution. From a survey of the leakage flux around the magnetic circuit it was determined that auxiliary magnetizing coils placed on the end sections of the yokes would greatly improve the flux distribution in the region where the measurements were to be made. Distribution tests were then made with various specimens with and without the auxiliary coils. It was found that with the auxiliary coils the longitudinal distribution of the flux in the region adjacent to the center section of the specimen was uniform and, with the use of a double *H*-coil to determine the radial gradient, the value of magnetizing force at the surface of the specimen could be determined with satisfactory accuracy.

It is generally recognized that the degree of magnetic uniformity of the specimen affects the results of a magnetic test. The nature and magnitude of the effect depends not only upon the nature and magnitude of the nonuniformity but also upon the characteristics of the testing apparatus. In the M*H* permeameter, the test is limited to the middle 3 cm of the bar. It is conceivable of course that extreme nonuniformity in the part of the bar near the middle might affect the observed value of magnetizing force unduly, but such a condition is relatively rare. However, valid comparisons between permeameters that include different lengths of the specimen in the test cannot be made unless the test specimens are uniform.

A source of uncertainty often ignored, but which should not be disregarded, is the effect of mechanical strain. It is well known that the high-permeability alloys, especially in sheet form, are likely to be exceedingly sensitive to strain. However, the effect of strain in solid materials of other types is often overlooked. For instance, in a recent test of a solid bar that was not quite straight, the induction corresponding to a given value of magnetizing force could be changed by as much as 2 kilogausses by varying the clamping pressure. To avoid this uncertainty, the M*H* permeameter was so designed that good contact between the yokes and the specimen could be obtained without the necessity of clamping.

In estimating the accuracy of any permeameter, it is necessary to take into account not only the sources of error peculiar to the individual apparatus, but also those inherent in ballistic methods in general. The factors inherent in ballistic methods include the value of the mutual inductor, the area-turns of the test coils, the adjustment of the galvanometer sensitivity, ability of the galvanometer to integrate the value of a delayed impulse correctly, temperature effects, degree of uniformity of the specimen, and observation errors. The principal points peculiar to the M*H* permeameter are the distribution of the magnetic field in the space adjacent to the specimen occupied by the *H*-coils and the longitudinal and transverse distribution of the magnetic flux within the specimen.

The value of the standard mutual inductor has been determined to within ± 0.05 percent by comparison with an absolute standard of high accuracy.

The area-turns of the *H*-coil have been deter-

mined by a method previously described,[5] with an estimated accuracy of ±0.2 percent.

The current in the mutual inductor for calibrating the galvanometer is easily adjusted to within ±0.05 percent by using a potentiometer and a standard shunt.

Recent theoretical and experimental studies of the behavior of the ballistic galvanometer in use with this permeameter have shown that under the most severe conditions likely to be encountered, the galvanometer integrates correctly to within 0.1 percent.

In view of the fact that the specimen is not closely surrounded by the magnetizing coil and that the currents are relatively low, the heating is negligible under normal conditions.

With the understanding that the test results relate only to the middle 3 cm of the specimen, errors due to nonuniformity along the length of the specimen are usually of negligible magnitude.

The observational error of a single reading may be as much as 0.2 mm. However, by taking a sufficient number of readings, the probable error can be reduced to about 0.1 mm. With suitable adjustment of the galvanometer sensitivity, this will correspond to not over 0.2 percent for values of magnetizing force of 5 oersteds or over, but for values of less than 5 oersteds the precision is the determining factor and the uncertainty is of the order of 0.05 oersted. The observational error in the measurement of the induction can easily be kept within 0.2 percent by suitable adjustment of the galvanometer sensitivity.

The accuracy of the observed values of magnetizing force is limited mainly by the degree of uniformity of the field in the space occupied by the *H*-coils and adjacent to the specimen. In order to obtain a reasonable degree of precision, it was necessary to choose dimensions for the test coils that represent the best compromise between the conditions for sensitivity and for accuracy. From the results of the experimental exploration of the field, it is estimated that errors due to nonuniform distribution do not exceed 0.3 percent.

Experimental evidence indicates that the longitudinal and transverse distributions of flux within the part of the specimen covered by the *B*-coil are sufficiently uniform to make errors from this source negligible.

For purposes of comparison, normal induction and hysteresis tests were made on a tungsten steel bar about 94 cm long with a rectangular cross-sectional area of about 1.8 cm². After confirming the magnetic uniformity of the bar, it was first tested in a long solenoid and then in the M*H* permeameter. Before testing the bar in the solenoid, the distribution of flux density in the center region of the solenoid was checked, and it was found that the radial gradient of *H* was very small, so that values of *H* could be obtained with a single flat *H*-coil with an error due to this gradient of less than 0.2 percent.

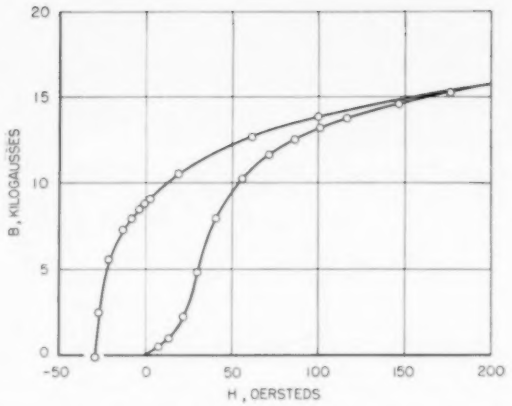

FIGURE 5. *Normal induction and hysteresis curves for tungsten-steel bar.*

Curves represent data obtained with solenoid. Check points represent data obtained with M*H* permeameter.

The curves in figure 5 are from values obtained with the solenoid, and the check points are plotted from values determined with the M*H* permeameter. A comparison of the curves and check points shows that the discrepancy between the values determined with the solenoid and M*H* permeameter is less than the observational error and well within the normal tolerance.

Considering all the probable sources of error, it is estimated that by the exercise of care in taking the readings and averaging several readings for each point, values of induction can be obtained that will be accurate to within about 0.5 percent, and values of magnetizing force can be obtained that will be accurate to within 0.5 percent, or 0.05 oersted, whichever is larger. For routine tests, values of either induction or magnetizing force accurate to within 1 percent should be obtained without difficulty.

WASHINGTON, March 9, 1950.

[5] NBS Circular C456, p. 24 (1946).

U. S. Department of Commerce
National Bureau of Standards

Research Paper RP2110
Volume 45, July 1950

Part of the Journal of Research of the National Bureau of Standards

Heat Capacity of Sodium Between 0° and 900° C, the Triple Point and Heat of Fusion

By Defoe C. Ginnings, Thomas B. Douglas, and Anne F. Ball

Using an improved ice calorimeter and furnace, the enthalpy changes of two samples of pure sodium have been accurately measured by a drop method at a number of temperatures between 0° and 900° C. Equations are derived to fit the data, and values of enthalpy and entropy, based on zero values at 0° C, as well as the heat capacity are tabulated for both the solid and liquid. Sources of significant experimental error are examined critically, and some theoretical implications of the results are discussed qualitatively.

I. Introduction

The advantages of liquid sodium for heat transfer at high temperatures have been known for some time. Not only have experimental values of the heat capacity of sodium been limited to the temperature range below 300° C, but these values have been widely discordant at 200° to 300°. It was the purpose of this investigation to measure the heat capacity of pure liquid sodium with higher accuracy and at higher temperatures than had been done previously.

II. Samples

The measurements were made on two samples of sodium enclosed in stainless steel containers of the type shown in figure 1. The stainless steel used was chosen for its resistance to attack by sodium at high temperatures. The sodium had been distilled once in glass in vacuum at or below 300° C. The weights of the samples were 5.3404 and 6.0297 g, respectively, and each was admitted in vacuum to a stainless steel cylinder weighing 16.840 g and having a capacity of 9.7 cm^3. After admitting helium to a pressure of one-thirtieth atm, each cylinder was sealed by welding and subsequently tested for leakage by noting whether exposure to 850° C for 15 min in an evacuated vessel caused any change in weight. The welding process utilized pulsed inductive heating [1].[1] With this welding technique, it was possible to seal the container without changing its weight by more than a milligram.

[1] Figures in brackets indicate the literature references at the end of this paper.

The sodium sample used for most of the measurements was analyzed spectrochemically at this Bureau after the heat-capacity experiments. Of the 47 elements tested for, including all the common metals, only three were detected. Calcium and lithium were found in amounts estimated at between 0.0001 and 0.001 weight percent, whereas potassium was estimated to be between 0.001 and 0.01 percent. The sample was completely soluble in water.

FIGURE 1. *Scale diagram of sample container.*

The spectrochemical analysis did not include a

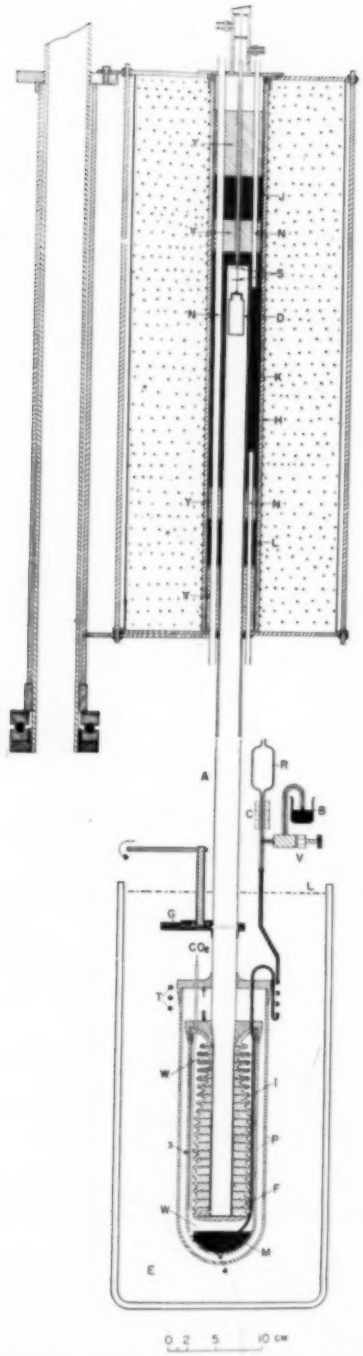

FIGURE 2. *Schematic diagram of furnace and ice calorimeter.*

A, Calorimeter well; *B*, beaker of mercury; *C*, glass capillary; *D*, sample container; *E*, ice bath; *F*, copper vanes; *G*, gate; *H*, platinum heater; *I*, ice mantel; *J*, *K*, *L*, silver cylinders; *M*, mercury; *N*, Inconel tubes; *P*, Pyrex containers; *R*, mercury reservoir; *S*, platinum shields; *T*, mercury "tempering" coil; *V*, needle valve; *W*, water; *Y*, porcelain spacers; 1, 2, 3, 4, thermocouple junctions.

search for the common nonmetals. However, other samples from the same original source and distilled by the same procedure were reported to contain as much as 0.01 percent by weight of oxygen (as Na_2O). The typical content of hydrogen before distillation amounted to 0.006 percent by weight. A melting curve observed by the authors on the principal sample is described in this paper. This indicated that the impurity in solution in the liquid but not in the solid amounted to about 0.0016 mole percent at the triple point.

III. Method and Apparatus

The method as applied to an earlier apparatus has already been described [2, 3, 4]. In brief, the method is as follows. The sample, sealed in its container, is suspended in a furnace until it comes to constant temperature. It is then dropped into a Bunsen ice calorimeter, which measures the heat evolved by the sample plus container in cooling to 0° C. A similar experiment is made with the empty container at the same temperature. The difference of the two values of heat is a measure of the change in enthalpy of the sample between 0° C and the temperature in the furnace. From enthalpy values of the sample so determined for a series of temperatures, the heat capacity can be derived.

1. The Ice Calorimeter

The construction, calibration, and use of an earlier Bunsen ice calorimeter in this Bureau have been described [2]. The present model, shown together with the furnace in figure 2, incorporates several improvements. In the first place, the mercury-water interface is now located in the bottom of the inner glass calorimeter vessel. This has two advantages. First, the area of the interface is much larger than before, so that for a given influx of heat, the level of mercury in the calorimeter changes very little. The calorimeter and its contents are slightly compressible, so that a change in pressure in the calorimeter results in a change in volume that must be distinguished from the change in volume due to heat input. With the earlier calorimeter, the change in volume produced by the change in head of mercury affected the calibration factor by about 0.01 percent, but with the present

calorimeter, the effect of the change in head is only about 0.004 percent. The electrical calibration experiments automatically compensate for this effect in heat measurements. However, reduction of the magnitude of the effect permits determination of the calibration factor of an "ideal" ice calorimeter (one that operates at constant head) with greater accuracy. A second reason for locating the mercury-water interface in the bottom of the calorimeter is to avoid danger of breaking the inner glass vessel. The inlet tube, now being filled with mercury rather than water, is not subject to blocking by freezing, an event that would burst the glass vessel. The present inlet tube includes a coil (T), for bringing the mercury to the temperature of 0° C before it enters the calorimeter.

The present calorimeter has been equipped with a tin-plated system of copper vanes, as pictured in figure 2. This results in more rapid distribution of heat from the well to the ice, so that the lag in reaching thermal equilibrium is now caused almost wholly by the thermal resistance between the heat source (sample in container) and the inner wall of the well. The latter lag has been considerably reduced by using a slow stream of dry helium gas up the well instead of carbon dioxide gas (as shown in fig. 1).

Unlike the earlier calorimeter, the new one has no built-in heater for electrical calibration. Calibrations were made with a removable heater provided with two zones of thermal contact with the calorimeter well for trapping the heat that would otherwise escape through the leads. This heater has a resistance of about 100 ohms instead of the 10 ohms in the earlier calorimeter. This reduces the uncertainty of accounting for the heat developed in the leads between the calorimeter and the jacket to a few thousandths of a percent of the total heat input to the calorimeter.

About one hundred electrical calibration experiments were made with the new calorimeter, with energies varying from 12,000 to 25,000 j. These experiments gave a calibration factor of 270.46 ± 0.03 abs j/g of mercury, which agrees with the value of 270.41 ± 0.06 obtained for the earlier calorimeter within the uncertainty assigned to the latter figure. About a hundred additional calibration experiments were made with low energies (about 100 j) in a search for small absolute errors that might not be detectable in high-energy experiments. These experiments indicated that the calorimeter failed to register about 0.4 j, an amount of heat that is negligible in most measurements.

2. The Furnace

The furnace is shown in position over the ice calorimeter in figure 2. It was mounted on a ball bearing so that it could be swung aside for access to the calorimeter. This furnace incorporated certain improvements that reduced temperature gradients in its central region and permitted more accurate temperature measurements over most of its temperature range.

In order to minimize end effects, the furnace was made 24 in. high, instead of 18 in. as with the earlier one [3]. The furnace was electrically heated by means of No. 26 platinum wire (H) wound on a grooved alundum tube having an inside diameter of 2 in. This heater was made in three separate sections corresponding in elevation to the three silver cylinders, which were located inside the alundum at J, K, and L. Silver was used because of its high thermal conductivity. By maintaining the silver cylinders J and L at the same temperature as the cylinder K, the temperature gradient in K could be made negligible. The silver cylinders were supported by porcelain spacers (Y). The silver and porcelain cylinders were lined with an Inconel tube (14% Cr, 80% Ni, 6% Fe) having an inside diameter of 1 in. in the central and lower parts of the furnace but with a diameter of one-eighth in. in the upper part. This tube served to enclose the sample container and its suspension wire (No. 32 Nichrome V), so that an inert atmosphere could be maintained at high temperatures where the stainless steel container would oxidize in air. Helium was used for the atmosphere in order to minimize the time necessary to hold the capsule in the furnace.

Figure 2 shows some of the vertical holes drilled through the silver and porcelain. These were placed 90 deg apart azimuthally. Three of them (one-fourth-in. in diameter) extended through the length of the furnace while two (three-sixteenth-in. in diameter) extended only to the top and bottom respectively of the center silver cylinder as shown in figure 2. These holes were fitted with thin-walled Inconel tubes, one of which served to hold the platinum-rhodium thermocouple sometimes used for temperature measurement of the central

silver section (K). In the two $\frac{3}{16}$-in tubes were placed differential thermocouples used to keep the end silver sections (J, L) at the same temperature as the central section. All thermocouples were insulated in four-hole porcelain tubes, which fit snugly in the Inconel tubes. A platinum resistance thermometer was encased in a platinum-rhodium tube, which also fit snugly in one of the one-fourth-in. Inconel tubes.

In another one-fourth-in. tube were placed three small auxiliary heaters, located at the elevations of the three silver cylinders. It was possible with these heaters to add heat at a low rate to any silver cylinder for fine-temperature regulation. It was possible to maintain the central silver cylinder constant to 0.01 deg and the end silver cylinders within a few tenths of a degree of the central silver. These auxiliary heaters were very useful in fine-temperature regulation since their heat was mostly delivered to the silver in 30 sec, thus avoiding the larger and troublesome lag that would have been encountered had the fine regulation been dependent on adjusting the currents in the main heaters.

In addition to the thermocouple mentioned, several more were installed just outside the main heaters (H). These thermocouples served to measure the temperature of this region and were used in a safety device to turn off automatically all current in the furnace if its temperature approached 961° C (the melting point of silver).

The suspension of the container in the furnace and its drop into the calorimeter is similar to that described earlier [3]. The braking started after the container entered the calorimeter. The weight of the falling system was kept constant in all experiments. Two platinum shields were used above the container in the same manner as formerly except that the diameters of the shields were increased from five-eighths in. to three-fourths in. since the diameter of the calorimeter well was increased from three-fourths in. to seven-eighths in.

3. Measurement of the Temperature of the Capsule in the Furnace

Up to 600° C, a strain-free platinum resistance thermometer was used to measure the temperature of the central silver cylinder that surrounded the capsule. This thermometer was calibrated at this Bureau on the International Temperature Scale [5] at the ice, steam, and sulfur points, and its resistance was always checked at the ice point after experiments at 600° C. Between 600° and 900°, the resistance thermometer was removed from the furnace, and the platinum-rhodium thermocouple was used. This thermocouple also was calibrated at this Bureau and was checked against a standard thermocouple before and after the measurements. A comparison of the resistance thermometer with the thermocouple showed agreement within 0.2 deg C in the temperature range up to 600° C. Both the resistance thermometer and thermocouple were made to have good thermal contact with the silver, so that their indications would not be affected by heat conduction along their leads. Experimental verification of this was found in tests with varying depths of immersion. The resistance thermometer winding and the principal junction of the thermocouple were both located at approximately the height of the sample container in the furnace.

It has been assumed that the sample container attains the temperature of the central silver, which surrounds it except at the bottom. Although calculations showed this assumption to be justified, experiments were made to test this. These experiments consisted of first making regular drop experiments at 700° C with the end silver pieces (J and L) regulated in the normal manner within a few tenths of a degree of the central silver (K). Then another series of drops was made, regulating both end silver pieces about 50 deg colder than the center. In other words, the temperature difference between the ends and the central silver was exaggerated by a factor of over one hundred. Even under these extreme conditions, the experiments gave a result only 0.1 percent lower. This indicated two main facts. First, with the exaggerated temperature difference, either the temperature gradient in the central silver was small, or the thermocouple was so placed that it represented the temperature of the sample container in spite of the gradient. Actually calculations show that the gradient is negligible in normal use. Second, this also indicated that any lowering of the temperature of the sample container below that of the main silver cylinder K due to radiation loss from the sample container out the bottom of the furnace is negligible. Calculations considering the solid angle had already shown that this should be true.

Since the temperature of the sample container was not directly measured, it was necessary to allow sufficient time for the container to reach the temperature of the silver. Special tests have been made to determine this time, similar to those described in detail in an earlier publication [3]. In the present experiments using helium in the furnace, the container with sodium acquired the temperature of the furnace (within 0.01 deg) within 15 min, whereas the empty container took less time in proportion to its heat capacity. In the experiments with sodium just above its melting point, extra time was taken to allow for absorption of the heat of fusion.

It was also necessary to consider the possibility of azimuthal temperature gradients in the silver due to the periodic addition of small amounts of heat by means of the auxiliary heaters that are located in one of the vertical holes in the silver. Calculations showed that no significant temperature gradients resulted with the relatively small amounts of heat supplied in this way.

4. Errors Due to Cooling of the Sample Container During Its Drop into the Calorimeter

Some users of the "drop" method in the past have simply subtracted the calculated enthalpy of the sample container from the measured enthalpy of the container plus sample. Of course, this procedure does not make allowance for heat lost during the drop. By making drop experiments with the empty container, most of this heat lost is accounted for, since it is approximately the same in both types of experiments. However, for the most accurate measurements, it is desirable to test the validity of this assumption that the heat loss is essentially the same for both empty and filled containers. The heat loss during the drop is dependent on the temperature difference between the container surface and its surroundings. This temperature difference will be slightly greater for the filled container, since its total heat capacity is higher than that of the empty container. This difference between the amounts of heat lost by the empty and the filled containers has been estimated by the authors for a sample assumed to have infinite thermal conductivity and perfect contact with the container. This gives the maximum possible difference. The radiation loss was estimated on the basis of a container with an area of 35 cm^2 with an emissivity of approximately unity. The heat lost by radiation from a container at 900° C dropping through a region near room temperature for one-quarter sec is about 80 j. The convective heat loss is much more difficult to estimate. Using the formula given in the International Critical Tables [6] for horizontal cylinders as being somewhat analogous, the convective loss in helium was calculated as about 80 j. Using these figures with the known heat capacities of the empty and filled containers, it is estimated that there would be a maximum error of about 4 j in the value for the enthalpy of the sample at 900° C. This is equivalent to about 0.06 percent on enthalpy, and a somewhat greater error on heat capacity.

Due to the approximate nature of the calculations of this error, some experiments were made to test if the heat losses calculated in this way were reasonable. Eight experiments were made at 300° C, dropping another container having about the same emissivity. In these experiments, the time of fall of the container was varied by factors of two and four greater than the normal time of fall (almost free fall). Assuming that the heat loss is directly proportional to the time of fall, it was estimated that the total heat lost in a normal fall at 300° C was about 6 j. This figure is considerably less than the value of about 16 j calculated in the manner described above (12 j by convection and 4 j by radiation). This would indicate that the heat loss is less than the calculations indicate and that at 900° C, the error due to this loss may be 0.02 to 0.03 percent. Since this error is small and is not known accurately, no attempt was made to apply a correction.

IV. Results of Enthalpy Measurements

A total of 129 measurements of enthalpy was made, 67 with the two empty containers and 62 with the two containers containing sodium. The average deviation from the mean was ± 0.02 percent with a given sample, and the difference between the values of enthalpy for the two samples did not exceed 0.3 j/g or 0.03 percent, whichever is larger. The detailed results of individual runs are given in table 1. Measurements were often repeated at lower temperatures after experiments at higher temperatures without disclosing any evidence that significant permanent changes had occurred in the samples meanwhile.

TABLE 1. *Corrected enthalpy values of individual experiments*

Temperature, t [a]	Measured heat		$(H_t-H_{0°C})$		
	Blank experiments	Experiments with sample	Observed	Calculated	Observed–Calculated
°C	*Abs j*	*Abs j*	*Abs j g⁻¹*	*Abs j g⁻¹*	
30.60	244.1	441.2	37.08	37.10	−0.02
	242.6	441.0			
	242.7	441.0			
	243.6	442.0			
59.00	474.1	862.4	72.64	72.61	+.03
	474.4	862.1			
	474.6	862.6			
	474.3	.....			
77.00	622.7	1,135.4	95.86	95.87	−.01
	623.3	1,135.2			
	623.7	1,134.9			
94.00	764.5	1,398.1	118.52	118.52	.00
	765.9	1,399.0			
	765.3	1,399.0			
	.....	[d] 1,479.2			
	.....	[d] 1,479.8			
	.....	[d] 1,479.1			
100.00	815.3	2,096.1	239.90	239.90	.00
	815.1	2,096.3			
	815.2	2,095.5			
	814.1	2,095.2			
	814.8	2,097.5			
	815.3	[d] 2,260.9			
	813.7	[d] 2,260.6			
	814.3	[d] 2,260.9			
	815.2	.....			
	[b] 814.0	.....			
	[b] 814.8	.....			
	[b] 814.6	.....			
150.00	1,241.2	2,889.0	308.48	308.47	+.01
	1,241.2	2,889.1			
	[c] 1,242.2	2,888.3			
200.00	1,676.8	3,682.2	375.84	375.95	−.11
	1,676.7	3,686.1			
	1,677.0	3,684.3			
	.....	3,683.1			
300.00	2,570.7	5,284.6	508.41	508.03	+.38
	2,570.2	5,285.5			
	2,571.7	5,285.2			
	.....	[d] 5,639.6			
	.....	[d] 5,636.7			
	.....	[d] 5,635.7			
	.....	[d] 5,636.3			
400.00	3,498.7	6,904.1	636.87	637.09	−.22
	3,496.1	6,897.2			
	[b] 3,496.9	6,901.3			
	[b] 3,507.4	6,900.0			
	[b] 3,499.0	.....			
	[b] 3,499.0	.....			
500.00	4,449.1	8,529.3	764.02	764.05	−.03
	4,449.1	8,529.2			
	4,448.3	8,528.4			
600.00	5,422.3	10,175.7	889.97	889.82	+.15
	5,423.3	10,173.3			
	5,422.2	[d] 10,791.6			
	.....	[d] 10,788.3			
	.....	[d] 10,788.8			
699.5	6,421	11,840	1,014.5	1,014.7	−.2
	6,418	11,836			
	6,430	11,837			
	.....	11,836			

See footnotes at end of table.

TABLE 1. *Corrected enthalpy values of individual experiments*—Continued

Temperature, t [a]	Measured heat		$(H_t-H_{0°C})$		
	Blank experiments	Experiments with sample	Observed	Calculated	Observed–Calculated
°C	*Abs j*	*Abs j*	*Abs j g⁻¹*	*Abs j g⁻¹*	
796.8	7,417	13,496	1,137.2	1,137.5	−.3
	7,420	13,492			
	7,417	13,491			
	[b] 7,423	.....			
	[b] 7,420	.....			
	[b] 7,422	.....			
	[b] 7,420	.....			
896.6	8,455	15,211	1,265.2	1,264.9	+.3
	8,458	15,211			
	8,454	[c] 15,210			
	[b] 8,458	[d] 16,083			
	[b] 8,453	[d] 16,080			
	[b] 8,453	.....			
	[b] 8,448	.....			
	[b] 8,449	.....			
	[b] 8,449	.....			
	[b] 8,452	.....			

[a] International Temperature Scale of 1948 [5].
[b] On alternate container of same mass.
[c] Weighted less because of unsteady heat leak.
[d] On alternate container, containing 6.0297 g of sodium. The other container had the same mass but contained 5.3404 g of sodium.

No corrections for impurities were made, since these were believed to be much smaller than the accidental error. All weights were reduced to an in-vacuum basis. Small corrections were made to bring the results to a common basis at the listed temperatures. The values of enthalpy (H_t-H_0) given in table 1 are at the vapor pressure (saturation pressure). Small corrections were made for the thin oxide coatings that the containers acquired in the furnace, using published heat capacities of Fe and Fe_3O_4 [7]. In addition, in order to evaluate the heat capacity of the liquid alone, it was necessary to make small corrections at the highest temperatures for the heat given up in condensing the sodium vapor. These corrections, based on published vapor pressure data and the volumes of the vapor, amounted to about 0.03 percent of the enthalpy at the highest temperature. The total corrections of all kinds did not amount to more than 0.1 percent of the enthalpy.

The experimental values found for the enthalpy of sodium (at saturation pressure) in absolute joules per gram, are represented by the following empirical equations. H_0 is the enthalpy of the solid at 0°C, and t represents degrees C.

$$H_t \text{ (solid)} - H_0 \text{ (solid)} = 1.19926t + (3.247)\ (10^{-4})t^2 + (3.510)(10^{-6})t^3 \qquad (0° \text{ to } 97.80° \text{ C})$$

$$H_t \text{ (liquid)} - H_0 \text{ (solid)} = 98.973 + 1.436744t - 2.90244)\ (10^{-4})t^2 + (1.54097)\ (10^{-7})t^3 + 24000e^{-\frac{13600}{t+273}} \qquad (97.80° \text{ to } 900° \text{ C})$$

The last term of the latter equation (liquid) accounts for the difference between $H_t - H_0$ and the net heat measured. As shown by Osborne [10], this difference is equal to PV/m, where P is the vapor pressure of the sodium, V is the volume of the container, and m is the mass of sodium. In the temperature range investigated, this term reaches a maximum value of 0.02 percent at 900° C and is entirely negligible for the solid. These equations give 113.2 abs j/g as the heat of fusion at the triple point, 97.80° C.

After dropping the last term in the equation for the enthalpy of the liquid, the two preceding equations then give the measured heat differences along the saturation curve. Therefore their direct differentiation gives the heat capacities (C_s) under saturation temperature and pressure, as follows:

$$C_s \text{ (solid)} = 1.19926 + (6.494)\ (10^{-4})t + (1.0531)\ (10^{-5})t^2 \qquad (0° \text{ to } 97.80° \text{ C})$$

$$C_s \text{ (liquid)} = 1.43674 - (5.8049)\ (10^{-4})t + (4.6229)\ (10^{-7})t^2 \qquad (97.80° \text{ to } 900° \text{ C})$$

From these equations directly result the following equations for the entropy (also at saturation pressure), absolute joules g^{-1} deg K^{-1}, in excess of that at 0° C. T represents degrees Kelvin (taking 0° C = 273.16° K).

$$S_T \text{ (solid)} - S_{273.16°K} \text{ (solid)} = 4.16241 \log_{10} T - (5.1036)\ (10^{-3})\ T + (5.2656)\ (10^{-6})\ T^2 - 9.14016 \qquad (0° \text{ to } 97.80° \text{ C})$$

$$S_T \text{ (liquid)} - S_{273.16°K} \text{ (solid)} = 3.75276 \log_{10} T - (8.3303)\ (10^{-4})\ T + (2.3112)\ (10^{-7})\ T^2 - 8.67398 \qquad (97.80° \text{ to } 900° \text{ C})$$

Values of enthalpy, heat capacity, and entropy calculated from these equations for rounded temperatures are listed in table 2.

TABLE 2. *Enthalpy, specific heat, and entropy of sodium*

Temperature, t	$H_t - H_{0°C}$	C_s	$S_T - S_{273.16°K}$
°C	*abs j g⁻¹*	*abs j g⁻¹ deg⁻¹*	*abs j g⁻¹ deg⁻¹*
0	0	1.1991	0
25	30.25	1.2221	.10590
50	61.21	1.2555	.20569
75	93.26	1.3071	.30116
97.80 (solid)	123.68	1.3636	.38581
[Melting	113.2	------	*.39510*]
97.80 (liquid)	236.86	1.3845	.69090
100	239.90	1.3832	.69906
200	375.95	1.3393	1.0222
300	508.03	1.3042	1.2757
400	637.09	1.2786	1.4832
500	764.05	1.2619	1.6590
600	889.82	1.2548	1.8121
700	1,015.3	1.2569	1.9481
800	1,141.6	1.2682	2.0715
900	1,269.4	1.2887	2.1853

V. Determination of the Triple Point and the Temperature Change During Melting

In order to measure the triple point and the amount of impurities (liquid-soluble, solid-insoluble) in the sodium, a resistance thermometer (60 ohms of No. 40 enameled copper wire) was wound directly around the lower half of the sample container used in most of the enthalpy measurements. This container was raised into the furnace, and the copper resistance thermometer was then calibrated at 94° and 100° C against the platinum resistance thermometer located in the silver cylinder (K). Starting with this container and the furnace at equilibrium at 94° C, the container was heated adiabatically using the copper resistance thermometer as an electric heater and raising the temperature of the furnace at about the same rate. After an appropriate time interval the electric power was turned off, and

the container was allowed to come to a constant temperature, which was observed by the copper resistance thermometer. This cycle was repeated about 20 times, using electric power of one-fourth watt over a total heating period of 90 min. It was therefore possible to observe the relation between the temperature of the sodium and the fraction that had melted.

The temperature and fraction of the sample melted were consistent with Raoult's law within the precision of the measurements, and indicated the triple point of the sample to be 97.792° C and that of pure sodium to be 97.80°. This triple-point lowering corresponds to a liquid-soluble, solid-insoluble impurity of 0.000016 mole/gram-atom of sodium. The freezing point of pure sodium at 1-atm pressure is calculated to be 97.81° C.

VI. Effect of Mechanical State of the Solid

E. Griffiths [9] claimed that he found reproducible changes in the heat capacity of crystalline sodium amounting to as much as 1.5 percent, depending on whether in its previous heat treatment, the sample had been "quenched" or "annealed". Similar tests were made by the authors on the two sodium samples reported here, and with conditions of quenching and annealing somewhat more extreme than employed by Griffiths. The furnace temperatures used were chosen to cover the temperature range where he found the greatest difference. The results are summarized in chronological order in table 3.

The first set of experiments (Set 1) was made after freezing slowly over an interval of 1 hr and then cooling at the rate of about 5 deg/hr. Preceding the experiments in Set 2 and on the same day, the molten sample was quenched by putting its container into a tube immersed in ice. The treatments before Sets 3 and 4 were respectively similar, except that the annealing carried out on the day preceding Set 3 involved freezing the sample over a period of 3 hr and then cooling the solid to room temperature at a rate varying from 3 to 5 deg/hr. Before observing Set 5, the sample was remelted and requenched by immersing its container directly into a dry ice-acetone bath (−78° C). It was then kept at this temperature overnight until just before the experiments.

TABLE 3. *Experiments to determine the reproducibility of the mechanical state of solid sodium*

Set No.	Temperature t	Mass of Na in sample	Prior heat treatment	Measured heat (Na and container)	
				Individual experiment	Mean of set
	°C	g		abs j	abs j
1	59.00	5.3404	Annealed	860.7 861.7 863.4 862.2	862.0
2	59.00	5.3404	Quenched	864.5 862.7 863.2	863.5
3	39.90	6.0297	Annealed	619.2 615.8 616.0 616.7 617.9	617.1
4	39.90	6.0297	Quenched	616.3 616.8 616.0	616.4
5	39.90	6.0297	Requenched rapidly by dry ice	614.4 616.2 615.2 616.5	615.6

The results tabulated in table 3 indicate that the quenching and annealing treatments did not change the heat capacity of the sodium by more than 0.2 percent and that these changes seem to be accidental and within the precision of the measurements.

VII. Reliability

An index to the reproducibility, or "precision", of the enthalpy measurements is afforded by the deviations from the mean, as shown by the results of the individual measurements shown in table 1. Another index is provided by the deviations (also listed in table 1) from the smoothed values given by the empirical equations adopted. All the results for liquid sodium lead to a probable error of the mean of from 0.01 to 0.03 percent on enthalpy (depending on the temperature), and as much as 0.3 percent on the derived heat capacity values, with a somewhat increased uncertainty below 200° and above 800° C because of the difficulty of determining the derivative of an empirical function accurately near its ends. For solid sodium, the relative uncertainties become considerably greater at the low temperatures, owing to the inability to determine heats by the ice calorimeter with a precision of better than 0.4 j.

In addition, all factors suspected of contributing appreciable systematic errors were analyzed to determine their likely contributions. Direct comparisons between the platinum resistance thermometer and the platinum-rhodium thermocouple up to 600° indicated differences in temperature of from 0.0 to 0.2 deg. Calculations indicated that errors due to the very small temperature gradients inside the silver cylinder in the furnace were entirely negligible. As far as uncertainties in measuring the temperatures on the International Temperature Scale are involved, the resulting probable error [2] in the enthalpy is thought to be only about 0.02 percent between 100° and 600°, and perhaps three times this much at 900°, where it was necessary to resort to measurement using a thermocouple. As a consequence, the probable error in the heat capacity due to uncertainty in temperature measurement may be considered to lie within 0.03 percent from 100° to 600°, but may reach 0.2 percent at 900° C.

In case the sample contained 0.01 percent by weight of oxygen as sodium oxide, as discussed earlier in this report, the error in enthalpy or heat capacity due to its gradual deposition from solution as the temperature fell might be as much as 0.05 percent. A similar error would be present if the liquid sodium dissolved appreciable amounts of the steel container; but recent measurements on the solubility of iron in liquid sodium by L. F. Epstein [8], of the Knolls Atomic Power Laboratory, indicate a solubility at 900° C of 22 parts per million, which would lead to negligible error in the present measurements. The analysis of the difference between the heat lost, during the drop into the calorimeter, by the sample container and by the empty container, showed that this effect, greatest at the highest temperatures, might lead to errors of 0.03 percent on enthalpy and 0.1 percent on heat capacity at 900°. Taking due consideration of the sources of error mentioned and other less significant ones, the authors believe that the probable error of the enthalpy values of sodium reported here may be considered to be between 0.1 and 0.2 percent (except below 100°, as mentioned above), whereas the probable error of the heat capacity was similarly estimated to be between 0.3 and 0.4 percent.

One experimental check on the over-all accuracy of the apparatus in measuring enthalpy was made by measuring the heat delivered to the ice calorimeter by a Monel capsule containing water and dropping from 250° C. By thus determining in several measurements the difference in heats for two amounts of water differing by about 6 g, a value of 1042.05 abs j/g for $\alpha]_0^{250°}$ of water, defined elsewhere [10], was obtained. This figure differs by only 0.02 percent from the value of 1041.85 published in the latest report [11] on the thermal properties of water as accurately measured earlier in this laboratory with an adiabatic calorimeter.

The value found for the triple point is considered to have a probable error of 0.03 deg, dependent mostly on the uncertainty in the calibration of the copper resistance thermometer used for the measurements. A probable error of 0.3 percent is assigned to the heat of fusion. This figure is based on the estimated reliability of the enthalpy values in the neighborhood of the triple point. If all the impurity indicated by the measured melting curve were actually in liquid solution at 94°, then 0.25 percent of the sample was liquid at this temperature. In that case, the value of the enthalpy of the solid given in table 1 would be 0.2 j/g too high due to this effect, making the calculated heat of fusion 0.3 j/g too low.

VIII. Comparison with Results of Other Investigations

A number of other investigators [9, 12, 13, 14, 15, 16, 17] have made measurements of the heat capacity of solid and liquid sodium above 0° C, and most of these are shown for comparison in figure 3, where the full-line curves represent the values of the present investigation as given by the equations presented earlier in this paper. Each experimental point (NBS) given for the liquid in figure 3 was calculated from two adjacent observed enthalpies given in table 1. Rengade's [12] measurements, which made use of an ice calorimeter, extended from 15° to 100°, and although he stated that his sample was not very pure, his precision amounted to about 0.2 percent. Griffiths [9] employed a dynamic method and covered the range 0° to 140°, claiming a

[2] "Probable error" as used in the remainder of this paper includes the authors' estimate of certain systematic errors. To each factor subject to error, there was assigned a figure such that it was believed that the actual error was as likely greater as smaller than this figure. These figures were then combined statistically to yield an over-all probable error in the given experimental quantity.

886334—50——3

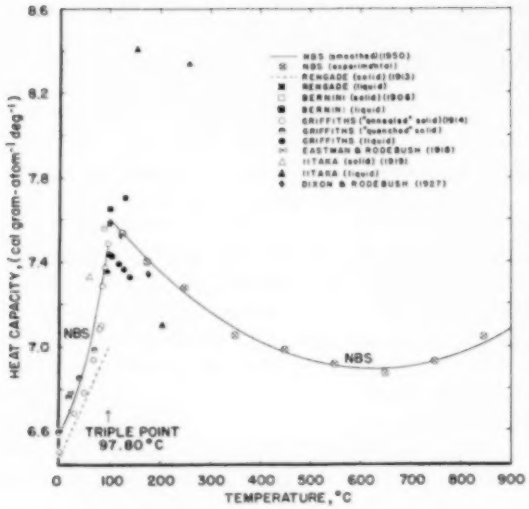

FIGURE 3. *Comparison of heat-capacity values.*

reproducibility of better than 0.1 percent, except for the variation of about 1.5 percent on the solid caused by varying the heat treatment, as mentioned above. Eastman and Rodebush's [13] measurements were mostly at low temperatures, but afford a comparison at 20° C. Iitaka [14] made determinations of the heat capacity of the liquid between 125° and 290°, the latter being the highest temperature attained prior to the present investigation. He dropped his samples from a furnace into his calorimeter and took due precaution to avoid certain systematic errors, but his precision was not better than several percent, and it will be noted from the graph that his values for heat capacity are considerably higher than those of the other investigators. Dixon and Rodebush [15] made measurements with a precision of about 1 percent, from 121° to 178°. Their method consisted in measuring the adiabatic temperature-pressure coefficient, and seems to have been subject to experimental difficulties due to the high thermal conductivity of the sodium.

The values reported for the melting point and heat of fusion of sodium are given in table 4. These melting point values in themselves are not, of course, a reliable criterion of the relative purity of the various samples used.

TABLE 4. *Values for the melting point and heat of fusion of sodium*

Source	Melting point	Heat of fusion
	°C	*abs j g*$^{-1}$
This investigation	97.81±0.03	113.2
Ladenburg and Thiele [18]	97.8 ±0.1	.....
Edmondson and Egerton [19]	97.7	.....
Tammann [18]	97.8	.....
Griffiths [9]	97.61	115.35 (113.4, less accurate)
Bridgman [20]	97.63	125.5
Rengade [12]	97.90	.....
Bernini [11]	97.63	74.5
Iitaka [14]	.....	108.8
Joannis [16]	.....	132.6

IX. Discussion of Results

The values of the heat capacity of sodium reported herein have practical importance, inasmuch as they cover the temperature range between 0° and 300° C with greater accuracy and precision than has been the case heretofore, and in addition extend the measurements to much higher temperatures, where experimental values for sodium have been entirely lacking until now. At the same time these values should be of considerable theoretical interest, since the extensive interest in the structure and properties of the liquid state in recent years has led to the theoretical calculation of the heat capacity of certain liquids, including sodium, whereas accurate experimental measurements on liquid metals have been relatively very meager.

The accuracy of the results given in this report is sufficient to show clearly the trends of the heat capacity curves of sodium with temperature, both below and above the triple point. The fall of the liquid curve to a minimum, a phenomenon in contrast to the steady rise with temperature for the great majority of liquids, is by no means unique in the case of metals, being paralleled by the heat capacity of mercury [21]. The entropy of fusion of sodium, 7.03 j deg^{-1} gram-atom^{-1}, is one of the lowest values for metals. According to current theories, the metal does not acquire complete randomness on melting, and the increased heat capacity of the liquid over what it displays at much higher temperatures is to be attributed to a further absorption of "communal" entropy above the melting point. Taking the values of the present investigation and extrapolating linearly to the melting point that part of the curve (fig. 3) above 700°, it was calculated

that the excess heat capacity between the triple point and 600° is equivalent to an entropy increase of 1.3 j deg^{-1} gram-$atom^{-1}$, a figure of the right order of magnitude to be explained in this way.

It has been pointed out further that the increase of heat capacity of the solid alkali metals with increasing temperature is enhanced in the regions of temperature just below the respective melting points, and this has been attributed to an acquisition of a part of the randomness, most of which occurs in fusion. The equation which Rengade [12] gave for the heat capacity of solid sodium from 15° to the melting point, being linear with temperature, does not of course show this feature. The equation found for the solid in this investigation, however, does have the sign of curvature just referred to, and so in this respect is at variance with an unmodified Debye function above the characteristic temperature.

Aside from any theoretical explanation of its approximate values, the heat capacity of liquid sodium is, as is well known, one of the determinants of the curvature of the vapor-pressure curve. Ladenburg and Thiele [18], in a critical evaluation of numerous vapor-pressure data of sodium, were forced to assume an average heat capacity of the liquid. Although their calculations are based on an approximate partition function for the vapor which is not accurate at these temperatures, the effect of this on the vapor pressures is probably relatively small, and they were able to show that for the range 100° to 500° C an average heat capacity of liquid sodium of 1.326 j g^{-1}, deg^{-1}, based on the measurements of Dixon and Rodebush [15], have better agreement with the vapor-pressure data and theoretically calculated "chemical constant" than a value of 1.452, the latter being Iitaka's [14] mean value. The results of the present investigation lead to an average heat capacity of 1.310 in this temperature interval.

X. Summary

The enthalpy of sodium has been measured in the range 0° to 900° C and with an accuracy of 0.1 to 0.2 percent over most of the range. Values of heat capacity are derived from the enthalpy values with an accuracy of 0.3 to 0.4 percent over most of the range. The triple point of sodium was shown to be 97.80°±0.03° C, whereas the heat of fusion is 113.2±0.4 abs j/g.

This investigation was made possible by the splendid cooperation of the Knolls Atomic Power Laboratory, Schenectady, N. Y., in preparing the samples and developing techniques of handling and sealing the samples without changing the mass of the containers. For this assistance, the authors are particularly indebted to Clifford Mannal and William D. Davis, who planned and supervised the work; and to William A. Ruggles, who was responsible for filling, sealing, and testing the sample containers.

XI. References

[1] R. J. Bondley, G. E. Research Laboratory Report No. RL–269.

[2] D. C. Ginnings and R. J. Corruccini, J. Research NBS **38,** 583 (1947) RP 1796.

[3] D. C. Ginnings and R. J. Corruccini, J. Research NBS **38,** 593 (1947) RP 1797.

[4] D. C. Ginnings and R. J. Corruccini, J. Research NBS **39,** 309 (1947) RP 1831.

[5] H. F. Stimson, J. Research NBS **42,** 209 (1949) RP 1962.

[6] International Critical Tables **5,** 234 (McGraw-Hill Book Co., New York, N. Y., 1929).

[7] K. K. Kelley, Contributions to the data on theoretical metallurgy. II. High-temperature specific-heat equations for inorganic substances. Bureau of Mines Bulletin 371. (U. S. Government Printing Office, Washington 25, D. C., 1934).

[8] Private communication.

[9] Ezer Griffiths, Proc. Roy. Soc. (London) **A89,** 561 (1914).

[10] N. S. Osborne, BS J. Research **4,** 609 (1930) RP168.

[11] N. S. Osborne, H. F. Stimson, and D. C. Ginnings, J. Research NBS **23,** 261 (1939) RP 1229.

[12] E. Rengade, Compt. Rend. **156,** 1897 (1913).

[13] E. D. Eastman and W. H. Rodebush, J. Am. Chem. Soc. **40,** 489 (1918).

[14] I. Iitaka, Sci. Reports Tohoku Imp. Univ. (Sendai) **8,** 99 (1919).

[15] A. L. Dixon and W. H. Rodebush, J. Am. Chem. Soc. **49,** 1162 (1927).

[16] A. Joannis, Ann. Chim. Phys. [7] **12,** 358 (1887).

[17] A. Bernini, Physik. Z. **7,** 168 (1906).

[18] R. Ladenburg and E. Thiele, Z. physik. Chem. **B7,** 161 (1930).

[19] W. Edmondson and A. Egerton, Proc. Roy. Soc. (London) **A113,** 521, 533 (1927).

[20] P W Bridgman, Phys. Rev. **3,** 153 (1914).

[21] T. B. Douglas, Anne F. Ball, and D. C. Ginnings, J. Research NBS (publication pending).

Washington, July 8, 1949.

U. S. Department of Commerce
National Bureau of Standards

Research Paper RP2111
Volume 45, July 1950

Part of the Journal of Research of the National Bureau of Standards

High-Temperature X-Ray Study of the System Fe_3O_4-Mn_3O_4

By H. F. McMurdie, Barbara M. Sullivan, and Floyd A. Mauer

A series of compositions in the system Fe_3O_4-Mn_3O_4 was prepared and examined at high temperatures by X-ray diffraction methods. Although Fe_3O_4 and Mn_3O_4 form a continuous series of substitutional solid solutions stable at room temperatures, those compositions containing less than 60 percent of Mn_3O_4 are cubic, of the spinel type, and the rest are tetragonal. Those compositions that are tegragonal at room temperature pass through a two-phase region when heated and acquire the cubic spinel-type structure at high temperatures. The temperature range of the two-phase (exsolution) region varies with composition. The relation to this system of the minerals vredenburgite and hausmannite is discussed.

I. Introduction

A few years ago, while the oxides of manganese were being studied in this laboratory [1],[1] it was found that Mn_3O_4, on being heated, inverts from the tetragonal structure to a cubic form of the spinel type at 1,170° C.

The low temperature form of Mn_3O_4 (hausmannite) is tetragonal, with $a=5.75$ A and $c=9.44$ A [2]. A larger unit cell, which is more readily compared in volume and atomic arrangement to that of the spinel-type [3] Mn_3O_4 obtained at higher temperatures, may be constructed by considering a equal to the diagonal of the cross section of the unit cell normal to c. When the two forms are compared in this way, it is found that the inversion involves only a slight distortion of the structure. As the change from tetragonal to cubic at 1,170° C. requires little change in structure, it is rapid and reversible as would be expected.

Since Fe_3O_4 and Mn_3O_4 are known to combine to give cubic spinel-type structures (jacobsite), the inversion of pure Mn_3O_4 described above suggests that a study of the system Fe_3O_4-Mn_3O_4 would be of interest.

II. Previous Studies

The main previous work on the system Fe_3O_4-Mn_3O_4 is that of Mason [4], from whose dissertation the diagram in figure 1 is reproduced.

[1] Figures in brackets indicate the literature references at the end of this paper.

Mason prepared a series of compounds by coprecipitating mixtures of the hydroxides of iron and manganese and heating the precipitate at approximately 1,200° C to obtain the proper state of oxidation. In this way, homogeneous preparations covering the range from 20 to 100 mole percent of Mn_3O_4 were obtained.

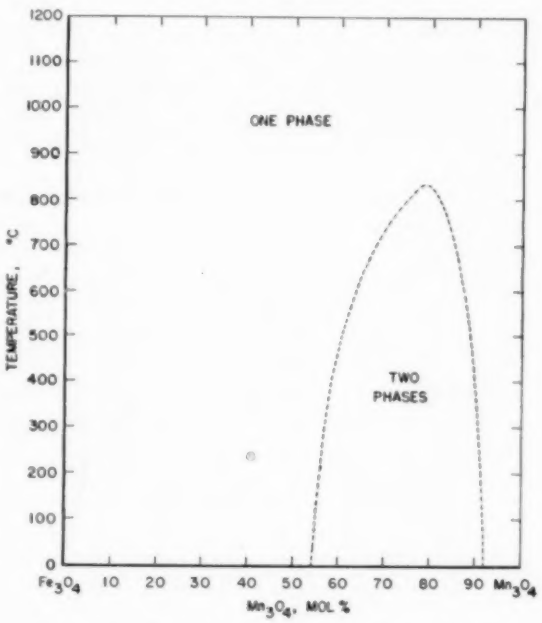

FIGURE 1. *Diagram of the system* Fe_3O_4–Mn_3O_4 *after Mason* [4].

These preparations were studied by means of powder photographs. The samples containing less than 60 percent of Mn_3O_4 gave cubic patterns, whereas those containing more than 60 percent of Mn_3O_4 were tetragonal. The tetragonal form showed a gradual increase in axial ratio with increase in manganese content. The axial ratio varied from unity (at 60 percent of Mn_3O_4) to 1.16 (for pure Mn_3O_4). Mason assumed that inasmuch as these compounds were formed near 1,200° C, they represented the conditions at that temperature and were not in equilibrium at room temperature. This interpretation seemed to be confirmed by the existence in nature of the mineral vredenburgite. This mineral has been found by X-ray diffraction and microscopy [5,6] to be composed of two phases, one cubic and the other tetragonal. The presence of these two phases indicates that the mineral is formed by exsolution. According to Mason, this two-phase mineral represents equilibrium conditions at room temperature, and on the basis of an analysis of the two phases present, he indicated an area of immiscibility in the portion of the system between 54 and 91 percent of Mn_3O_4. His approximation of the region in which exsolution would occur is outlined in figure 1. He did not indicate the position of the boundary between the cubic and the tetragonal phases in the one phase region.

In Mason's survey of the minerals comprising the system Fe_3O_4-Mn_3O_4, he fixed limits of composition for four minerals: magnetite, jacobsite, vredenburgite, and hausmannite. According to him, "Vredenburgite signifies those substances whose composition lies within the area of immiscibility, i. e., between 54 and 91 percent Mn_3O_4." The name hausmannite was given to substances in this system containing from 91 to 100 percent of Mn_3O_4. The remainder of the system, from pure Fe_3O_4 to 54 percent of Mn_3O_4, was arbitrarily divided at a composition corresponding to 50 percent of Fe_3O_4 and 50 percent of $MnFe_2O_4$, that is, at 16.7 percent of Mn_3O_4. Substances containing less than 16.7 percent of Mn_3O_4 were called magnetite, and those containing from 16.7 to 54 percent of Mn_3O_4 were designated jacobsite. The two-phase mineral vredenburgite was believed by Mason to represent equilibrium conditions at room temperature and was therefore called β-vredenburgite. The name α-vredenburgite was reserved for a high-temperature form that Mason expected to find. Later [7], he did find minerals in this range of composition that consisted of a single tetragonal phase.

Von Eckermann [8] suggested that the change from the cubic to the tetragonal structure might take place at a different composition if the temperature were increased. Basing his hypothesis on Mason's paper, and on earlier work by Montoro [9], he suggested that compositions high in Mn_3O_4 might remain tetragonal up to the melting point, whereas those richer in iron would change on heating from cubic to tetragonal at approximately 1,000° C. As Mason pointed out in a later paper [10], such a change to lower symmetry on heating seems unlikely.

When work in this laboratory disclosed that heating pure Mn_3O_4 brought about a change from the tetragonal to the cubic structure at 1,170° C, it became evident that further work was needed to clarify the picture of the high-temperature portion of the system. Because of the rapid inversions that occur in this system, it is not practical to investigate the phase relations by examination of quenched samples. High-temperature X-ray diffraction studies seemed to be the only practical method of attacking the problem, and, since suitable equipment was available [11], work was undertaken to revise the diagram of the system.

III. Method and Materials

The high-temperature X-ray diffraction apparatus described by Van Valkenburg and McMurdie [11] was employed to hold the specimens at various temperatures while the diffraction patterns were being made. Unfiltered FeK radiation was used, and the patterns were automatically recorded on a Geiger-counter spectrometer. The equipment used can record only those lines for which the Bragg angle is less than 45°. For this reason, it was not possible to determine the cell dimensions with the accuracy attained by Mason.

A series of mixtures at intervals of 5 percent by weight [2] from 60 to 100 percent of Mn_3O_4 was prepared by a method similar to that of Mason. Manganous and ferrous sulfates were weighted out in the proper proportions and dissolved. The hydroxides were coprecipitated with NaOH

[2] Although Mason's compositions are expressed in mole percent and those in this paper in weight percent, the difference in this system is very slight.

and washed by centrifuging until free from sulfates. The precipitates were then heated at 1,200° C for approximately 18 hours to convert them to the desired state of oxidation. Analysis of several of the samples for iron and manganese showed that the composition was as originally planned in each case.

X-ray diffraction patterns of each of the samples were recorded at room temperature and at various elevated temperatures. When a pattern was recorded at a high temperature, the sample was usually held at that temperature for about half an hour. Recording the pattern required about 40 minutes, after which the sample was raised to the next temperature without intermediate cooling. In a few cases samples were held at one temperature for periods up to 24 hours. The change in the relative amounts of the two phases during this period was so slight that it seemed reasonable to assume that the samples were at equilibrium when held at one temperature for half an hour.

In order to prevent oxidation of the sample at temperatures between 200° and 1,000° C, it was necessary to pass a stream of nitrogen through the furnace. In no case where nitrogen was used did lines of the higher oxide appear.

IV. Results

Table 1 shows the phases present and the unit-cell dimensions [3] for each of the samples at various temperatures. These data show that, at room temperature, each sample consists of a single phase, the one containing 60 percent of Mn_3O_4 being cubic while all others are tetragonal. When the samples containing 65 to 95 percent of Mn_3O_4

[3] As mentioned previously, a modified unit cell has been used to describe the tetragonal phase. The cell chosen facilitates comparison with spinel structures.

TABLE 1. *Unit-cell dimensions of compositions in the system* Fe_3O_4-Mn_3O_4 *at various temperatures*

	Cell dimensions, angstrom units								
Mn_3O_4, percent	60	65	70	75	80	85	90	95	100
Cubic / Tetragonal	*a* / a c	*a* / a c	*a* / a c	*a* / a c	*a* / a c	*a* / a c	*a* / a c	*a* / a c	*a* / a c
Temperature, °C									
25	*8.58* /	8.41 8.92	8.39 9.10	8.33 9.24	8.28 9.27	8.26 9.33	8.21 9.36	8.21 9.44	8.20 9.44
400	*8.56* /	*8.52* / 8.48 9.07	8.38 9.06	8.32 9.06	8.32 9.28	8.30 9.36	8.21 9.34		
500			*8.55*						
600	*8.56* /	*8.57*	*8.61*	*8.55* / 8.21 9.36		8.26 9.23			
700				*8.55* /	*8.60* / 8.29 9.29	8.26 9.26			
800		*8.60*	*8.60*	*8.58*	*8.60*	*8.65* / 8.35 9.35	8.26 9.36		
900			*8.61*	*8.61*	*8.60*	*8.65* / 8.37 9.38	8.29 9.31		
1,000							*8.62* / 8.33 9.50	8.27 9.44	
1,100	/		*8.60*	*8.62*	*8.60*	*8.64*	*8.60*	8.31 9.36	
1,120								*8.62*	
1,170									8.20 9.27
1,200									*8.64*

are heated, each passes from the tetragonal phase through a region in which both the tetragonal and cubic phases are in equilibrium. At high temperatures the cubic phase alone is present. The pure Mn_3O_4, of course, passes directly from the tetragonal to the cubic form with no two-phase region. As any one sample is heated to a temperature near the inversion point, the axial ratio does not approach unity as one might expect. The only change in unit-cell dimensions is a slight over-all increase due to thermal expansion. For this reason, the cubic and tetragonal patterns do not become indistinguishable at the inversion point.

Although the 60-percent Mn_3O_4 sample gave a cubic pattern at room temperature, this pattern was characterized by poorly defined peaks and considerable line broadening. The fact that the pattern improved when the temperature of the sample was raised to 600° C indicates that the cubic phase is probably not stable at room temperature. The cubic pattern obtained can be attributed to the fact that the samples were held at 1,200° C during preparation, at which temperature all would exist in the cubic phase. The 60-percent-Mn_3O_4 sample appears to have been quenched when cooled to room temperature, and it was impossible to observe any transition on reheating. Extrapolation from data obtained for samples of higher Mn_3O_4 content indicates that, in the case of the 60-percent-Mn_3O_4 sample, the cubic and tetragonal phases should be in equilibrium at about 400° C. The specimen was held at this temperature for a period of 24 hours, but there was no significant change in the pattern obtained at the end of this time. The furnace temperature was then manually lowered in small steps over a period of 2 days. When the temperature of the specimen was lowered to 250° C the lines characteristic of the tetragonal phase were discernible. The specimen was eventually cooled to room temperature, but the tetragonal pattern was still not distinct, and the cubic pattern showed some line broadening, indicating that the lattice was under strain. Thus, while it seems reasonable to assume that the cubic form containing 60 percent of Mn_3O_4 is not at equilibrium at room temperature, the tendency to supercool makes it impossible to obtain a specimen that is tetragonal. Data on samples containing 50 and 55 percent of Mn_3O_4 would be desirable, but because of the slower rate of inversion of compositions in this range, it does not seem likely that one could be reasonably sure that the patterns obtained represented the conditions at the temperature used during the test.

In figure 2 the results obtained from the patterns made at elevated temperatures are plotted. Points have been plotted for each of the samples to show the highest temperature at which the tetragonal phase alone was discernible, the lowest and highest temperature at which both the cubic and tetragonal phases could be detected, and the lowest temperature at which the cubic phase appeared alone. It should be borne in mind that a second phase may not be detected if it constitutes less than 10 percent of the specimen. Figure 2 shows the temperature range over which two phases could be distinguished, but it must be assumed that traces of the second phase too small to detect may be present outside this temperature range. As explained above, no satisfactory data

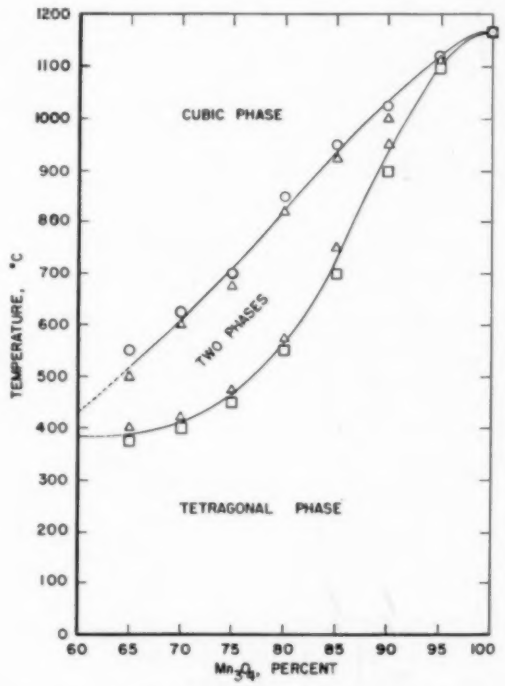

FIGURE 2. *Partial diagram of the system* Fe_3O_4–Mn_3O_4.

□, Highest temperature at which the tetragonal-phase alone was discernible; △, limits of the temperature range over which both the cubic and tetragonal phases could be detected; ○, lowest temperature at which the cubic phase appeared alone.

were obtained for the 60-percent sample. The dotted portion of the curve indicates the probable limits of the two-phase region at this end of the curve. As shown in the figure, the pure Mn_3O_4 inverts at 1,170° C and has no two-phase region.

The cell dimensions at room temperature are shown in figure 3, and the dimensions for both phases occurring at 600° C appear in figure 4.

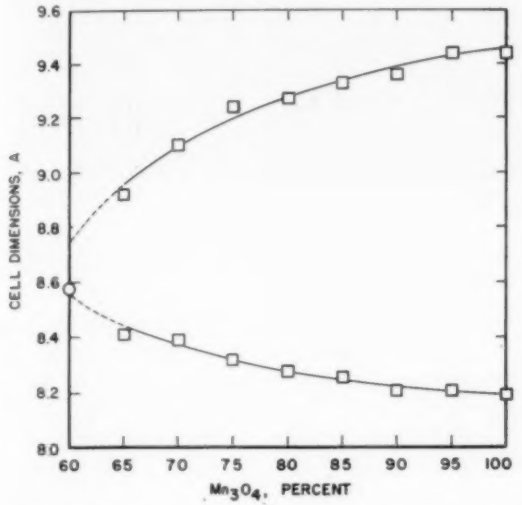

FIGURE 3. *Unit-cell dimensions at room temperature of compositions in the system* Fe_3O_4–Mn_3O_4.

□, Tetragonal phase. ○, cubic phase.

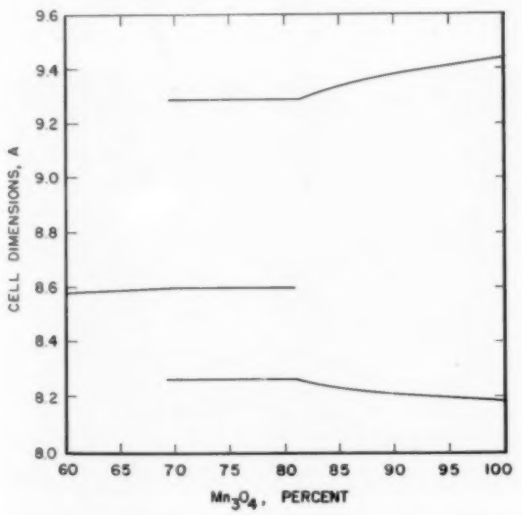

FIGURE 4. *Unit-cell dimensions of the system* Fe_3O_4–Mn_3O_4 *at 600° C.*

V. Discussion

Whereas the end compounds of the series Fe_3O_4–Mn_3O_4 are of the cubic and tetragonal structure, respectively, at room temperature, the unit cells of the two compounds have been shown to be very similar. As iron and manganese have similar atomic radii, it is not surprising to find that the two oxides are completely miscible at room temperature and form a series of substitutional solid solutions. If the unit-cell dimensions at room temperature are plotted for the series of compositions between Fe_3O_4 and Mn_3O_4 [4], it is found that the size of the cubic cell increases regularly until a composition of about 60 percent of Mn_3O_4 is reached, at which point the cubic lattice is no longer stable. When the composition exceeds 60 percent of Mn_3O_4, the cubic lattice becomes deformed and a tetragonal lattice results. The axial ratio increases continuously from unity at about 60 percent of Mn_3O_4 to 1.15 at 100 percent of Mn_3O_4. The volume of the unit cell increases almost linearly with the substitution of manganese throughout the whole range of compositions. This behavior is typical of substitutional solid solutions.

Although Fe_3O_4 and Mn_3O_4 appear to be completely miscible in the solid state at room temperature, a two-phase region has been found at higher temperatures. For example, at 600° C manganese may be substituted for iron to obtain a single cubic phase until a composition of about 69 percent of Mn_3O_4 (by weight) is reached. Likewise, iron may replace manganese in the tetragonal structure of Mn_3O_4, giving a single tetragonal phase. When a composition of 81 percent of Mn_3O_4 and 19 percent of Fe_3O_4 is reached, however, no more iron will go into the structure of Mn_3O_4. For this reason, there is a range of compositions at this particular temperature within which each sample is a mixture of two phases.

The vredenburgite occurring in nature usually shows two phases, cubic and tetragonal. Mason believed that this two-phase mineral, rather than the prepared samples, represented equilibrium conditions at room temperature, and that the compositions of the two phases making up the mineral therefore represented the limiting values of the solubility of Mn_3O_4 in Fe_3O_4 and of Fe_3O_4 in Mn_3O_4 at normal temperatures and pressures. In

886334—50——4

his survey of the minerals comprising the system Fe_3O_4-Mn_3O_4, he designated as vredenburgite those substances whose compositions lie within the area of immiscibility, that is, between 54 and 91 percent of Mn_3O_4. He arrived at these limits by examining samples of vredenburgite and comparing the lattice dimensions of each of the two phases present with those of a series of preparations that covered all compositions from Fe_3O_4 to Mn_3O_4 at intervals of 10 mole percent.

The present investigation shows that there is no region of immiscibility at room temperature and that Mason's criterion for establishing the limits of composition for vredenburgite is not based on equilibrium conditions at room temperature.

Mason also found specimens in the range from 54 to 91 percent of Mn_3O_4, which consisted of a single tetragonal phase. Believing that the single-phase type was a high-temperature form not in equilibrium at room temperature, he proposed calling it α-vredenburgite and reserved the name β-vredenburgite for the two-phase material. In choosing these designations, Mason followed the convention that the high-temperature form should be indicated by the prefix α. However, the present study indicates that the two-phase form (β-vredenburgite) is the one that is stable at higher temperatures. To prevent confusion, it is suggested that Mason's designations be retained, the two-phase material being called β-vredenburgite.

Figure 5 is a photomicrograph of β-vredenburgite from India. The cubic phase appears as a black background, upon which the bright lines due to the tetragonal phase may be seen. As this material is unstable at room temperature, we must assume that, in cooling, the specimen remained in the two-phase region long enough for fairly large crystals of the tetragonal phase to form by exsolution. Subsequent cooling must have been rapid enough so that reaction between the two phases could not proceed and a degree of quenching took place.

Figure 6 is a photomicrograph of natural hausmannite from Sweden that shows polysynthetic twinning, as has been noted previously, [5] typical of material that has undergone a simple inversion [12]. In this case, the material must have had the cubic spinel structure before cooling through the inversion temperature.

Because of the difficulty in distinguishing iron from manganese by their difference in scattering power, no information could be obtained about the distribution of cations among the positions available in the spinel structure. Barth and Posnjak [13] have shown that even the valence of a particular atom does not determine which metal position it will assume.

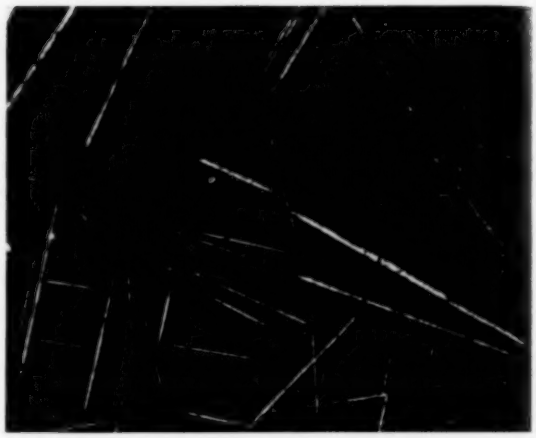

FIGURE 5. *Photomicrograph of β-vredenburgite from India by reflected polarized light.*

The tetragonal phase appears as bright lines and the cubic phase as the dark background. ×180.

VI. Summary

At room temperature, Fe_3O_4 and Mn_3O_4 appear to be completely miscible in the solid state. Manganese may be substituted for iron in the

FIGURE 6. *Photomicrograph by reflected polarized light showing polysynthetic twinning of hausmannite from Sweden. ×180.*

cubic spinel-type structure of Fe_3O_4 until a composition of about 60 percent by weight of Mn_3O_4 is reached. Compositions containing more manganese take on the tetragonal structure of pure Mn_3O_4, and the axial ratio increases continuously from unity at 60 percent of Mn_3O_4 to 1.15 at 100 percent.

The volume of the unit cell increases regularly with the addition of manganese.

In the temperature range from 380° to 1,170° C, compositions above 60 percent of Mn_3O_4 are not completely miscible. When a composition with the tetragonal structure is heated, a temperature is reached at which a cubic phase of the spinel type starts to form. This cubic phase is in equilibrium with the tetragonal phase over a range of temperatures that depends on the composition. The percentage of tetragonal material decreases with further heating until a temperature is reached at which all the material has the cubic spinel-type structure. From this temperature up to the melting point, only the cubic phase is present.

The natural two-phase mineral β-vredenburgite is not at equilibrium at room temperature. The one-phase mineral α-vredenburgite is the low-temperature form.

VII. References

[1] H. F. McMurdie and E. Golovato, Study of the modifications of manganese dioxide, J. Research NBS **41,** 589 (1948) RP1941.

[2] G. Aminoff, The Crystal structure of hausmannite, Z. Krist. **64,** 475 (1926).

[3] R. W. G. Wyckoff, The structure of crystals, 2d ed., p. 297 (Reinhold Publishing Corp., 1931).

[4] B. Mason, Mineralogical aspects of the system FeO-Fe_2O_3-MnO-Mn_2O_3, Geol. Fören. Förh. **65,** 97 (1943).

[5] J. Orcel and S. Pavlovitch, Les caractéres microscos piques des oxydes de manganese et des manganite-naturels, Bul. soc. franc. minéral. **54,** 108 (1931).

[6] H. Schneiderhohn and P. Ramdohr, Lehrbuch der erzmikroskopie, **2,** 602, Berlin (1931).

[7] B. Mason, α-Vredenburgite, Geol. Fören, Förh. **65,** 263 (1943).

[8] H. Von Eckermann, Some remarks on the system Fe_3O_4-Mn_3O_4, Geol. Fören. Förh. **65,** 258 (1943).

[9] V. Montoro, Miscibilita fra gli ossidi salini di ferro e di manganese, Gass chim. ital. **68,** 728 (1938).

[10] B. Mason, Mineralogical aspects of the system, Fe_3O_4-Mn_3O_4-$ZnMn_2O_4$-$ZnFe_2O_4$, Am. Mineral. **32,** 426 (1947).

[11] A. Van Valkenburg, Jr., and H. F. McMurdie, High temperature X-ray diffraction apparatus, J. Research NBS **38,** 415 (1947), RP1782.

[12] H. Le Chatelier, The constitution of hydraulic mortars p. 53 (McGraw-Hill Book Co., Inc., New York, N. Y., 1905).

[13] T. F. W. Barth and E. Posnjak, Spinel structures, Z. Krist. **82,** 325 (1932).

WASHINGTON, March 29, 1950.

U. S. Department of Commerce
National Bureau of Standards

Research Paper RP2112
Volume 45, July 1950

Part of the Journal of Research of the National Bureau of Standards

A Quantitative Study of the Carbon Monoxide Formed During the Absorption of Oxygen by Alkaline Pyrogallol

By Marthada V. Kilday

The amounts of carbon monoxide evolved during analytical absorptions of oxygen by alkaline pyrogallol were studied with respect to the composition and methods of preparing solutions, the temperature of reaction, the rate of flow of the sample through the solution, the capacity of the reagent for the absorption of oxygen, the partial pressure of reacting oxygen, and the manner of bringing the gas into contact with the reagent. Less than 0.02 percent of carbon monoxide was formed during analyses of gases containing as much as 80 percent of oxygen when the recommended solutions were used in bubbler-type absorption pipettes, and when the samples were passed into the solutions at a rate greater than 20 milliliters per minute at about 25° C. This was true until the solutions had absorbed approximately twelve times their volume of oxygen, after which the formation of carbon monoxide increased significantly. The NBS colorimetric carbon monoxide indicating gel was used for the quantitative determinations of carbon monoxide. A method was developed for preparing pyrogallol solutions that yielded reproducible amounts of carbon monoxide so small that no significant error was caused in the usual analysis.

I. Introduction

For many years it has been known that under some conditions the analytical absorption of oxygen by alkaline pyrogallol is subject to an error introduced by the formation of carbon monoxide during the reaction. This carbon monoxide is measured as part of the residue after absorption, so that the oxygen absorbed appears to be less than was actually present in the original sample. If a combustion analysis follows, the carbon monoxide may contribute further error.

Pyrogallol is so superior to other reagents sometimes employed for the removal of oxygen, with respect to the exchange of gases inert to it, that errors of physical solubility are very greatly reduced by its use [1].[1] However, the evolution of carbon monoxide has long been invoked as an argument against the use of pyrogallol. It will be shown in this paper that this argument is unfounded, as no significant amount of carbon monoxide is formed under the conditions of the usual analysis when the recommended solutions are used.

Many investigators have tried to determine the amount of carbon monoxide formed under the conditions of the conventional analytical procedures, but usually they have found that the concentration of carbon monoxide was too low for the methods of analysis employed. Therefore they have resorted to measuring the relatively large amounts of carbon monoxide produced under extreme conditions, such as high partial pressures of oxygen, weakly alkaline pyrogallol solutions, and high temperatures of reaction. Even with these high concentrations of carbon monoxide, which came within the range of their analytical methods, there was a great divergence in the results obtained by various investigators.

During World War II, this Bureau developed a colorimetric indicator for the quantitative determination of carbon monoxide in low concentrations

[1] Figures in brackets indicate the literature references at the end of this paper.

up to 0.1 percent. Higher concentrations were determined by making simple dilutions of the samples [2].

The NBS indicator was found to be very satisfactory in the direct analyis of the carbon monoxide present in the residues of oxygen absorptions by pyrogallol. During the preliminary work, it was found that, although a given solution yielded reproducible amounts of carbon monoxide during a series of like analyses, there was significant variation in the amount of carbon monoxide generated by different solutions prepared according to the same formula. This led to an investigation of the methods of preparing the pyrogallol solutions. By dissipating the heat produced while dissolving the pyrogallol in a saturated solution of potassium hydroxide, solutions were prepared that not only gave reproducible results with respect to carbon monoxide generated, but which consistently evolved less carbon monoxide during an absorption.

A satisfactory method of preparing the pyrogallol solutions having been established, it was possible to proceed with the determination of carbon monoxide evolved under various conditions. The data obtained in this experimental study are reported so that the gas analyst may use them in estimating the error to be expected as a result of carbon monoxide formation under the conditions of the analysis.

II. Description of Apparatus

A modification of the Shepherd gas analysis apparatus [3] with spherical, interchangeable ground-glass joints instead of rubber connections was used in this study, and Apiezon grease "L" was the stopcock lubricant employed. Figure 1 is a diagram of the distributor as modified for this work. Below stopcock 1 is the absorption pipette. Two mercury reservoirs, connected under stopcocks 2 and 3, were used for diluting and mixing the residues from the absorptions of oxygen, which were too rich in carbon monoxide to be analyzed directly with the NBS colorimetric indicator. Below stopcock 4 is a tube containing gold sponge to remove mercury vapor, which interferes with the test for carbon monoxide. The colorimetric carbon monoxide indicator tube was attached with a pure gum rubber connection below the gold sponge. Between stopcocks 5 and 6 was a calibrated flowmeter that was provided to measure the rate of flow of the residue after absorption through the carbon monoxide indicator tube. The position of the stopcocks could be manipulated so that the flowmeter containing mercury was either included or excluded from the distributor train. The burette and compensator were previously described [4].

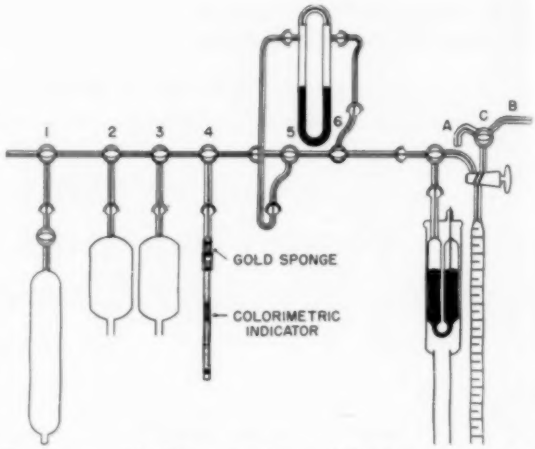

FIGURE 1. *Distributor showing modifications provided for the carbon monoxide determination and for measuring the rate of flow of the gas.*

The volumetric analyses were made in a laboratory where the temperature was maintained at about 25° C. The room was reserved primarily for making physical measurements and was therefore free of the atmosphereic contaminations and variations present in many chemical laboratories.

The nine types of absorption pipettes used in this investigation are shown in figure 2.

III. Method for Determination of Carbon Monoxide

The NBS colorimetric indicator for carbon monoxide and the "Laboratory Method" described by Shepherd [2] were used in the analyses for carbon monoxide reported in this paper. A detailed description of the analytical procedure as adapted to this problem is given in section V.

The chemicals of the indicator tube are inclosed in a 15-cm length of 7-mm Pyrex glass tubing. The 2-cm length of yellow indicating gel, which turns green upon exposure to carbon monoxide, is protected at both ends by a 5-cm length of purified silica gel, which removes water vapor and

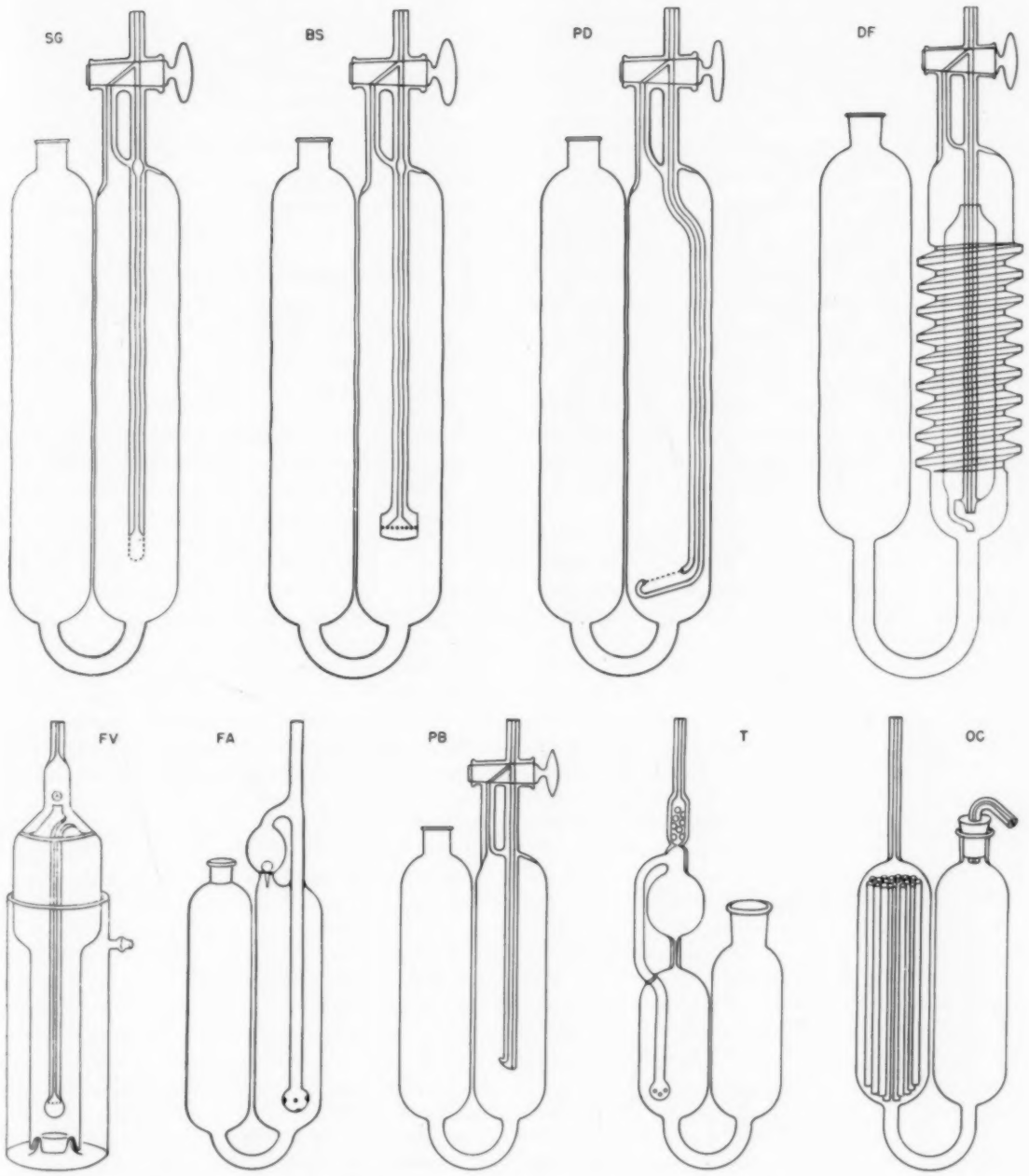

FIGURE 2. *Absorption pipettes: Sintered-glass bubbler (SG); Branham-Sperling bubbler (BS); platinum-disk bubbler (PD); Dennis-Friedrichs (DF); Fisher valve-bubbler (FV); Francis autobubbler (FA); Hankus or plain bubbler (PB); Tramm double-action (T); Orsat contact (OC).*

organic vapors that might interfere with the determination of carbon monoxide. The guard gel is held in place by absorbent cotton, and a cork is placed in each end when the tube is not actually being used.

To determine the percentage of carbon monoxide present in an unknown sample, a measured volume of the sample is passed through the indicator tube at a controlled rate of flow. The color developed by the indicating gel is compared with standards prepared by exposing tubes to known concentrations of carbon monoxide. The percentage of carbon monoxide expressed in this paper is based on the volume of the original sample and refers to the amount of carbon monoxide that would have been generated by 100 ml of original sample. In other words, if it is stated that a solution generated 0.02 percent of carbon monoxide, it means that 0.02 ml of carbon monoxide would have been present in the residue of absorption of 100 ml of original sample.

In this work there was a linear relationship between the concentration of carbon monoxide and the probable error of the carbon monoxide determination. From 0.0020 to 0.039 percent of carbon monoxide, the error was about 17 percent of the carbon monoxide present. These errors could have been reduced to less than half of these values (1) by reducing the interval of time in exposing standards to the known mixtures of carbon monoxide and (2) by having the concentration of carbon monoxide in the known mixtures nearly the same as the partial pressure of carbon monoxide that exists in the unknown. These refinements were not employed in this work because most volumetric gas analysis apparatus are not capable of such accuracy. If the analyst is concerned with extreme accuracy, a determination of carbon monoxide should be made for each individual analysis, as there is some variation in the amount of carbon monoxide produced even when the conditions of the analyses are similar.

IV. General Methods for Preparing Solutions

Prior to the present study, the gas chemistry laboratory had used a method of preparing pyrogallol solutions that was previously described [3] and is quoted below (page 145 of this reference):

> The reagent used for the removal of oxygen in the absorption pipette . . . (platinum-disk bubbler) is an alkaline pyrogallol solution. This is made by dissolving crystalline pyrogallol in a minimum amount of hot water and adding this solution to the concentrated potassium hydroxide solution . . . The resulting solution closely approximates one recommended by Anderson,[4] who found a solution containing 15 g of pyrogallol per 100 ml of potassium hydroxide solution of 1.55 specific gravity to be satisfactory. . . .
>
> In order to prevent air from reaching the reagents a layer of light mineral oil, about 10 to 15 mm in depth, is poured over the reagent in the reservoir arm of the pipette. This also permits the preparation of the pyrogallol solution within the pipette itself and out of contact with air. The potassium hydroxide solution is first introduced, the oil is placed over this solution and the pyrogallic acid solution in water is introduced beneath the layer of oil from a pipette.

[4] Anderson, R. P., Ind. Eng. Chem. 7, p. 588 (1915).

It was necessary to heat the pyrogallol crystals with water in order to prepare the solution within a reasonable length of time, and this solution, while still hot, was poured through a long-stemmed funnel to the bottom of the saturated potassium hydroxide solution in the pipette. This was frequently accompanied by considerable bubbling and splattering as a result of the additional heat produced during solution.

Preliminary work of this study indicated that this method of preparation produced solutions yielding inconsistent results with respect to the concentration of carbon monoxide evolved. Consequently, an improved method was developed that produced solutions that yielded reproducible amounts of carbon monoxide when used under similar conditions. This solution, quite happily, yielded significantly less carbon monoxide than previous solutions. A description of the improved method follows.

The saturated potassium hydroxide solution is prepared by saturating distilled water with solid potassium hydroxide at 25° ±1° C. This solution contains about 55 percent of potassium hydroxide, or 120 g of potassium hydroxide per 100 g of water, and has a specific gravity of about 1.55.

The flask or pipette in which the pyrogallol is to be stored is placed in an ice bath, and the pyrogallol crystals are placed in the bottom of the container. The saturated solution of potassium hydroxide is added rapidly, and the flask is sealed with an air-tight cover, or a layer of light mineral oil is added if the solution is prepared in a pipette. The new solution should remain in the bath until

the ice melts and the bath reaches room temperature, at which time it may be used immediately or stored for future use. If any crystals remain undissolved, agitating the solution in the pipette by passing nitrogen into it will complete solution. Data will be presented that show no significant difference in the amount of carbon monoxide formed by solutions that were freshly prepared and those that were stored out of direct sunlight for as long as 21 months.

V. Procedure for Analyses

In the course of this study, five partial pressures of oxygen were used: approximately 21 (air), 40, 60, 80 percent of oxygen in nitrogen, and 100 percent of oxygen. Air was sampled directly from the laboratory in which the analyses were made, and the other mixtures and the approximately pure oxygen were stored under pressure in gas cylinders from which samples were taken in the following manner. A needle valve was used to control the sampling rate, and the sample was passed through copper tubing to *A*, figure 1, and connected by means of nitrometer pressure tubing. The sample was thoroughly flushed from *A* through *B*, and stopcock *C* was turned to admit the sample under pressure to the mercury-filled burette.

The sample was saturated with water vapor from the burette walls, and the volume was measured in the usual way. Unless otherwise stated, the rate of flow of the gas to the absorption pipette was controlled only by the maximum rate at which the mercury could flow into the burette and by the back pressure exerted in the pipette; this was usually about 190 to 250 ml/min. After enough passes had been made into the pyrogallol to assure complete absorption of the oxygen, the residue was returned to the burette, saturated, and measured as before.

From this point the procedure depended upon the total volume of the residue as well as the concentration of carbon monoxide. Dilution was necessary if the amount of carbon monoxide exceeded 0.04 percent, or if the residual volume was less than 70 ml, which was the minimum set for each determination in this work. If no dilution was needed, the determination of carbon monoxide was made immediately.

When the volume of the residue was too small, it was measured at atmospheric pressure and air was drawn into the burette. The volume of the resulting mixture was also measured at atmospheric pressure, and the concentration of carbon monoxide present in the residue was computed.

If the concentration of carbon monoxide in the residue after absorption was expected to exceed the range of the colorimetric carbon monoxide indicator, a fraction of the residue was stored in one of the mercury reservoirs, and the remaining portion was diluted and treated as in the procedure described above. If further dilution was necessary, the second mercury reservoir was used to store the residue from the first dilution, and a measured volume of air was taken into the burette and mixed with the first diluted residue.

The amount of carbon monoxide in the residue or in the diluted residue was determined as follows. Six indicator tubes were used in the analysis, one for the residue and five for color standards. An indicator tube was attached to the volumetric gas analysis apparatus as shown in figure 1. The distributor was flushed, and 45 ml of the residue was passed through the indicator tube at 90 ml/min, which is equal to a 30-sec exposure. The standards were prepared by passing a known concentration of carbon monoxide through indicator tubes at 90 ml/min for varying periods of time—usually at 5-sec intervals. The five standard mixtures of carbon monoxide in air were: 0.0025_7, 0.0052, 0.0097, 0.020_2, and 0.038_2 percent. The percentage of carbon monoxide in the unknown (residue) was determined by comparing visually the color developed in this tube with the colors of the tubes that had been exposed to known concentrations of carbon monoxide.

VI. Data and Discussion

1. Effect of Variations in Pyrogallol Solutions

(a) Experimental Methods of Preparation

An inspection of the graphs in figure 3 reveals the inconsistencies found in the amount of carbon monoxide formed by solutions prepared by the "old" method previously described. These graphs show the amount of carbon monoxide evolved during absorptions of oxygen from air by solutions of various compositions individually prepared in several platinum-disk bubbler pipettes (see table 1). It may be seen that the amounts of carbon monoxide evolved during absorptions of oxygen from air under similar conditions by any one solution (those in any one small block) were

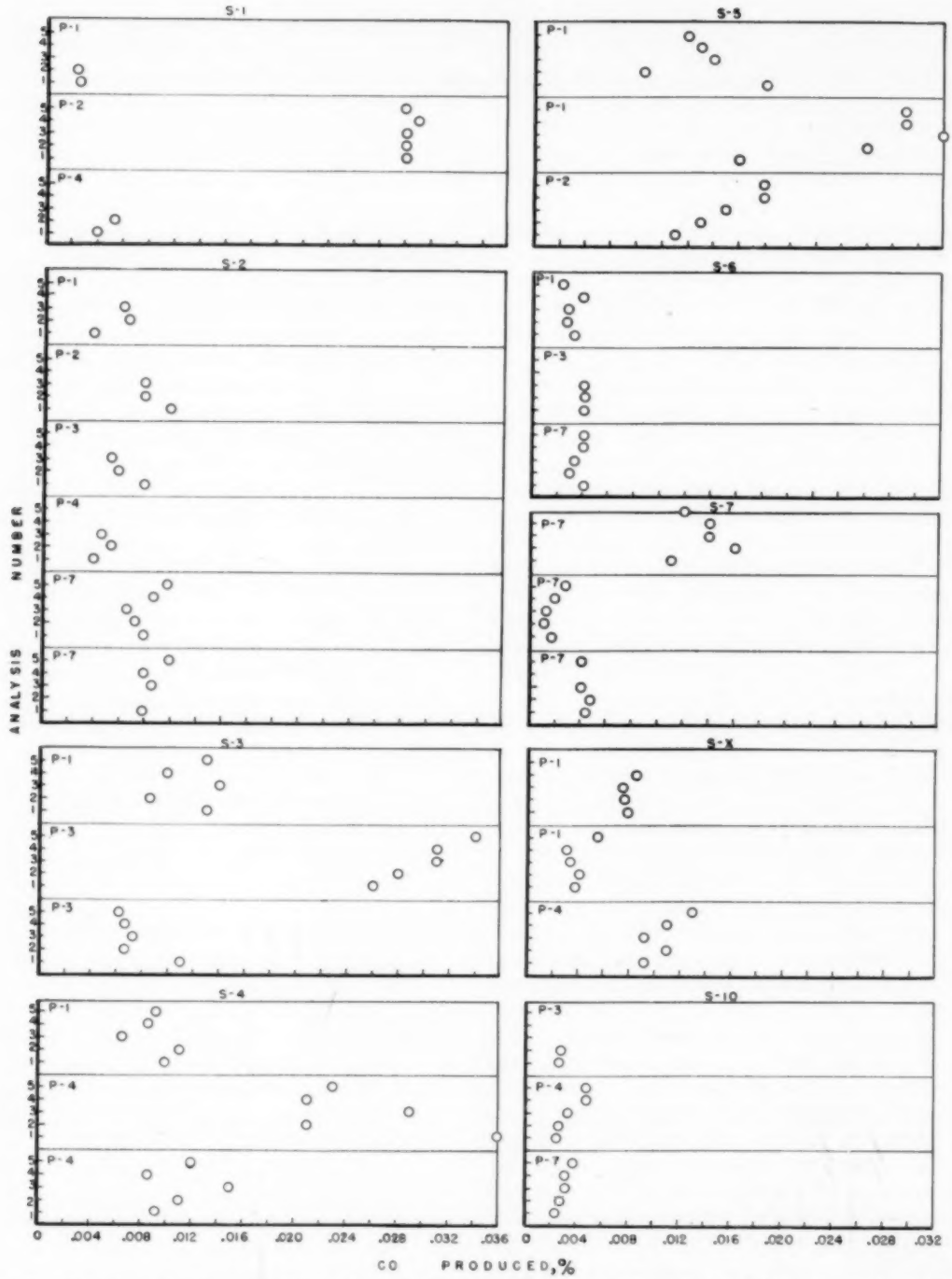

FIGURE 3. *Percentage of carbon monoxide produced during absorption of oxygen from air by solutions prepared according to the old method.*

Composition of the solutions are found in table 1. The number in the upper left-hand corner of each small block indicates which platinum-disk bubbler pipette was used.

reasonably consistent, but in various solutions of the same composition (those in any one large block) the amount of carbon monoxide produced sometimes varied by as much as a factor of 10.

TABLE 1. *Composition of solutions studied*

Composition No.	Pyrogallol [a] [b]	Solution		Pyrogallol per 100 ml of saturated KOH solution [a] [c]
		Potassium hydroxide saturated at 25° C	H_2O	
	g	*ml*	*ml*	*g*
S–1	35	225	0	------
S–2	35	200	25	------
S–3	35	175	50	------
S–4	35	150	75	------
S–5	35	125	100	------
S–6	------	------	------	25
S–7	------	------	------	20
S–X [d]	------	------	------	17
S–Z [d]	------	------	------	14
S–10	------	------	------	5
S–B7	(e)	(e)	(e)	(e)
S–BZ	(f)	(f)	(f)	(f)

[a] The crystalline pyrogallol was obtained commercially under the name "Acid pyrogallic, analytical reagent." When the old method of preparing solutions was used, an additional 10 ml of water was added to dissolve the crystalline pryogallol.

[b] The amount of pyrogallol was equal to about 15.5 g of pyrogallol per 100 ml of diluted solution of saturated potassium hydroxide. Thus the solutions of these compositions would logically be placed between solutions S–X and S–Z, except for the dilutions of the saturated potassium hydroxide solution.

[c] The concentration of potassium hydroxide was the same as that used in solution S–1, which was found to produce the least carbon monoxide in the series showing the effect of changing the concentration of potassium hydroxide in the solution.

[d] The only significance attached to S–X and S–Z is that the former was of a composition in general use by this laboratory before this work, and the latter was found to be the most desirable composition when the improved method of preparing solutions was used.

[e] 1 liter of solution S–7 stored in an Erlenmeyer flask and the cap sealed with paraffin.

[f] 2 liters of solution S–Z stored in an Erlenmeyer flask and the cap sealed with Apiezon grease "L".

The fact that the variations were not caused by the use of different platinum-disk bubbler pipettes is shown in solutions S–3, S–4, S–5, and S–7 where inconsistencies were found when the same pipette was used for different preparations of solutions of the same composition.

A thorough investigation was made of the possible causes for the variations shown in figure 3. First, the accuracy of the determination of carbon monoxide was verified by taking into the burette samples of a known concentration of carbon monoxide and determining the carbon monoxide present by the same method used in the analysis of the residues of absorption. In the ten analyses made, the maximum deviation from the known value was 10 percent of the carbon monoxide present, with an average deviation of 6 percent. The accuracy of the determination of carbon monoxide was therefore discounted as a significant variable. Other possible variables, which will be discussed in detail later, were:

1. Concentration of the solution with respect to pyrogallol.
2. Concentration of the solution with respect to potassium hydroxide.
3. Rate of flow of sample into pyrogallol solution.
4. Age of solution (actual age and also the degree expended).
5. Temperature of reaction during absorption of oxygen.
6. Number of passes into pyrogallol solution.

These factors were controlled sufficiently to eliminate them as significant variables in the runs represented in figure 3. This left the actual method of preparing the pyrogallol solutions as the most probable cause of the extreme deviations.

It was believed that variations in the temperature of solutions might have caused differences in the solutions themselves, which in turn caused differences in the amount of carbon monoxide evolved during the absorption of oxygen in different runs. As the measurement of the maximum temperature developed at several points would have been rather difficult in this instance, the effect was shown by preparing solutions in which it was known that the temperature of the solution had been varied by large amounts.

Figure 4 shows the amount of carbon monoxide formed in absorptions from gaseous mixtures containing 21 percent and 80 percent of oxygen by solutions that were prepared in five different ways, each varying with respect to the temperature allowed to develop during preparation.

The greatest amount of carbon monoxide per unit volume of oxygen was evolved by the solution prepared by method 2 (see fig. 4) in which the pyrogallol was added all at once to the saturated potassium hydroxide solution at 53° C in an atmosphere of nitrogen. The yield of carbon monoxide was 0.023 to 0.059 percent during absorptions of oxygen from air.

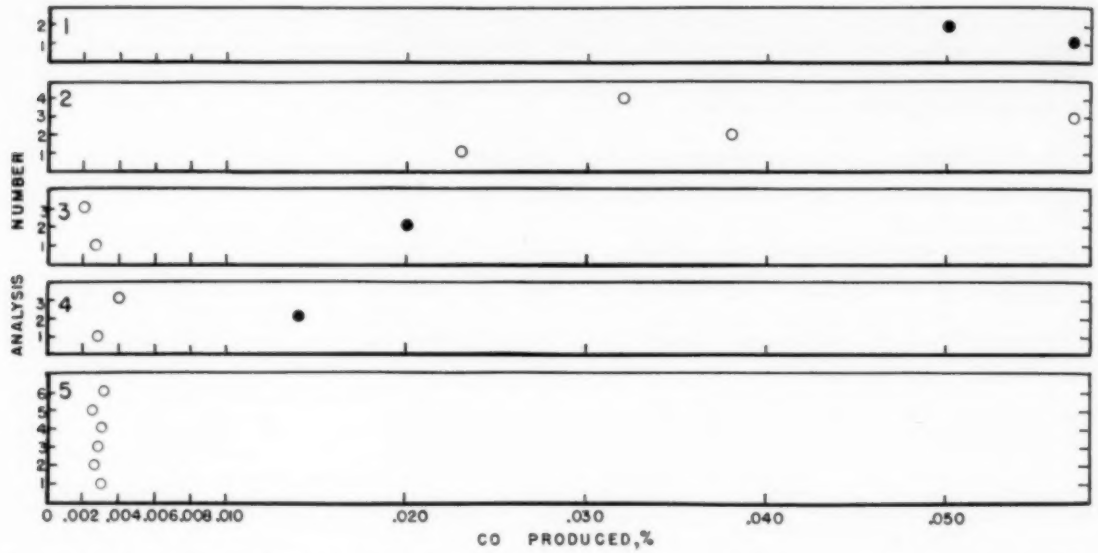

FIGURE 4. *Percentage of carbon monoxide produced during absorption of oxygen by solutions prepared according to various methods.*

The analysis number on the left shows the order in which the analyses were performed. The composition number of the solutions and the pipettes used are indicated as follows: 1, S–6, PD–3, method 1; 2, S–X, SG, method 2; 3, S–X, SG, method 3; 4, S–X, PD–4, method 4; 5, S–X, PD–7, method 5. ○, 21% O_2 (air); ●, 80% O_2 in N_2.

In method 1 the pyrogallol was dissolved, by heating it with a little water (to approximately 110° C), and added in small increments to the saturated potassium hydroxide solution at room temperature, with vigorous stirring after each addition. In this case, the dissipation of heat was more rapid, and the carbon monoxide evolved during the absorption from a mixture containing 80 percent of oxygen was about 0.05 to 0.06 percent, which is of the same order as that produced by the previously described solution when only 21 percent of oxygen was absorbed. Since the higher partial pressure of oxygen will produce more carbon monoxide in the same solution, it was assumed that the carbon monoxide evolved by the solutions during absorptions was probably dependent to some extent upon the rapidity of the dissipation of heat during the preparation of the pyrogallol solutions.

In preparing the solution according to method 3, it was found unnecessary to dissolve the pyrogallol crystals in water, as previously described, before adding them to the saturated potassium hydroxide solution. The solution was made by simply adding the crystalline pyrogallol to the saturated solution of potassium hydroxide at room temperature and placing the mixture in a refrigerator overnight to accelerate the dissipation of the heat of reaction. Here the carbon monoxide evolved was reduced by more than half of that found in method 1 in the absorption from a mixture containing 80 percent of oxygen, and the reduction in carbon monoxide formed in the absorption of oxygen from air was remarkable, as little as 0.002 to 0.003 percent being generated.

In method 4 the pyrogallol crystals were added, while stirring, to the saturated potassium hydroxide solution in an ice bath at 8° C. The solution remained in the bath until it reached room temperature. With 21 percent of oxygen, this solution yielded about the same amount of carbon monoxide as in method 3; with 80 percent of oxygen, the yield was appreciably less.

Method 5 was found to be the most convenient. The absorption pipette containing the pyrogallol crystals was nearly immersed in an ice bath, and the saturated solution of potassium hydroxide, at room temperature, was added. This solution remained in the bath until it reached room temperature. The reproducibility in the amount of carbon monoxide formed by solutions prepared according to this method was very satisfactory,

and the yield of carbon monoxide was low, about 0.002 to 0.004 percent. None of the solutions showed variations in the amount of carbon monoxide formed that were greater than those that occurred in different analysis made with a single solution. The reproducibility will be discussed in more detail later.

(b) Composition

The composition for the solutions studied in this investigation are given in table 1, and reference to the solutions of these compositions will be made only by number. The table is arranged to show the manner of preparing the solutions as well as the composition.

Although the pyrogallol solutions represented in figure 3 were prepared according to the old method, they may be used to illustrate the general effect of changing the concentrations of potassium hydroxide and pyrogallol in solutions, if the obviously erratic runs are eliminated. In solutions S–1 through S–5, the pyrogallol remained constant while the concentration of potassium hydroxide became progressively less. Solution S–1 yielded 0.002 to 0.006 percent of carbon monoxide, and as the alkalinity decreased, the carbon monoxide produced became greater until in S–5 about 0.01 to 0.02 percent of carbon monoxide was formed during air analyses.

The concentration of potassium hydroxide remained constant in solutions 6, 7, X, and 10, but the weight of pyrogallol was varied (see table 1). The changes in the concentration of pyrogallol (in the solutions used) apparently did not affect the amount of carbon monoxide produced during absorptions of the oxygen in air. This fact was also supported by the analyses in figure 5, which represents solutions prepared according to the improved method. The soultions represented by blocks 1 and 2 contained 17 g of pyrogallol per 100 ml of saturated potassium hydroxide solution and were prepared in the same pipettes as those in blocks 5 and 10, the solutions of which contained only 14 g of pyrogallol per 100 ml of saturated potassium hydroxide solution.

Increased viscosity and clotting occurred sooner in solutions having higher concentrations of pyrogallol. The clotting impaired the efficiency of the distributor pipettes by reducing the number of openings through which bubbles could escape, by trapping the fine bubbles in the viscous solution, and by reducing the rate of flow of the sample into the solution. Finally, the distributor openings became plugged and no gas at all could be bubbled into the solution. In all solutions shown in figure 5, except block 1, oxygen was absorbed by the solution until the distributor became so badly plugged that the sample could not be passed into solution at a rate greater than 40 ml/min. At least twice as much oxygen was absorbed by S-Z (blocks 5 and 10) as by S-X because of the delay in clotting, which resulted from a decrease in pyrogallol content.

It was previously stated that in solutions prepared by the old method no significant difference was found in the amount of carbon monoxide evolved during oxygen absorptions when different platinum-disk pipettes were used. However, when the solutions were prepared by the improved method, the data shown in figure 5, blocks 1, 2, 5, and 10, where pipettes SG–1 and SG–2 were used, indicate that in the initial absorptions of 80 percent of oxygen, 0.012 to 0.017 percent of carbon monoxide was formed, and in all the other pipettes the corresponding absorptions yielded only 0.004 to 0.008 percent of carbon monoxide. All of the sintered-glass bubbler pipettes were supposed to be identical, but pipettes SG–1 and SG–2 were purchased at a different time from the others and there may have been some difference in the sintered-glass bubblers.

Two or three drops of an antifoamer, 2-ethyl hexanol, were added to the solutions represented in blocks 3, 5, 7, and 9. No undesirable effects were observed as a result of its use, and it reduced the excessive foaming present when the solutions were new and of relatively low viscosity.

(c) Age

The age of a solution may refer to its age in time or to the extent to which it is expended. It may be seen in figure 6 that the aging of a solution before oxygen absorptions were begun had no significant effect upon the amount of carbon monoxide produced. The graphs on the left represent solutions, S–X, that were prepared according to the old method in a plain bubbler pipette. No significant variation in carbon monoxide formed is noted from 1 to 8 days. The erratic result at 6 days is an illustration of the vagaries to be expected when solutions are prepared from the same formula by the old method.

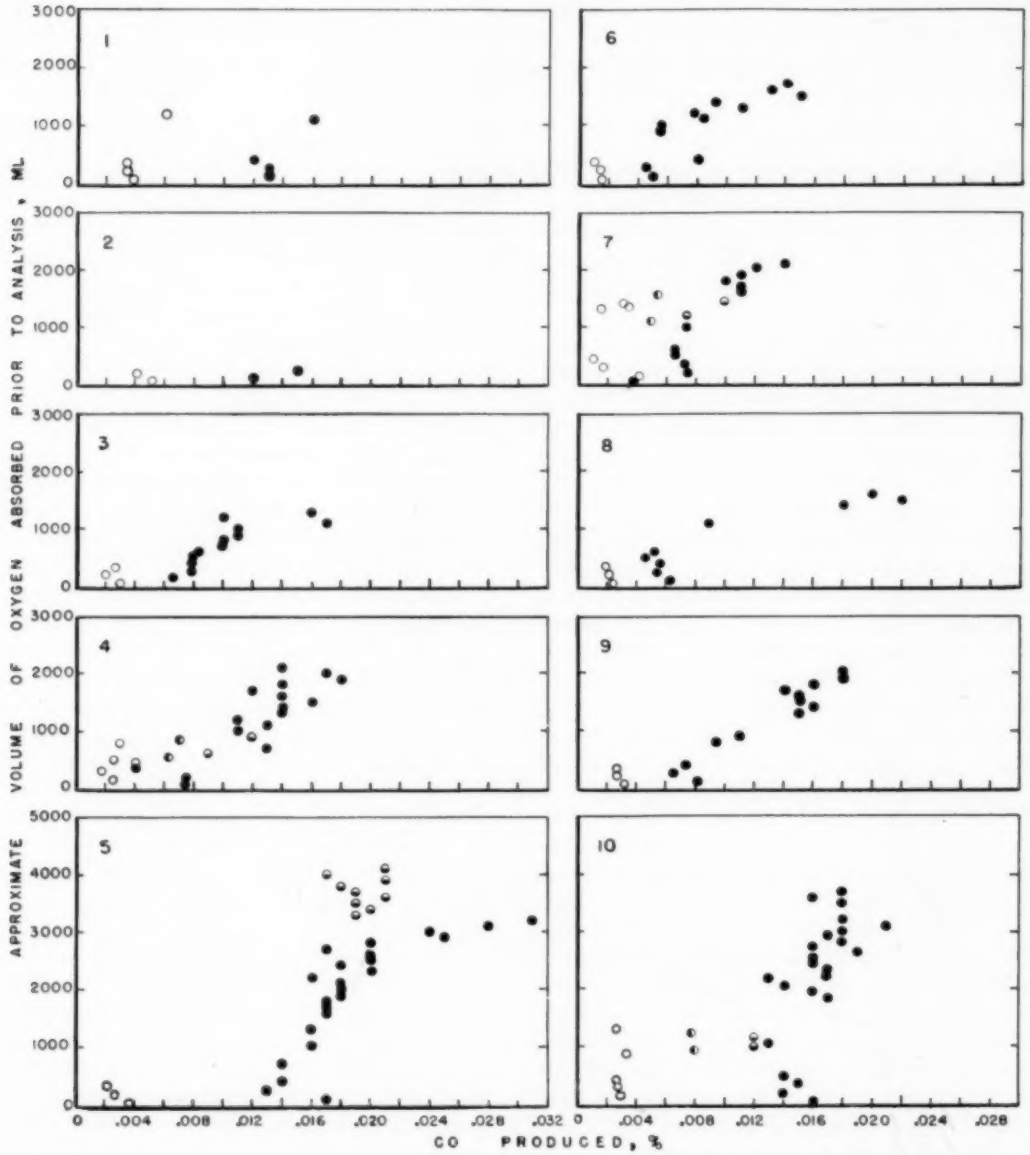

FIGURE 5. *Percentage of carbon monoxide produced during absorptions of oxygen by solutions S-X and S-Z prepared by the improved method in various sintered-glass bubbler pipettes.*

1, S-X, SG-1 (not taken to completion) 2, S-X, SG-2; 3, S-X, SG-1a (antifoamer); 4, S-X, SG-3; 5, S-Z, SG-1 (antifoamer); 6, S-X, SG-7; 7, S-X, SG-9 (antifoamer); 8, S-X, SG-10; 9, S-X, SG-12 (antifoamer); 10, S-Z, SG-2. ○, 21% O_2 (air); ◐, 40% O_2 in N_2; ◒, 60% O_2 in N_2; ●, 80% O_2 in N_2.

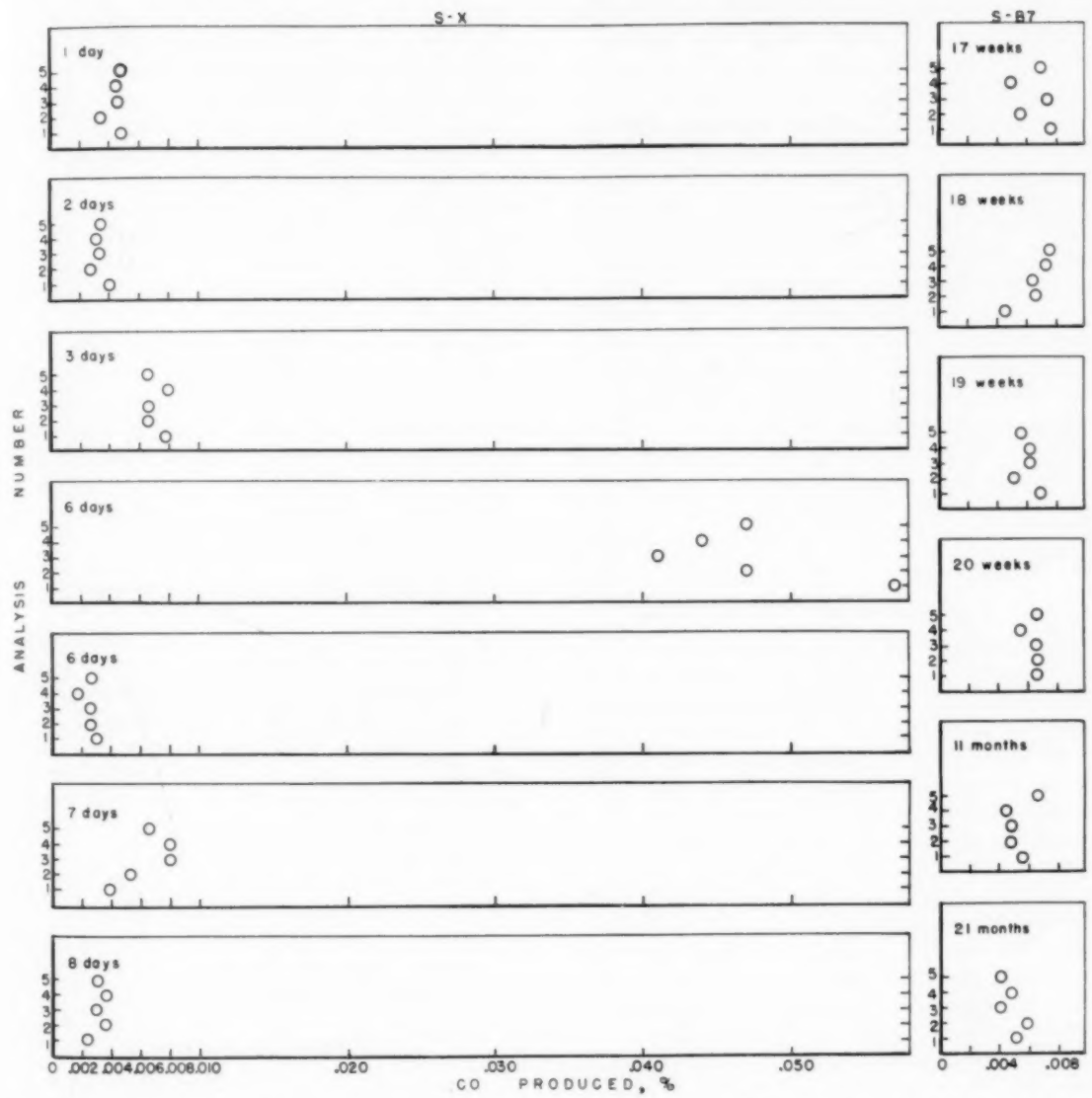

FIGURE 6. *Percentage of carbon monoxide produced during absorptions of oxygen from air by solutions S–X and S–B7, which were prepared by the old method.*

The preliminary age of the solution is shown in the upper left-hand corner of each block.

The plots on the right-hand side of figure 6 show more conclusively that age has no effect. Two liters of solution B7 was prepared in an Erlenmeyer flask by the old method. The flask, on which the glass cap was sealed with paraffin, was stored out of direct sunlight for 17 weeks. About 150 ml of the solution was then transferred to a plain bubbler pipette, and the flask was again sealed and stored. This procedure was repeated when the age of the solution was that indicated in the graphs. Air analyses were made with each portion of this solution, and it was found that no significant change had occurred in the amount of carbon monoxide produced by solutions that were stored from 17 weeks to 21 months.

The relationship between the carbon monoxide produced and the total volume of oxygen absorbed at the point of analysis is shown in figure 5. At first there is a gradual increase in the amount of carbon monoxide formed as more oxygen is absorbed, and, in most cases, there is a rather sharp increase in the amount of carbon monoxide produced after about 800 ml of oxygen absorbed by S–X and after about 2,500 ml of oxygen absorbed by S–Z.

2. Effect of Partial Pressure of Oxygen

The graphs of figure 7 show the amount of carbon monoxide produced by five partial pressures of oxygen when absorbed by pyrogallol solutions prepared according to the old method in three types of pipettes.[2] Since the old method of preparing solutions could not be relied upon to give consistent results from one run to another, these graphs may not show exactly the effect of the type of pipette upon the amount of carbon monoxide produced, although the Orsat contact pipette does show the characteristically high production of carbon monoxide. The graphs may be used to indicate the relative effects of several partial pressures of oxygen ranging from 21 to 100 percent of oxygen at various stages in the life of the solution. The broken lines in figure 7 separate the points into groups according to the partial pressure of oxygen absorbed. They show more clearly the fan-shaped effect that results from plotting amounts of carbon monoxide produced during absorptions of various partial pressures of oxygen versus the degree to which the solution was expended. The same effect was shown in figure 5, although it was less well defined with respect to the total amount of oxygen absorbed in the solutions prepared by the improved method.

In figure 8 is a comparison of the carbon monoxide produced in the absorption of various partial pressures of oxygen by a solution prepared by the old method and one prepared by the improved method. In the latter, the amount of carbon monoxide produced was directly proportional to the partial pressure of oxygen absorbed. In the solution prepared by the old method the carbon monoxide produced increased with the partial pressure of oxygen, but there was not the simple linear relationship that was observed with the improved solution.

Since the volumes of the samples used were constant, the amounts of carbon monoxide formed were directly proportional to the total amount of oxygen absorbed and independent of the partial pressures of oxygen in the samples. This permits a close estimate of the carbon monoxide yield and, therefore, the proper correction for any determined analytical condition.

3. Effect of Temperature of Reaction

Figure 9 illustrates the effect of temperature variations in four different solutions that were prepared according to the improved method. The numbers next to the symbols in these graphs indicate the order in which the analyses were performed. A variation of 7 or 8 deg. C in the temperature of reaction was necessary to change significantly the amount of carbon monoxide formed in the absorption of oxygen by pyrogallol solutions. There was a definite relationship between the temperature of reaction and the amount of carbon monoxide formed, although under most laboratory conditions the effect of temperature changes would be negligible.

4. Effect of Rate of Flow

The formation of carbon monoxide was significantly increased only when the rate of flow of the original sample was less than 20 ml/min, at which rate about 5 minutes was required to make one pass into the solution. So slow a rate would be considered impractical for most volumetric gas analyses. Figure 10 shows the amount of carbon monoxide formed at various rates of flow.

[2] The letters in the upper left-hand corner indicate the type of pipette used. For the key to abbrevatiations, see the legend of figure 2.

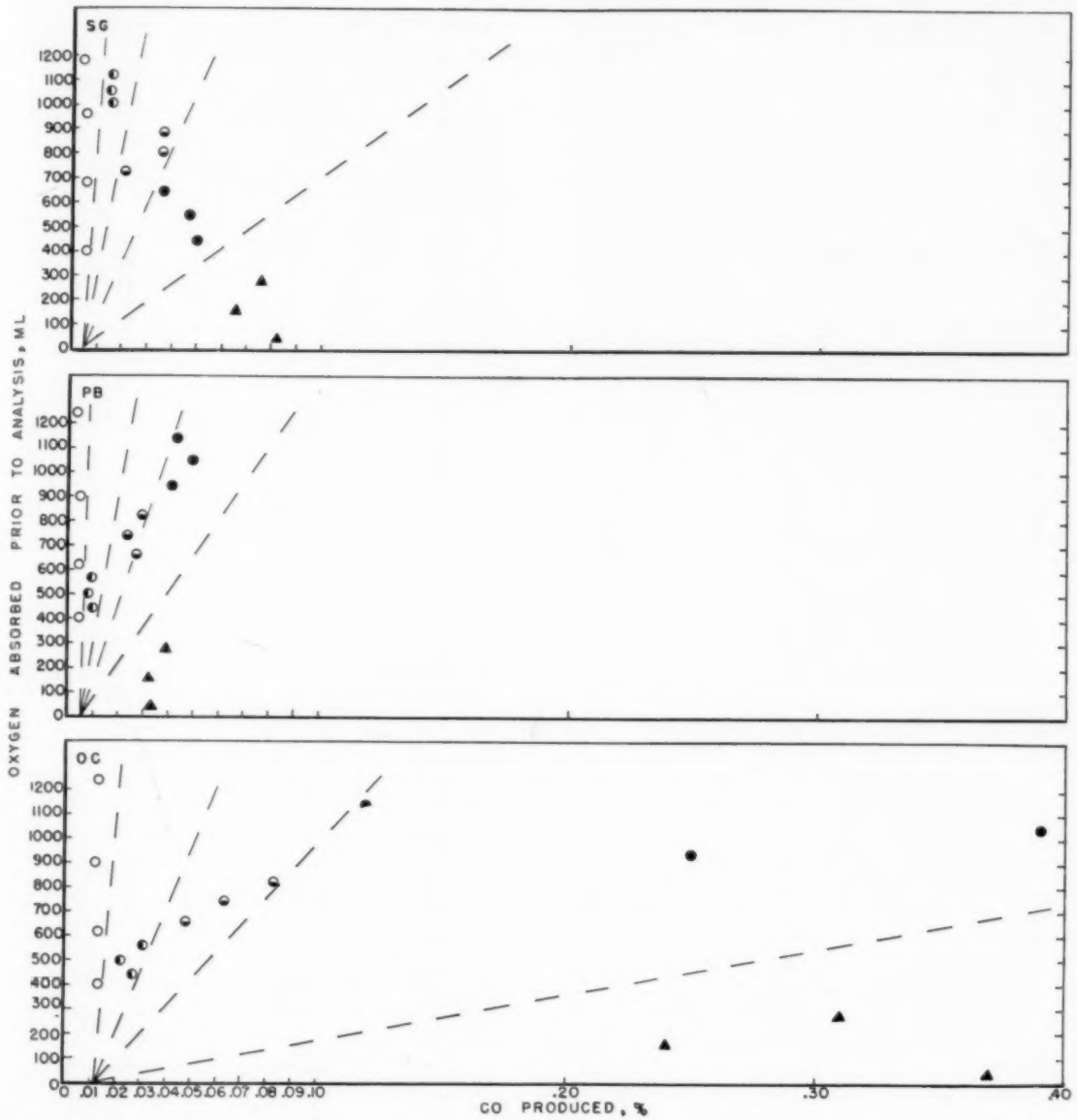

FIGURE 7. *Percentage of carbon monoxide produced in the absorptions of oxygen at various partial pressures, by solutions of the same composition prepared by the old method.*

The type of pipette is given in the upper left-hand corner of each block (see fig. 2). ○, 21% O_2 (air); ◐, 40% O_2 in N_2; ◒, 60% O_2 in N_2; ●, 80% O_2 in N_2; ▲, 100% O_2.

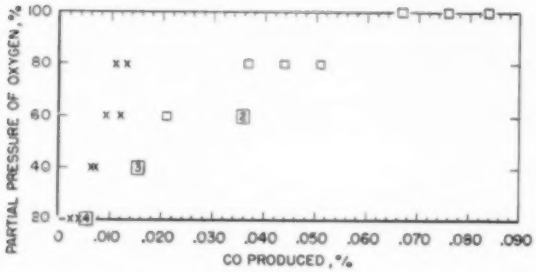

FIGURE 8. *Percentage of carbon monoxide produced in the absorption of oxygen at various partial pressures by two solutions of S–X prepared in a sintered-glass bubbler pipette, one according to the improved method and the other according to the old method.*

Numbers inside of squares indicate the number of points at this location; plain squares indicate one point. X, Improved solution; □, old solution.

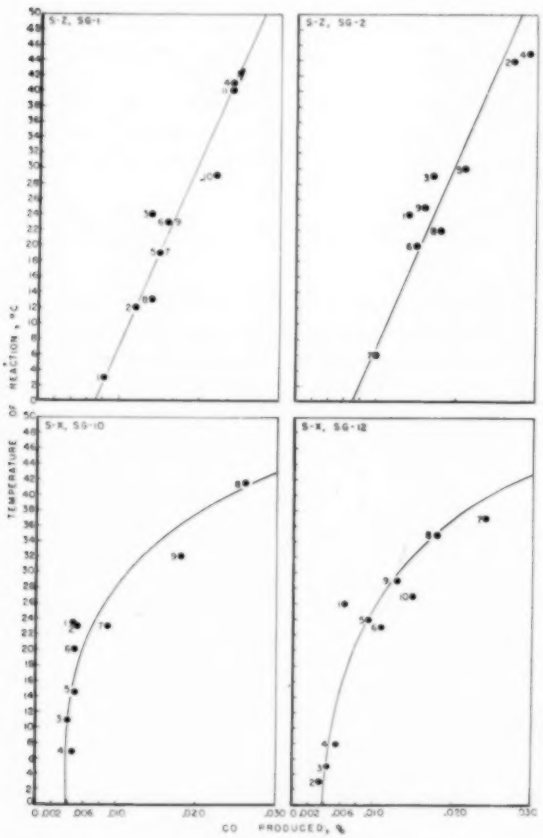

FIGURE 9. *Percentage of carbon monoxide produced at various temperatures of reaction during the absorption from mixtures containing 80 percent of oxygen.*

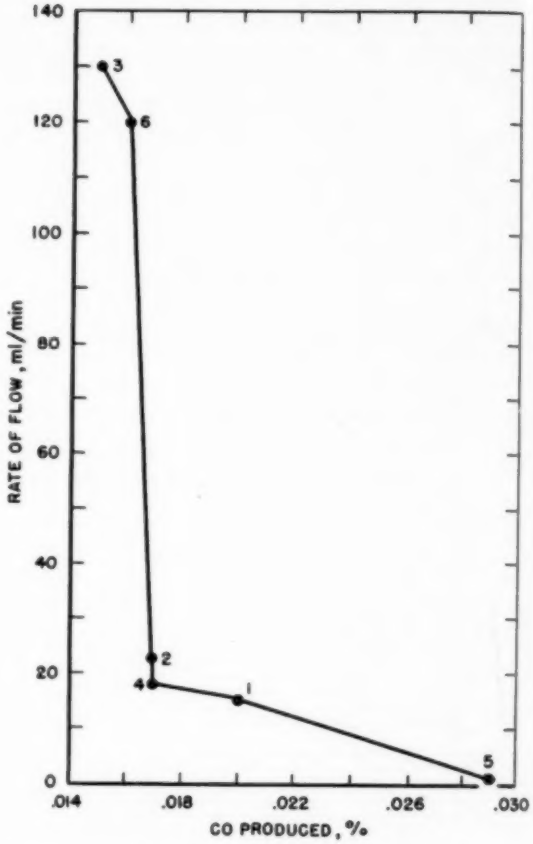

FIGURE 10. *Percentage of carbon monoxide produced at various rates of flow of a mixture containing 80 percent of oxygen into pipette SG–1 containing solution S–X.*

The numbers next to the symbols indicate the order in which the analyses were performed.

It will be shown later in section 6 that the contact type of pipette caused a much greater production of carbon monoxide than did the bubbler type. This indicated that carbon monoxide was formed when high partial pressures of oxygen came in contact with *expended* pyrogallol solution on the glass walls. If this assumption were true, it would follow that a reduction in the rate of flow of the sample would cause a greater production of carbon monoxide in the bubbler type of pipettes, because the oxygen would be in contact longer with the expended solution adhering to the inlet capillary tube leading to the bubbler. This seems to be a logical explanation of the data presented in figure 10.

5. Effect of Number of Passes Into Pyrogallol

The efficiency of oxygen absorption in the platinum-disk bubbler pipette has been previously determined [5]. In the work referred to it was found that in the analysis of a mixture containing 95 percent of oxygen, more than 70 percent of the total oxygen in the sample was removed during the first pass and about 93 percent had been removed after the second pass. It may therefore be assumed that any significant amount of carbon monoxide was formed in the first two passes, since, for any one reagent at one temperature, the partial pressure of oxygen is the most important factor in the formation of carbon monoxide. The graphs on the left of figure 11 show the amount of oxygen absorbed during the number of passes indicated. The graphs on the right show the amount of carbon monoxide formed during those absorptions. In order to exaggerate the effect, *the bubbler was not used* and the sample was passed into the pipette on top of the solution. The weakly alkaline solution S–5 in an absorption from gas containing 80 percent of oxygen absorbed about 10 percent of oxygen on each of the first three passes, and the amount of carbon monoxide formed was almost directly proportional to the oxygen absorbed. Furthermore, absorptions of oxygen in air made with this solution showed no significant amount of carbon monoxide produced after the fourth pass when only about 2 percent of oxygen remained in the residue.

In the absorption of oxygen from air, the strongly alkaline solution, S–7, yielded no significant amount of carbon monoxide after the second pass when about 6 percent of oxygen remained in the residue. When a mixture containing 80 percent of oxygen was absorbed by this solution, erratic results were obtained in the two analyses made with five passes. This may be explained by the fact that about 1,200 ml of oxygen had been previously absorbed and the breaking point in the absorption curve had been reached, causing less efficient absorption of oxygen as well as a larger yield of carbon monoxide.

6. Effect of the Design of the Absorption Pipette

For the determination of the effect of several types of absorption pipettes upon the amount of carbon monoxide produced, the improved method was used in preparing 2 liters of solution S–Z in an Erlenmeyer flask. Two hundred ml of this solution was siphoned, in an atmosphere of nitrogen, into each of the nine pipettes illustrated in figure 2, and absorptions from mixtures of 21 and 60 percent of oxygen were made in each of the pipettes. The carbon monoxide evolved is shown in figure 12. The Orsat contact pipette was the only one that showed any great deviation from the others in the amount of carbon monoxide produced. The sintered-glass bubbler, Branham-Sperling bubbler, and platinum-disk bubbler pipettes produced the smallest amounts of carbon monoxide. The Dennis-Friedrichs pipette may also be included in this group with the note that the carbon monoxide formed might have been slightly less, except that the rate of flow of sample

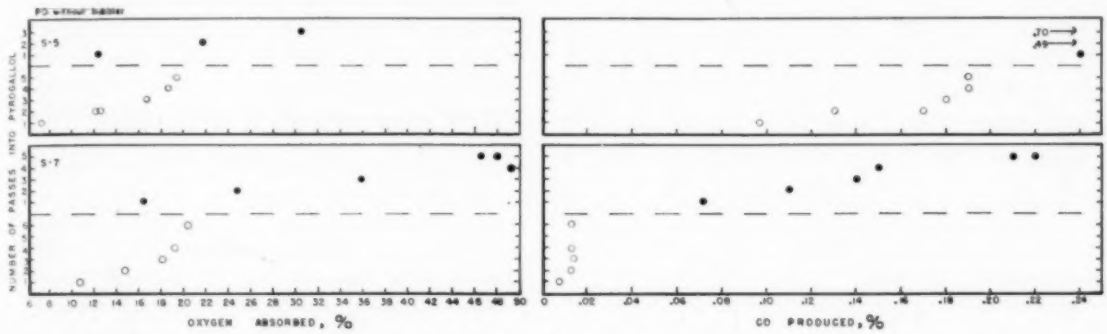

FIGURE 11. *Percentage of carbon monoxide produced and oxygen absorbed during varying numbers of passes of sample into pyrogallol.*

A platinum-disk bubbler pipette was used, but the bubbler was *not* employed in order to exaggerate the desired effect. ○, 21% O_2 (air); ●, 80% O_2 in N_2.

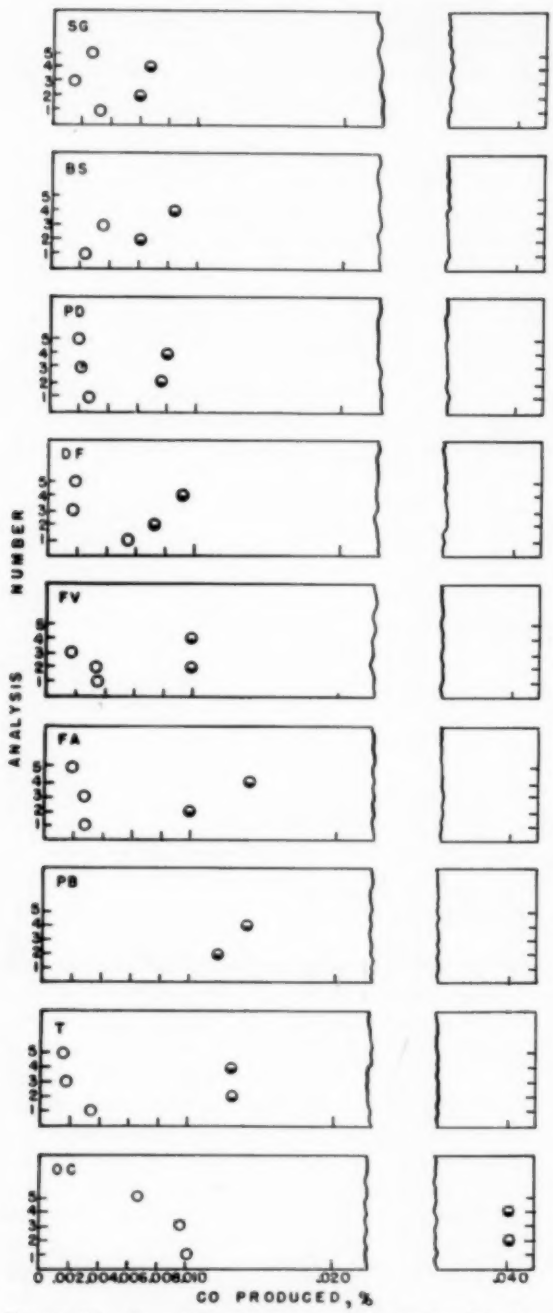

FIGURE 12. *Percentage of carbon monoxide produced during the absorption of oxygen by solution S–BZ in various types of absorption pipettes (see fig. 2).*

Length of stem of bubbler: SG, 18.5 cm; BS, 19 cm; PD, 20 cm; DF, 19 cm; FV, 15 cm; FA, 14 cm; PB, 13 cm; T, 10.5 cm. ○, 20% O_2 (air); ◒, 60% O_2 in N_2.

was reduced to about one-half of the usual rate. This had to be done to prevent the sample from passing to the atmospheric arm of the pipette. Figure 12 shows, in general, that the amount of carbon monoxide formed is a function of the depth of the pyrogallol solution above the bubbler and/or the size of the gas bubbles.

It appears that there may be a correlation between the formation of carbon monoxide and the depth of pyrogallol solution through which the bubbles travel. In the first four pipettes, the distance from the bubbler tip to the top of the solution was 18.5 cm or more, and the carbon monoxide formed in the absorption from a mixture containing 60 percent of oxygen was 0.006 to 0.009 percent; in the next four pipettes where the bubbles traveled from 10.5 to 15 cm in solution, the carbon monoxide produced during similar absorptions was 0.010 to 0.014 percent. When the depth of the solution above the bubbler was decreased the effect became more pronounced, therefore, it appears to be desirable to have at least 18 cm of solution above the bubbler.

For a minimum production of carbon monoxide it is probably also desirable to distribute the sample in fine bubbles. The sintered-glass bubbler, Branham-Sperling bubbler, and platinum-disk bubbler pipettes, which produced the least carbon monoxide, distribute the gas in many very fine bubbles. The Fisher valve-bubbler and Francis auto-bubbler pipettes produce bubbles of an intermediate size, and the plain bubbler pipette has the largest bubbles. The Dennis-Friedrichs pipette is not comparable with the others because of the long spiral up which the bubbles travel, and the Tramm pipette combines the contact method of absorption with the bubbling method. The large amount of carbon monoxide formed in the Orsat contact pipette indicates the importance of distributing the sample in such a way as to prevent its contacting excessive amounts of expended solution.

Shepherd has shown that distributors of fine bubbles are the most efficient for the absorption of oxygen [5]. However, since the bubble size may not affect the carbon monoxide formed by an amount significant to many analyses, some may find it desirable to avoid the trouble caused from plugged distributors by using the plain bubbler with a larger number of passes for the complete absorption of oxygen.

VII. Conclusions

The accuracy, reproducibility, and rapidity of the analytical determination of oxygen by absorption in alkaline pyrogallol may be improved as indicated by this experimental study.

(1) Solutions can be prepared that evolve no significant amount of carbon monoxide during the usual analysis. This is accomplished by the direct addition of a saturated solution of potassium hydroxide to pyrogallol crystals under conditions such that the heat evolved during the solution is dissipated rapidly.

(2) Samples having partial pressures of oxygen higher than 50 percent can be analyzed with the improved solutions without dilution of the sample.

(3) The solution should not be used for analysis after the absorption of 12 volumes of oxygen per volume of solution if high accuracy is desired.

(4) The temperature of the pyrogallol reagent should not exceed 30° C during absorption.

(5) The rate of flow of sample into the pyrogallol should be as rapid as possible and never less than 20 ml/min.

(6) A pipette that disperses the gas in fine bubbles through at least 18 cm of solution is preferable.

It should be emphasized that if the analyst is concerned with amounts of carbon monoxide that are less than about 0.01 percent of the sample, a determination of the carbon monoxide formed should be made after each absorption of oxygen.

The author acknowledges with gratitude the helpful suggestions and advice contributed by Martin Shepherd during this investigation.

VIII. References

[1] J. R. Branham and M. Sucher, J. Research NBS **21,** 63 (1938) RP1113.
[2] M. Shepherd, Anal. Chem. **19,** 77 (1947).
[3] M. Shepherd, BS J. Research **6,** 121 (1931) RP266.
[4] M. Shepherd, J. Research NBS **26,** 351 (1941) RP1382.
[5] M. Shepherd, BS J. Research **4,** 747 (1930) RP177.

WASHINGTON, March 31, 1950.

U. S. Department of Commerce
National Bureau of Standards

Research Paper RP2113
Volume 45, July 1950

Part of the Journal of Research of the National Bureau of Standards

Tracing of Skew Rays

By Donald P. Feder

This paper presents a set of convenient recurrence formulas for the tracing of skew rays by means of a desk calculator. Because of the increased speed and field coverage of modern lenses, it is frequently desirable to trace such rays in making a complete study of an optical system.

The formulas apply to systems of spherical refracting surfaces. The system need not be centered.

Particularly convenient check formulas are available, which need be applied only at the final surface.

A complete study of an optical system appears to demand some knowledge of the behavior of the general or skew rays. A computational process for obtaining this information by tracing such rays, which has proved convenient in practice, will now be described.

It is contemplated that these formulas will be used with a desk calculating machine. When such a calculator is used, twelve numbers per surface must be written down for each ray.

An advantage of the method is the existence of a simple check that need be applied only at the final surface.

Brief derivation. We consider a system of spherical refracting surfaces. The system need not be centered.

We denote the incident and refracted rays by the unit vectors $\boldsymbol{Q}$ and $\boldsymbol{Q}'$, and the radius vector to the center of curvature from the point of incidence by $\boldsymbol{R}$. Bold-faced type will be used to denote vectors.

We define a new vector $\boldsymbol{P}$

$$\boldsymbol{P}=N\ \boldsymbol{Q}\times\boldsymbol{R}. \tag{1}$$

The law of refraction becomes

$$\boldsymbol{P}=N'\ \boldsymbol{Q}'\times\boldsymbol{R}, \tag{2}$$

where N and N' are the refractive indices of the surrounding media.

We can now choose our independent variables from the set of vectors ($\boldsymbol{P}$, $\boldsymbol{Q}$, $\boldsymbol{R}$). Any two of these determine the direction and location of the ray and may be used as independent variables. An obvious choice is the pair $\boldsymbol{Q}$ and $\boldsymbol{R}$, but $\boldsymbol{P}$ and $\boldsymbol{Q}$ yield simpler equations, particularly a simpler transfer.

We eliminate $\boldsymbol{R}$ from eq 1 and 2 in order to obtain $\boldsymbol{Q}'$ as a function of $\boldsymbol{P}$ and $\boldsymbol{Q}$. Multiplying eq 1 vectorially by $\boldsymbol{Q}$, one can obtain $\boldsymbol{R}$, which is then substituted in eq 2. After solving the resulting equation for $\boldsymbol{Q}'$, we obtain

$$\boldsymbol{Q}'=a\boldsymbol{Q}+b\boldsymbol{P}\times\boldsymbol{Q}, \tag{3}$$

where

$$a=\frac{\boldsymbol{P}^2+NN'(\boldsymbol{Q}'\cdot\boldsymbol{R})(\boldsymbol{Q}\cdot\boldsymbol{R})}{NN'\boldsymbol{R}^2}, \tag{4}$$

$$b=\frac{N'(\boldsymbol{Q}'\cdot\boldsymbol{R})-N(\boldsymbol{Q}\cdot\boldsymbol{R})}{NN'\boldsymbol{R}^2}. \tag{5}$$

$(\boldsymbol{Q}\cdot\boldsymbol{R})$ and $(\boldsymbol{Q}'\cdot\boldsymbol{R})$ may be evaluated by squaring eq 1 and 2 respectively. We find

$$N^2(\boldsymbol{Q}\cdot\boldsymbol{R})^2=N^2\boldsymbol{R}^2-\boldsymbol{P}^2 \tag{6}$$

$$N'^2(\boldsymbol{Q}'\cdot\boldsymbol{R})^2=N'^2\boldsymbol{R}^2-\boldsymbol{P}^2 \tag{7}$$

Given $\boldsymbol{P}$ and $\boldsymbol{Q}$, these equations enable us to find $\boldsymbol{Q}'=\boldsymbol{Q}_1$. It remains only to find $\boldsymbol{P}_1$ for the following surface in terms of $\boldsymbol{P}$ and $\boldsymbol{Q}$ at the preceding one.

In figure 1 O and O_1 are the respective centers, and A and A_1 are the points of incidence of the ray. In general the quadrilateral is not plane.

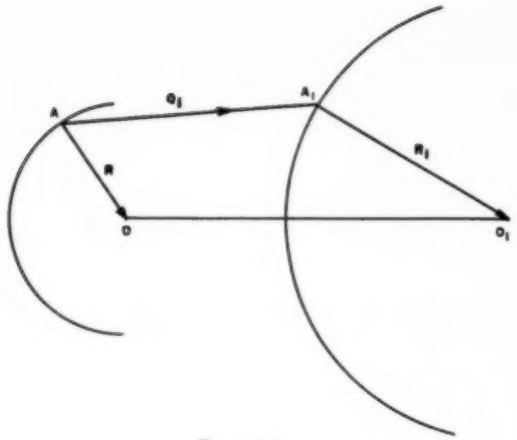

FIGURE 1.

$\boldsymbol{R}$, $\boldsymbol{Q}_1$, and $\boldsymbol{R}_1$ denote vectors.

Denoting the vector from O to O_1 by $\boldsymbol{T}$, one has immediately

$$\boldsymbol{R}_1+\overline{AA_1}\boldsymbol{Q}_1=\boldsymbol{R}+\boldsymbol{T} \tag{8}$$

Multiplying vectorially by $N'\boldsymbol{Q}'=N_1\boldsymbol{Q}_1$, the term in $\overline{AA_1}$ vanishes, and we have

$$\boldsymbol{P}_1=\boldsymbol{P}+\boldsymbol{Q}_1\times\boldsymbol{t} \tag{9}$$

where $\boldsymbol{t}=N_1\boldsymbol{T}$

Summary in scalar form. Since the vast majority of optical systems are centered, let us suppose that $\overline{OO_1}$ lies on the optical axis. We may take the x axis along this line so that $t_y=t_z=0$.

Suppose that $\boldsymbol{Q}=(X, Y, Z)$ and $\boldsymbol{P}=(P_x, P_y, P_z)$ are given in scalar form. Defining the auxiliary constants $r=N|\boldsymbol{R}|$ and $r'=N'|\boldsymbol{R}|$, and writing

$$P^2=P_x^2+P_y^2+P_z^2 \tag{10}$$

$$g^2=r^2-P^2 \tag{11}$$

$$g'^2=r'^2-P^2 \tag{12}$$

$$a=\frac{g'g+P^2}{rr'} \tag{13}$$

$$b=\frac{g'-g}{rr'} \tag{14}$$

$$\left.\begin{aligned} X_1&=aX+b[P_yZ-P_zY]\\ Y_1&=aY+b[P_zX-P_xZ]\\ Z_1&=aZ+b[P_xY-P_yX]\end{aligned}\right\} \tag{15}$$

$$\left.\begin{aligned} P_{1x}&=P_x\\ P_{1y}&=P_y+t_xZ_1\\ P_{1z}&=P_z-t_xY_1\end{aligned}\right\} \tag{16}$$

The signs of g and g' are identical and are positive for surfaces convex toward the entering rays.

Equations 10 through 16 inclusive, form the complete set for systems of spherical surfaces.

One notices that P_x is an invariant of the ray. $P_x=0$ implies that the ray lies in a meridian plane.

Plane surfaces. At a plane refracting surface normal to the optical axis, the refraction equations are greatly simplified.

From eq 1 and 2 by taking $\boldsymbol{R}=\boldsymbol{i}$ one obtains

$$\left.\begin{aligned} N'Y'&=NY\\ N'Z'&=NZ\end{aligned}\right\}, \tag{17}$$

also

$$X'^2=1-Y'^2-Z'^2, \tag{18}$$

and X' is always positive.

Since $\boldsymbol{P}$ does not define the location of the ray at a plane, we introduce a vector $\boldsymbol{F}$, lying in the plane and extending from the axis to the intersection of plane and ray.

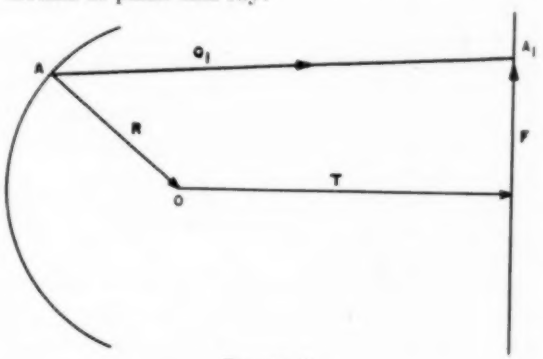

FIGURE 2.

$\boldsymbol{R}$, $\boldsymbol{Q}_1$, $\boldsymbol{F}$, and $\boldsymbol{T}$ denote vectors.

From figure 2 we obtain $\overline{AA_1}\boldsymbol{Q}_1=\boldsymbol{R}+\boldsymbol{T}+\boldsymbol{F}$ and multiplying by $N_1\boldsymbol{Q}_1$ as before, we have

$$\boldsymbol{P}=N_1\boldsymbol{F}\times\boldsymbol{Q}_1+\boldsymbol{t}\times\boldsymbol{Q}_1 \tag{19}$$

where $\boldsymbol{t}=N_1\boldsymbol{T}$. In scalar form, if we take $t_y=t_z=0$

$$\left.\begin{aligned} P_x&=N_1[F_yZ-F_zY_1]\\ P_y&=N_1F_zX_1-t_xZ_1\\ P_z&=-N_1F_yX_1+t_xY_1\end{aligned}\right\} \tag{20}$$

Evidently eq 20 may be used to obtain $\boldsymbol{F}$ in terms of $\boldsymbol{P}$ or conversely. Frequently they are used as initial and final equations as well as at refracting surfaces.

Checking equations. At each surface

$$\left.\begin{aligned}\boldsymbol{P}\cdot\boldsymbol{Q}=\boldsymbol{P}\cdot\boldsymbol{Q}_1=0\\ \boldsymbol{Q}^2=\boldsymbol{Q}_1^2=1\end{aligned}\right\}, \tag{21}$$

from eq 1 or 2. It is important to note that these checks need be applied only at the final surface.

For we have from eq 3 by scalar multiplication

$$\boldsymbol{P}\cdot\boldsymbol{Q}'=a\boldsymbol{P}\cdot\boldsymbol{Q}$$

and similarly from eq 9

$$\boldsymbol{P}_1\cdot\boldsymbol{Q}_1=\boldsymbol{P}\cdot\boldsymbol{Q}_1=a\boldsymbol{P}\cdot\boldsymbol{Q}. \tag{22}$$

Furthermore, since a can be shown to be always nonzero, it follows that if $\boldsymbol{P}\cdot\boldsymbol{Q}$ is nonzero at any point, it remains nonzero. This implies that an error that causes $\boldsymbol{P}\cdot\boldsymbol{Q}$ to differ from zero at any surface will appear at the final surface.

Similarly, if any error is made so that $\boldsymbol{Q}^2-1\neq 0$, the error will appear at the final surface.

In addition one must have at each surface

$$\left.\begin{aligned}a^2+b^2\boldsymbol{P}^2-1=0\\ l^2-\boldsymbol{P}_x^2-P_y^2-P_z^2=0\end{aligned}\right\}. \tag{23}$$

These checks should guarantee the accuracy of the final data, provided no errors are made in the constants.

Using this method, the accuracy of the results is not limited by a particular set of tables. All that is needed is two square roots, and this may be obtained, with any desired accuracy, by the usual iteration formulas. It is very easy to obtain results to 10 significant figures by employing at most a small table.

WASHINGTON, March 30, 1950.

886334—50——5

U. S. Department of Commerce
National Bureau of Standards

Research Paper RP2114
Volume 44, July 1950

Part of the Journal of Research of the National Bureau of Standards

Strength of Heat-Resistant Laminated Plastics up to 300° C *

By Benjamin M. Axilrod and Martha A. Sherman

The flexural properties of samples of glass-fabric laminates were determined for several conditions of heating and testing. The laminates tested were bonded with various resins, including unsaturated-polyester, acrylic, silicone, phenolic, and melamine types. Flexural tests were made under the following conditions: (1) at 25° C and 50-percent relative humidity after 200 hours of heating at a temperature T; (2) at a temperature T after 0.5 hour at the temperature T; (3) at a temperature T after 200 hours at the temperature T; and (4) at 25° C and 50-percent relative humidity without heating prior to testing. The temperature T was 150°, 200°, and 250° C for condition 1; 150°, 200°, 250°, 300°, and 375° C for condition 2; and 150°, 200°, 250°, and 325° C for condition 3.

The one sample of silicone resin laminate tested was superior to the other laminates in retention of flexural properties at temperatures of 250° C or higher. The single phenolic laminate tested showed good retention of flexural properties when tested at elevated temperatures after 0.5 hour of heating. After prolonged heating the behavior of the phenolic sample was much less satisfactory, the strength being almost negligible at 250° C. The sample of melamine laminate was superior to the phenolic in retention of flexural strength after prolonged heating at 200° and 250° C. The polyester laminates lost at least 80 percent of their flexural strength when tested at 250° C. For each laminate and each test condition loss in modulus of elasticity correlated with loss in flexural strength, but the former loss was less than the latter. The results of one test in which duplicate sets of specimens were heated in still air and in rapidly moving air indicate that the loss of flexural properties during prolonged heating may depend on the method of exposing the specimens.

I. Introduction

The mechanical properties of glass-fabric laminates at elevated temperatures are of interest to aircraft designers, as these materials have properties that can be used to advantage in certain applications, such as radomes. Considerable work had been done prior to 1947 on the mechanical properties of various laminates at temperatures in the range of 70° to 100° C [1 to 7],[1] and a few tests were reported at temperatures of 200° C [8]. With the development of higher speed aircraft and guided missiles, there was a demand for information on the mechanical properties of laminated plastics at temperatures much higher than 100° C.

The present investigation was undertaken to determine the flexural properties of promising laminates at temperatures up to 300° C. Commercial resin manufacturers and laminators were informed of the project and invited to submit samples of laminates that could be expected to be heat-resistant. Glass-fabric laminates bonded with various resins including silicone, phenolic, melamine, acrylic, and unsaturated-polyester types were received and tested. This report summarizes the results of the flexural tests, made at room temperature after prolonged heating and also at elevated temperatures after both brief and prolonged heating.

* This investigation was conducted under the sponsorship and with the financial assistance of the National Advisory Committee for Aeronautics and the Air Matériel Command.

[1] Figures in brackets indicate the literature references at the end of this paper.

As testing at temperatures of 300° C presents problems not encountered in testing at room temperature or at 70° to 100° C, a considerable part of the project was devoted to the development of suitable equipment and procedures. These are described in detail in this report.

II. Materials

The materials, submitted in sheets approximately ⅛ in. in thickness, are identified in this report as follows:

Laminate sample	Resin designation
Unsaturated polyester:	
A	Laminac PDL–7–261.
E	Plaskon 911–11.
F	Thalid X–528–10A. C.
C	Paraplex P–43.
Acrylic addition:	
C	BCM monomer and polymethyl methacrylate.
Silicone:	
B	DC 804.
Phenolic:	
H	Redux.
Melamine:	
J	Melmac 405.

All the laminates except the sample *J* were made with Fiberglas 181A fabric; Fiberglas ECC–128 was used in sample *J*. The materials are described in detail, including fabrication conditions, in table 1.

III. Test Procedures

1. Flexural Specimens and Sampling

It is known that the sheet-to-sheet variability, especially in experimental laminates, may be large. A proper sampling plan for the tests at various conditions could give information both as to the average behavior of the sheets of a given sample, and also the variations that might be expected both at standard test conditions and elevated temperatures. Since both the number of sheets and the sizes differed from sample to sample, it was not practical to study sheet-to-sheet variability.

The following sampling plan was adopted: Approximately 80 percent of each sheet of each sample was cut into specimens, which were numbered. The numbered specimens were arranged in a random order and separated into groups of seven each. The plan was to test five specimens from each group with two specimens for use in case of experimental difficulties. The statistical analysis of the results can be greatly facilitated by having the same number of test specimens for each condition.

The flexural specimens were 4 in. long and were machined to a width of 1.00 in., either by dry grinding with a surface grinder or milling with a carbide-tipped cutter.

2. Flexural Test Equipment [2]

The flexural jig and the heated test enclosure are shown in figures 1 and 2 in place in the testing machine. The flexural jig and test enclosure are both suspended from the upper cross-head of the testing machine. The flexural jig, partly disassembled, is shown in figure 3. The base of the flexural jig has slots located so that the support blocks may be bolted in place to give a span of 2,

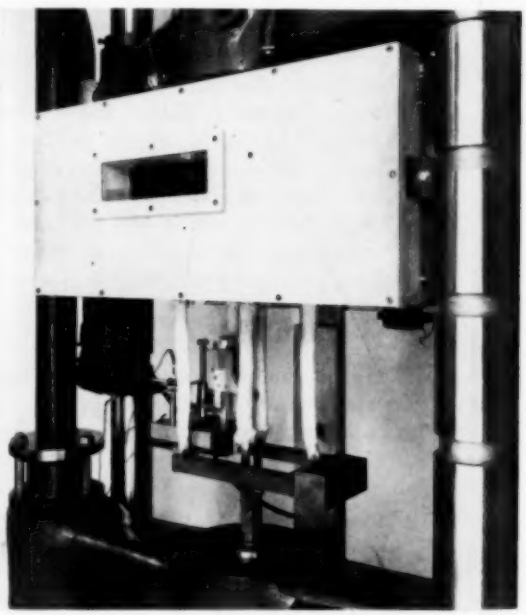

FIGURE 1. *Front view of flexural test enclosure in place in the testing machine.*

The recording deflectometer and selsyn motor are at the left below the enclosure.

[2] Drawings of the flexural test equipment are available from the Organic Plastics Section, National Bureau of Standards, Washington 25, D. C.

TABLE 1. *Description of materials*

	Sample A	Sample E	Sample F	Sample G
Laminator of sample	American Cyanamid Co.	Plaskon Division	Monsanto Chemical Co.	Rohm & Haas Co.
Resin used:				
Trade name and number	Laminac PDL-7-261, B-11	Plaskon 911-11	Thalid X-528-10AC	Paraplex P-43.
Chemical type	Polyester	Polyester	Unsaturated polyester; vinyl type monomers.	Unsaturated polyester-styrene.
Catalyst used with resin:				
Name or type	Luperco ATC[a]	Luperco ATC[a]	LupercoATC [a]	Benzoyl peroxide.
Amount, %	0.5	4	2	1.
Liquid added to resin to prepare it for application to fabric:				
Name	Styrene	None	None	Styrene.
Amount, parts per 100 parts of resin	40			15.
Resin content (by weight) of finished panel:				
Manufacturer's data, %	33±2	31	45	40 to 45.
National Bureau of Standards data, %	35	32	24	42.
Fabric used:				
Identity	Fiberglas 181-A-14	Fiberglas 181-A-14	O. C. C. 181-A-14	Fiberglas 181-38, Finish 114.
Number of plies	12	15	15	12.
Ply arrangement	Parallel	Parallel	Cross	Cross.
Treatment prior to application of resin (drying, etc.)	None	In forced-draft oven for 2 hr at 204° C.	None	None.
Method of applying resin	Dipping	By hand with broad-blade spatula.	Brush	Brush.
Drying of impregnated fabric				
Molding conditions:				
Equipment:				
Heat	Steam	Steam	Steam	Steam.
Pressure	Hydraulic press	Hydraulic press	Platen press	Hydraulic press.
Precure	None	None	None	
Temperature, ° C				104.
Pressure, lb/in.²				5.
Time, min				3.
Cure:				
Temperature, ° C	105, 15 min 125, 10 min	100	100 to 110	145.
Pressure, lb/in.²	10	25	15	50.
Time of heating under pressure, min	25	30	15	5.
Time of cooling under pressure, min	None	None	5	None.
Aftercure	do	do	None	Do.
Sample:				
Area, in.	12 by 22 21 by 22	12 by 12	12 by 12	10 by 10.
Thickness, in.	0.11 to 0.13 0.11 to 0.13	0.13 to 0.14	0.09 to 0.12	0.13 to 0.15.
Number of sheets	1 1	10	4	14.

[a] Luperco ATC consists of 50% benzoyl peroxide and 50% tricresyl phosphate.

TABLE 1. *Description of materials*—Continued

	Sample C	Sample B	Sample H	Sample J
Laminator of sample	E. I. du Pont de Nemours & Co.	Dow Corning Corp.	Rohm & Haas Co.	Formica Co.
Resin used:				
Trade name and number	BCM monomer, 60%; polymethylmethacrylate HG–4, 40%.	DC 804	Redux	Melmac 405.
Chemical type	Acrylic addition type; thermosetting.	Silicone	Phenolic	Melamine-formaldehyde.
Catalyst used with resin:				
Name or type	Residual benzoyl peroxide in polymethylmethacrylate.		None	None.
Amount, %				
Liquid added to resin to prepare it for application to fabric:				
Name	Methyl ethyl ketone	Toluene	None	Water, 95%; butyl alcohol, 5%.
Amount, parts per 100 parts of resin	135	67		67.
Resin content (by weight) of finished panel:				
Manufacturer's data, %	56	39	40 to 45	42 to 47.
National Bureau of Standards data, %	62		44	46.
Fabric used:				
Identity	Fiberglas 181–A–13	Fiberglas 181–A–12	Fiberglas 181–38, Finish 114.	Fiberglas ECC–128; sizing pyrolyzed to light brown.
Number of plies	6	11	12	13.
Ply arrangement	Cross	Cross	Cross	Parallel.
Treatment prior to application of resin (drying, etc.)	None		None	
Method of applying resin	Continuous dip and squeeze roll.	Dipping	Dipping	Dipping.
Drying of impregnated fabric	Solvent evaporated in forced-draft oven at 43° C.		Air dried for 30 min at room temperature, 15 to 18 min at 104° C in forced-draft oven.	
Molding conditions:				
Equipment:				
Heat	Steam	Steam	Steam	Steam.
Pressure	Hydraulic press	Hydraulic press	Hydraulic press	Hydraulic press.
Precure	None			None.
Temperature, °C		110	145	
Pressure, lb/in.[2]		Atmospheric	15	
Time, min		10	1	
Cure:				
Temperature, °C	110	175	145	125 to 124, 20 min. 142 to 147, 20 min.
Pressure, lb/in.[2]	50	900	50	1,100.
Time of heating under pressure, min	15	75	15	About 40 min.
Time of cooling under pressure, min	3	30	None	15.
Aftercure	None	90° C, 15 hr [b] 130° C, 4 hr 160° C, 4 hr 190° C, 16 hr 250° C, 4 hr	do	None.
Sample:				
Area, in	14 by 19 .. 11 by 12	12 by 12	10 by 10	21 by 36.
Thickness, in	0.10 to 0.13 .. 0.10 to 0.13	0.13 to 0.14	0.13 to 0.15	0.12 to 0.13.
Number of sheets	3 .. 2	3	14	1.

[b] Mechanical convection oven.

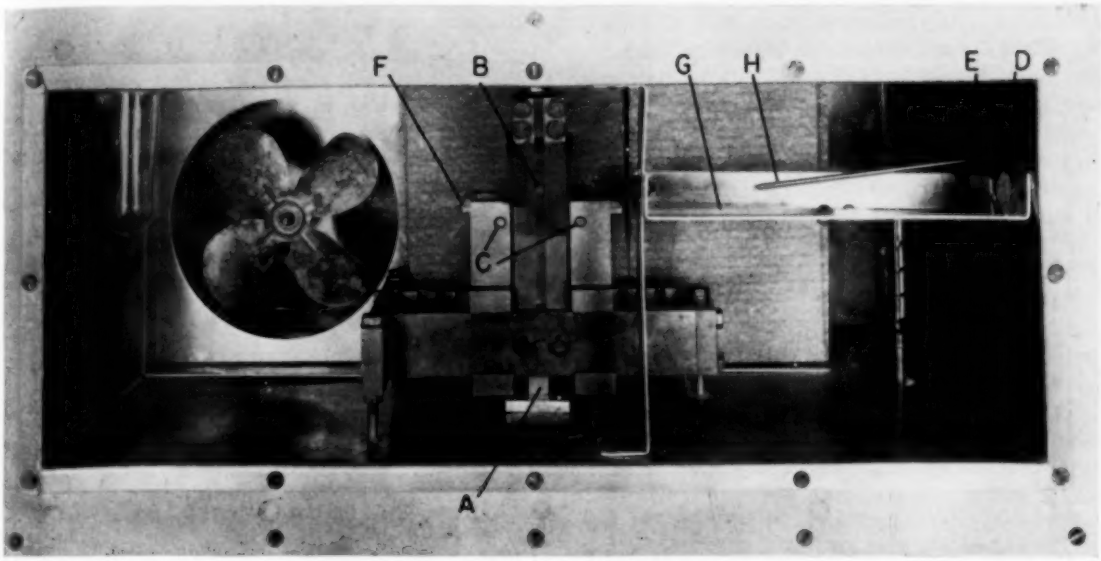

FIGURE 2. *Interior view of test enclosure.*

A, Loading stirrup; *B*, loading edge in loading stirrup; *C*, contact edges in support block; *D*, loading port; *E*, hole for push rod; *F*, specimen in jig; *G*, specimen in tray; *H*, stem of dial-type thermometer.

3, 4, or 5 in. The loading stirrup, attached to the lower cross-head of the testing machine (fig. 1), is centered by having the ends of the drill rod used for the loading edge extend into slots in the flexural jig suspension (see figs. 2 and 3). The flexural jig is made of steel, nickel-plated to avoid corrosion.

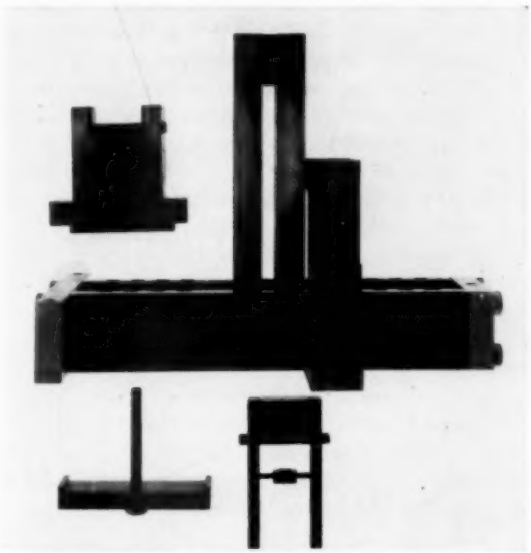

FIGURE 3. *Flexural jig partly disassembled.*

The left support block and clamp and the loading stirrup have been removed and rotated through 90°.

The deflection of the specimen is measured by a Southwark-Peters deflectometer, model PD–1, coupled to a recorder on the testing machine to produce load-deflection graphs. The deflectometer, located below the test enclosure (fig. 1), is supported by a platform attached to the flexural jig base. A glass push rod touching the lower side of the specimen operates the deflectometer; this rod is centered by a guide in the loading stirrup (fig. 3).

The test enclosure has an asbestos board exterior, a sheet aluminum interior, and Fiberglas insulation about 1.75 in. thick. The interior is divided into two compartments by an aluminum partition; the front compartment is the test chamber and the rear compartment contains a bank of five 250-w strip heaters. A fan operating continuously draws air past the heaters and blows it into the test chamber. After a number of tests had been made, it was found desirable to place two layers of ¼-in.-thick asbestos board in front of the partition (fig. 2) to improve the temperature distribution within the test chamber.

The specimens are inserted with a spatula-like

holder through a loading port and then placed side by side on an aluminum specimen tray, visible at the right of figure 2. This tray holds five 1-in.-wide specimens. The specimens are manipulated into place in the flexural jig by push rods inserted into holes in the front and right side of the enclosure. In figure 2 one specimen is shown in place in the flexural jig and one in the specimen tray. After a test the specimen is removed from the flexural jig with a pair of tongs inserted through a port in the left side of the enclosure. The operation of the equipment is aided by a double-paned Pyrex glass window and a projection bulb located inside the enclosure. To avoid failure of the phenolic plastic socket or the bulb, the latter is operated at lower than rated voltage by means of a variable auto transformer, and the socket is attached to the outer wall of the enclosure.

Preliminary temperature measurements were made with thermocouples located inside and on the surface of specimens in both the specimen tray and in the flexural jig. It was found that a specimen came to temperature equilibrium within 10 to 15 min after insertion in the enclosure. Before the asbestos board was added to the partition, the temperature of a specimen in the tray was appreciably less than that of a specimen in the flexural jig, the differences amounting to 3 deg and 7 deg C at enclosure temperatures of 150° and 250° C, respectively. The difference was reduced to 3 deg C at 250° C by insertion of the asbestos board.

A fine mesh screen (fig. 2) was wrapped around the upper part of the flexural jig to keep particles of Fiberglas or resin out of the guides for the loading stirrup.

In testing at elevated temperatures the gaseous products given off by some of the specimens were a source of trouble, as the testing machine was located in a controlled atmosphere room in which the air was recirculated. The problem became more serious as the test temperature was increased. An exhaust pipe equipped with a blower was finally attached to the box; it was necessary to control the amount of air drawn from the enclosure by means of a valve in the exhaust pipe, as otherwise the temperature of the enclosure could not be maintained constant.

3. Flexural Test Procedure

(a) Temperature Conditions

Sets of specimens of the samples were tested at 25° C after heating at temperatures of 150°, 200°, and 250° C for 200 hr. Other sets of specimens were tested at an elevated temperature T after 0.5 hr or 200 hr at the temperature T. The temperatures ranged up to 375° C in the 0.5-hr tests and 325° C in the 200-hr tests. Each sample was not tested at each set of conditions; in some instances the samples were badly weakened at moderate test conditions, and in other instances sufficient material was not available.

Two control sets of specimens of each sample were tested at 25° C and 50-percent relative humidity. One set was tested at the beginning of the testing program, the other set about 7 mo later, near the end of the tests.

In heating the specimens for 200 hr, a circulating-air oven was used with each specimen in an open wide-mouthed glass bottle of 2-in. diameter and 4-in. height. In one experiment specimens were also placed on asbestos board laid on the oven shelf in order to compare the effect of heating in still air with heating in rapidly moving air. For convenience, the 200-hr heating period was interrupted at about 96 hr, and the specimens were allowed to cool in the glass containers for about 18 hr; the heating was then continued for about 103 hr. The specimens were transferred to the heated test enclosure 1 hr prior to testing; in making the transfer the specimens were transported to the immediate vicinity of the test enclosure in their containers to minimize cooling; transfer from the container into the test enclosure took a few seconds. During all the 200-hr heating periods the oven temperature was recorded with a Brown recording potentiometer and a thermocouple.

In the tests at elevated temperatures after the specimens were heated 0.5 hr, it was considered that the thermal shock when a cold specimen was placed on the hot metal specimen tray might weaken the specimens. Accordingly, in some tests the specimen tray was covered with a sheet of $\frac{1}{16}$-in.-thick asbestos paper.

In tests at 25° C and 50-percent relative humidity, the specimens were normally conditioned for 7 days prior to test in a room whose atmosphere was controlled at the above values.

(b) Flexural Test Conditions

The flexural jig span was set for 2 in. The actual span was determined at 25° C with screw micrometer calipers. The contact edges of the supporting and loading pieces were all of ¼-in.-diameter drill rod. The rate of loading was maintained at 0.04 in./min in all tests.

(c) Calculation of Flexural Data

In calculations of tests at elevated temperatures the specimen dimensions obtained at 25° C and 50-percent relative humidity were used; however, the span was corrected for change with temperature, assuming a thermal expansivity of 12×10^{-6} per deg C for the metal in the jig. The stress range chosen for calculating the flexural secant modulus of elasticity values was about one-half to two-thirds of the flexural strength at the test condition concerned.

(d) Resin Content and Loss of Weight on Heating

The resin content was determined for three sets of flexural specimens, except for the laminate made with the silicone resin which could not be completely burned off. The initial weights were determined after the specimens were conditioned for at least 7 days at 25° C and 50-percent relative humidity. The resins were removed from the specimens by heating in a muffle furnace.

The weight loss after 200 hr of heating was determined by weighing some of the sets of specimens prior to heating and reweighing after the specimens were reconditioned 7 days at 25° C and 50-percent relative humidity.

(e) Tolerances on Temperatures and Times of Heating

The temperature in the circulating-air oven was controlled at the nominal value to within ±5° C during the 200-hr heating period. In the heating at 325° C in a muffle furnace, the temperature fluctuations were ±10 deg C relative to 325° C.

In the test chamber the average temperature for each set of five specimens noted at the specimen at the start of the flexural test was within ±3 deg C of the test temperature reported in tables 2 and 3 with only one exception. The latter occurred in testing sample *B* at approximately 375° C after heating for 0.5 hr, the average test temperature being 368° C. In more than 90 percent of the tests the average test temperature was within 2 deg C of the desired value. The individual test temperatures were within -5 deg and $+3$ deg C of the nominal values except for the tests at 375° C for which the range was 367° to 381° C.

In the tests at a temperature *T* after 0.5 hr at the temperature *T*, the actual time of heating at the start of the flexural tests was 30 to 35 min. In the 200-hr tests, the total time of heating was 200 ± 1 hr.

886334—50——6

TABLE 2. *Flexural strength data for specimens of glass-fabric laminates tested under various conditions of temperature and heating* [a]

Temperature of heating	Special conditions	Unsaturated polyester resin laminates											
		Laminate A			Laminate E			Laminate F			Laminate G		
		Mean	Range	Percentage of control mean	Mean	Range	Percentage of control mean	Mean	Range	Percentage of control mean	Mean	Range	Percentage of control mean
		FLEXURAL STRENGTH OF CONTROL SPECIMENS AT 25° C (AFTER AT LEAST 7 DAYS AT 25° C AND 50% RELATIVE HUMIDITY)											
°C		10^3 lb/in.^{2}	10^3 lb/in.^{2}		10^3 lb/in.^{2}	10^3 lb/in.^{2}		10^3 lb/in.^{2}	10^3 lb/in.^{2}		10^3 lb/in.^{2}	10^3 lb/in.^{2}	
None	A. First set (Oct. 1948)	27.1	24.6 to 29.9		58.8	56.6 to 61.8		49.8	47.1 to 52.4		53.7	47.1 to 64.4	
Do.	B. Second set (Apr. 1949)	27.9	25.0 to 31.2		59.2	58.2 to 60.6		50.8	48.4 to 52.9		51.3	49.5 to 53.4	
Do.	Control mean	27.5			59.0			50.3			52.5		
		FLEXURAL STRENGTH OF SPECIMENS AT 25° C AFTER 200 HR OF HEATING [b] (RECONDITIONED 7 DAYS AT 25° C AND 50% RELATIVE HUMIDITY, UNLESS OTHERWISE NOTED)											
150		25.8	23.4 to 28.1	94	57.7	51.0 to 63.1	98	49.6	48.1 to 51.7	99	43.6	40.1 to 49.3	83
150	Not reconditioned [c]	28.4	26.0 to 30.9	103	60.2	56.5 to 64.4	102	52.1	49.7 to 54.7	104	41.1	37.6 to 46.9	78
200		20.4	17.9 to 22.3	74	40.8	35.7 to 44.9	69				26.6	24.4 to 30.3	51
200	Not heated in bottles [d]	17.8	16.7 to 19.4	65	37.0	34.4 to 40.5	63				21.4	18.3 to 24.3	41
250		3.6	3.3 to 4.1	13	9.6	7.3 to 10.6	16	3.5	2.9 to 4.2	7	3.0	2.8 to 3.4	6
		FLEXURAL STRENGTH OF SPECIMENS AT A TEMPERATURE T AFTER 0.5 HR AT THE TEMPERATURE T											
150		9.2	8.4 to 9.6	33	20.1	18.0 to 21.2	34	12.0	11.0 to 12.8	24	6.2	4.9 to 7.4	12
200		6.1	5.8 to 6.3	22	10.7	9.9 to 11.4	18	7.4	6.4 to 8.9	15	4.9	4.3 to 6.3	9
250		5.4	4.7 to 6.2	20	7.7	7.1 to 8.0	13	5.8	5.3 to 6.6	12	3.6	3.3 to 4.1	7
250	Abestos-covered tray [e]	5.0	4.7 to 5.4	18	7.8	7.4 to 8.4	13				4.0	3.6 to 4.6	8
300		3.5	3.2 to 3.9	13	5.4	5.2 to 5.6	9	[f] 4.4	[f] 3.1 to 5.1	[f] 9			
300	Asbestos-covered tray [e]	3.2	3.1 to 3.4	12	5.5	5.2 to 5.9	9	5.3	4.7 to 5.7	11			
375	do												
		FLEXURAL STRENGTH OF SPECIMENS AT A TEMPERATURE T AFTER 200 HR AT THE TEMPERATURE T [b]											
150		14.7	14.5 to 14.8	53	28.9	27.2 to 30.6	49	24.1	23.6 to 25.0	48	7.1	6.2 to 7.9	14
200		6.4	6.2 to 6.7	23	18.2	17.1 to 19.4	31	17.4	16.6 to 18.3	35	3.4	3.3 to 3.5	6
250		2.1	1.7 to 2.3	8	9.4	8.6 to 10.1	16	2.2	2.1 to 2.4	4			
325	(g)												

See footnotes at end of table.

TABLE 2. *Flexural strength data for specimens of glass-fabric laminates tested under various conditions of temperature and heating* [a]—Continued

Temperature of heating	Special conditions	Acrylic laminate C			Silicone laminate B			Phenolic laminate H			Melamine laminate J		
		Mean	Range	Percentage of control mean [b]	Mean	Range	Percentage of control mean	Mean	Range	Percentage of control mean	Mean	Range	Percentage of control mean
	FLEXURAL STRENGTH OF CONTROL SPECIMENS AT 25° C (AFTER AT EAST 7 DAYS AT 25° C AND 50% RELATIVE HUMIDITY)												
°C		10^3 lb/in.^{2}	10^3 lb/in.^{2}		10^3 lb/in.^{2}	10^3 lb/in.^{2}		10^3 lb/in.^{2}	10^3 lb/in.^{2}		10^3 lb/in.^{2}	10^3 lb/in.^{2}	
None	A. First set (Oct. 1948)	24.3	23.7 to 25.1		28.9	28.2 to 29.7		44.9	35.0 to 50.6		51.6	50.2 to 53.4	
Do	B. Second set (Apr. 1949)	26.8	25.1 to 28.4		29.6	27.7 to 31.3		48.2	42.0 to 53.6		51.5	50.0 to 52.8	
Do	Control mean				29.2			46.5			51.6		
	FLEXURAL STRENGTH OF SPECIMENS AT 25° C AFTER 200 HR OF HEATING [b] (RECONDITIONED 7 DAYS AT 25° C AND 50% RELATIVE HUMIDITY, UNLESS OTHERWISE NOTED)												
150		28.2	26.8 to 29.4	116(A)	27.7	26.2 to 30.3	95	40.1	36.4 to 42.6	86	33.8	31.8 to 35.0	66
150	Not reconditioned [c]	31.7	27.6 to 34.9	130(A)	28.0	26.6 to 29.1	96	40.3	36.3 to 43.3	87	31.6	31.3 to 32.1	61
200								15.0	13.2 to 16.8	32	26.4	25.7 to 28.4	51
200	Not heated in bottles [d]							9.5	8.6 to 10.4	20	26.0	25.1 to 26.8	50
250					26.4	25.2 to 27.7	90	<0.2			17.6	16.8 to 18.4	34
	FLEXURAL STRENGTH OF SPECIMENS AT A TEMPERATURE *T* AFTER 0.5 HR AT THE TEMPERATURE *T*												
150		3.4	2.9 to 4.2	14(A)	12.6	11.3 to 13.7	43	41.9	39.7 to 44.4	90	37.2	36.4 to 38.1	72
200								35.3	28.2 to 40.6	76	26.5	24.8 to 27.4	51
250					10.9	10.1 to 11.9	37	23.9	21.5 to 28.7	51	22.1	21.4 to 22.7	43
250	Asbestos-covered tray [e]	0.47	0.42 to 0.51	1.8(B)				24.8	22.6 to 26.4	53	22.4	21.8 to 23.5	43
300					[f] 10.1	[g] 9.6 to 10.9	[g] 35	19.8	17.4 to 21.7	43	20.5	19.2 to 22.6	40
300	Asbestos-covered tray [e]				10.5	10.3 to 10.8	36	20.5	17.0 to 25.3	44	19.0	18.4 to 19.4	37
375	do				[f] 9.8	[g] 8.8 to 10.6	[g] 34	14.7	12.3 to 16.4	32	[g] 2.0	[g] 1.4 to 2.5	[g] 4
	FLEXURAL STRENGTH OF SPECIMENS AT A TEMPERATURE *T* AFTER 200 HR AT THE TEMPERATURE *T* [b]												
150		4.2	2.9 to 5.4	17(A)	14.3	13.4 to 15.7	49	39.1	36.2 to 42.6	84	30.3	29.4 to 32.3	59
200								10.9	10.4 to 11.9	23	23.3	23.0 to 24.2	45
250					13.4	12.7 to 14.0	46	0.55	0.51 to 0.59	1.2	15.6	14.7 to 17.4	30
325	(h)				9.8	9.2 to 10.4	34				[g] 1.5	[g] 1.5 to 1.6	[g] 3

[a] Specimens approximately ⅛ in. thick and 1 in. wide tested at 0.04 in./min relative head motion with a span of 2.0 in. Each value is the average for five specimens, unless otherwise noted. Specimens taken at random from the sheets, unless otherwise noted.

[b] Unless otherwise noted, all specimens that were heated for 200 hr were heated in open wide-mouthed bottles placed in a circulating-air oven.

[c] After removal from the oven, specimens kept over calcium chloride for 24 hr prior to testing.

[d] Specimens laid on asbestos board on oven shelf.

[e] The normal tray is an aluminum tray. The asbestos-covered tray is the same aluminum tray covered with asbestos paper about 1/16 in. thick. Unless otherwise noted, all tests at elevated temperature were made with the normal tray.

[f] Specimens not randomly selected but taken from at least three sheets.

[g] A muffle furnace controlled at 325° ±10° C was used for conditioning these specimens.

[h] The flexural strengths for the first and second controls differ significantly for this sample. The test results for various conditions were referred to the data for the control tested at nearly the same time; this is indicated by (A) or (B) following the percentage.

[i] Four specimens.

[j] Two specimens.

TABLE 3. *Secant modulus of elasticity for specimens of glass-fabric laminates tested under various conditions of temperature and heating* [a]

Temperature of heating	Special conditions	Secant modulus of elasticity in flexure															
		Unsaturated polyester resin laminates								Acrylic laminate C		Silicone laminate B		Phenolic laminate H		Melamine laminate J	
		Laminate A		Laminate E		Laminate F		Laminate G									
		Mean	Range	Mean	Range	Mean	Range	Mean	Range	Mean	Range	Mean	Range	Mean	Range	Mean	Range
MODULUS OF ELASTICITY OF CONTROL SPECIMENS AT 25° C (AFTER AT LEAST 7 DAYS AT 25° C AND 50% RELATIVE HUMIDITY)																	
		0 to 2,500 lb/in.²		0 to 10,000 lb/in.²		0 to 10,000 lb/in.²		0 to 4,000 lb/in.²		0 to 2,700 lb/in.²		0 to 5,000 lb/in.²		0 to 7,500 lb/in.²		0 to 10,000 lb/in.²	
°C		10^6 lb/in.²	10^6 lb/in.²	10^6 lb/in.²	10^6 lb/in.²	10^6 lb/in.²	10^6 lb/in.²	10^6 lb/in.	10^6 lb/in.	10^6 lb/in.²	10^6 lb/in.²	10^6 lb/in.²	10^6 lb/in.²	10^6 lb/in.²	10^6 lb/in.²	10^6 lb/in.²	10^6 lb/in.²
None	A. First set (Oct. 1948).	2.72	2.52 to 2.85	3.43	3.34 to 3.48	3.87	3.77 to 3.97	2.68	2.34 to 3.24	1.40	1.35 to 1.54	2.11	1.98 to 2.21	2.55	2.19 to 2.84	3.31	3.25 to 3.38
Do	B. Second set (Apr. 1949).	2.80	2.61 to 3.19	3.38	3.29 to 3.56	3.86	3.76 to 3.96	2.54	2.41 to 2.60	1.41	1.33 to 1.49	2.04	1.97 to 2.12	2.64	2.29 to 3.01	3.26	3.14 to 3.39
Do	Control mean	2.76		3.41		3.87		2.61		1.40		2.08		2.59		3.29	
		0 to 4,000 lb/in.²		0 to 15,000 lb/in.²		0 to 20,000 lb/in.²		0 to 15,000 lb/in.²		0 to 10,000 lb/in.²		0 to 7,500 lb/in.²		0 to 10,000 lb/in.²		0 to 15,000 lb/in.²	
Do	A	2.71	2.52 to 2.85	3.43	3.34 to 3.48	3.85	3.71 to 3.91	2.68	2.34 to 3.24	1.39	1.35 to 1.54	2.10	1.98 to 2.20	2.55	2.19 to 2.84	3.29	3.21 to 3.37
Do	B	2.80	2.61 to 3.19	3.34	3.25 to 3.50	3.83	3.72 to 3.96	2.51	2.41 to 2.60	1.41	1.33 to 1.49	2.03	1.96 to 2.12	2.62	2.29 to 3.00	3.21	3.13 to 3.31
Do	Control mean	2.75		3.39		3.84		2.60		1.40		2.07		2.58		3.25	
		0 to 5,000 lb/in.²		0 to 20,000 lb/in.²		0 to 40,000 lb/in.²		0 to 20,000 lb/in.²		0 to 20,000 lb/in.²		0 to 10,000 lb/in.²		0 to 15,000 lb/in.²		0 to 20,000 lb/in.²	
Do	A	2.70	2.52 to 2.85	3.43	3.34 to 3.48	3.69	3.56 to 3.82	2.67	2.34 to 3.24	1.30	1.25 to 1.34	2.08	1.98 to 2.16	2.55	2.19 to 2.84	3.26	3.18 to 3.32
Do	B	2.80	2.61 to 3.19	3.30	3.20 to 3.49	3.70	3.64 to 3.83	2.50	2.40 to 2.60	[c]1.32	[c]1.26 to 1.44	2.02	1.94 to 2.11	2.58	2.25 to 2.99	3.20	3.13 to 3.29
Do	Control mean	2.75		3.37		3.69		2.59		1.31		2.05		2.56		3.23	
		0 to 8,000 lb/in.²		0 to 40,000 lb/in.²				0 to 30,000 lb/in.²				0 to 20,000 lb/in.²		0 to 20,000 lb/in.²		0 to 30,000 lb/in.²	
Do	A	[b]2.69		3.36	3.25 to 3.40			2.63	2.32 to 3.19			1.98	1.87 to 2.07	2.51	2.16 to 2.82	3.15	3.09 to 3.23
Do	B	[b]2.79		3.22	3.07 to 3.44			2.46	2.37 to 2.57			1.92	1.84 to 2.01	2.56	2.24 to 2.94	3.12	3.07 to 3.21
Do	Control mean	2.74		3.29				2.55				1.95		2.53		3.14	

		0 to 10,000 lb/in.²						0 to 40,000 lb/in.²								0 to 30,000 lb/in.²			
Do	A	2.68	2.53 to 2.85					2.59	2.27 to 3.15							2.48	2.13 to 2.78		
Do	B	2.78	2.56 to 3.17					2.42	2.26 to 2.54							2.53	2.19 to 2.94		
Do	Control mean	2.73						2.51								2.50			
		0 to 20,000 lb/in.²																	
Do	A	2.58	2.45 to 2.80																
Do	B	2.60	2.32 to 2.84																
Do	Control mean	2.59																	

MODULUS OF ELASTICITY OF SPECIMENS AT 25° C AFTER 200 HR OF HEATING [4] (RECONDITIONED 7 DAYS AT 25° C AND 50% RELATIVE HUMIDITY, UNLESS OTHERWISE NOTED)

		0 to 10,000 lb/in.²		0 to 20,000 lb/in.²		0 to 20,000 lb/in.²		0 to 20,000 lb/in.²		0 to 10,000 lb/in.²		0 to 10,000 lb/in.²		0 to 15,000 lb/in.²		0 to 15,000 lb/in.²	
150	Not reconditioned [5]	2.60	2.38 to 2.91	3.14	3.11 to 3.18	3.56	3.51 to 3.67	2.40	2.33 to 2.47	1.37	1.32 to 1.49	2.03	1.97 to 2.06	2.50	2.30 to 2.71	2.42	2.35 to 2.47
		2.70	2.54 to 2.97	3.30	3.13 to 3.40	3.70	3.59 to 3.86	2.36	2.23 to 2.50	1.48	1.26 to 1.60	1.98	1.87 to 2.16	2.42	2.33 to 2.61	2.44	2.37 to 2.51
		0 to 20,000 lb/in.²		0 to 40,000 lb/in.²		0 to 40,000 lb/in.²		0 to 30,000 lb/in.²		0 to 20,000 lb/in.²		0 to 20,000 lb/in.²		0 to 30,000 lb/in.²		0 to 30,000 lb/in.²	
150	do [5]	2.54	2.31 to 2.84	3.08	3.02 to 3.17	3.29	3.23 to 3.39	2.37	2.28 to 2.46	1.34	1.29 to 1.45	1.91	1.87 to 1.96	2.44	2.27 to 2.70	2.14	2.04 to 2.19
		2.67	2.51 to 2.87	3.23	3.08 to 3.35	3.46	3.38 to 3.59	2.29	2.17 to 2.45	1.43	1.22 to 1.53	1.88	1.77 to 2.06	[6] 2.33	[6] 2.24 to 2.47	1.97	1.89 to 2.04
		0 to 10,000 lb/in.²		0 to 20,000 lb/in.²				0 to 15,000 lb/in.²						0 to 7,500 lb/in.²		0 to 15,000 lb/in.²	
200	Not heated in bottles [7]	2.43	2.22 to 2.66	2.81	2.75 to 2.92			2.12	1.75 to 2.65					1.72	1.59 to 1.88	2.06	2.00 to 2.10
		2.21	2.02 to 2.38	2.73	2.60 to 2.98			1.55	1.34 to 1.85					1.28	1.08 to 1.57	2.01	1.93 to 2.11
		0 to 2,500 lb/in.²		0 to 5,000 lb/in.²		0 to 2,500 lb/in.²		0 to 2,500 lb/in.²				0 to 20,000 lb/in.²				0 to 10,000 lb/in.²	
250		1.38	1.10 to 1.55	1.62	1.39 to 1.89	2.16	1.72 to 2.54	0.91	0.67 to 1.25			1.84	1.78 to 1.87	[8]		1.89	1.80 to 1.95

See footnotes at end of table.

TABLE 3. *Secant modulus of elasticity for specimens of glass-fabric laminates tested under various conditions of temperature and heating* [a]—Continued.

Temperature of heating	Special conditions	Secant modulus of elasticity in flexure															
		Unsaturated polyester resin laminates								Acrylic laminate C		Silicone laminate B		Phenolic laminate H		Melamine laminate J	
		Laminate A		Laminate E		Laminate F		Laminate G									
		Mean	Range	Mean	Range	Mean	Range	Mean	Range	Mean	Range	Mean	Range	Mean	Range	Mean	Range
MODULUS OF ELASTICITY OF SPECIMENS AT A TEMPERATURE T AFTER 0.5 HR AT THE TEMPERATURE T																	
		0 to 5,000 lb/in.²		0 to 7,500 lb/in.²		0 to 5,000 lb/in.²		0 to 2,000 lb/in.²		0 to 1,000 lb/in.²		0 to 5,000 lb/in.²		0 to 15,000 lb/in.²		0 to 15,000 lb/in.²	
°C		10^6 lb/in.²	10^6 lb/in.²	10^6 lb/in.²	10^6 lb/in.²	10^6 lb/in.²	10^6 lb/in.²	10^6 lb/in.²	10^6 lb/in.²	10^6 lb/in.²	10^6 lb/in.²	10^6 lb/in.²	10^6 lb/in.²	10^6 lb/in.²	10^6 lb/in.²	10^6 lb/in.²	10^6 lb/in.²
150		1.48	1.24 to 1.66	2.50	2.34 to 2.59	2.84	2.74 to 2.99	0.86	0.63 to 1.07	0.29	0.26 to 0.32	1.39	1.31 to 1.48	2.44	2.30 to 2.54	2.33	2.19 to 2.42
		0 to 8,000 lb/in.²		0 to 15,000 lb/in.²		to 10,000 lb/in.²		0 to 4,000 lb/in.²		0 to 2,000 lb/in.²		0 to 10,000 lb/in.²		0 to 30,000 lb/in.²		0 to 30,000 lb/in.²	
150		1.27	1.04 to 1.40	2.44	2.32 to 2.52	2.46	2.15 to 2.68	0.80	0.61 to 0.97	0.26	0.25 to 0.29	1.26	1.19 to 1.33	2.40	2.27 to 2.50	2.05	1.88 to 2.16
		0 to 4,000 lb/in.²		0 to 7,500 lb/in.²		0 to 4,000 lb/in.²		0 to 2,500 lb/in.²						0 to 20,000 lb/in.²		0 to 15,000 lb/in.²	
200		1.23	1.09 to 1.37	1.72	1.62 to 1.81	1.88	1.69 to 2.35	0.84	0.63 to 1.32					2.28	1.87 to 3.07	2.02	1.91 to 2.10
		0 to 4,000 lb/in.²		0 to 5,000 lb/in.²		0 to 4,000 lb/in.²		0 to 2,500 lb/in.²				0 to 7,500 lb/in.²		0 to 15,000 lb/in.²		0 to 15,000 lb/in.²	
250	Asbestos-covered tray [b]	1.20	0.98 to 1.34	1.26	1.06 to 1.39	1.18	1.02 to 1.37	0.49	0.38 to 0.65			1.36	1.27 to 1.41	1.52	1.42 to 1.79	1.68	1.60 to 1.73
		1.07	0.84 to 1.32	1.27	1.19 to 1.39			0.66	0.55 to 0.86					1.77	1.52 to 1.90	1.73	1.68 to 1.79
		0 to 2,500 lb/in.²		0 to 4,000 lb/in.²		0 to 2,500 lb/in.²						0 to 7,500 lb/in.²		0 to 10,000 lb/in.²		0 to 15,000 lb/in.²	
300	do	0.78	0.74 to 0.81	0.80	0.74 to 0.89	[c] 1.13	[c] 0.56 to 1.39					[c] 1.35	[c] 1.30 to 1.44	1.69	1.27 to 2.11	1.60	1.56 to 1.65
		0.68	0.61 to 0.73	0.78	0.66 to 0.90	1.44	1.29 to 1.55					1.39	1.32 to 1.52	1.59	1.36 to 1.79	1.72	1.65 to 1.75
												0 to 7,500 lb/in.²		0 to 10,000 lb/in.²			
375	do											[c] 1.25	[c] 1.11 to 1.41	0.99	0.84 to 1.08	(e)	

MODULUS OF ELASTICITY OF SPECIMENS AT A TEMPERATURE T AFTER 30 HR AT THE TEMPERATURE T

MODULUS OF ELASTICITY OF SPECIMENS AT A TEMPERATURE T AFTER 200 HR AT THE TEMPERATURE T'[a]

	0 to 5,000 lb/in.²		0 to 10,000 lb/in.²		0 to 10,000 lb/in.²		0 to 2,000 lb/in.²		0 to 2,000 lb/in.²		0 to 5,000 lb/in.²		0 to 15,000 lb/in.²		0 to 10,000 lb/in.²	
150	2.02	1.87 to 2.19	2.72	2.64 to 2.84	3.13	2.96 to 3.32	0.82	0.64 to 0.96	0.32	0.16 to 0.50	1.54	1.42 to 1.65	2.46	2.34 to 2.62	2.41	2.28 to 2.49
	0 to 10,000 lb/in.²		0 to 20,000 lb/in.²		0 to 20,000 lb/in.²		0 to 4,000 lb/in.²		0 to 2,700 lb/in.²		0 to 10,000 lb/in.²		0 to 30,000 lb/in.²		0 to 20,000 lb/in.²	
150	1.97	1.83 to 2.10	2.65	2.58 to 2.74	2.93	2.72 to 3.24	0.78	0.56 to 0.95	0.30	0.13 to 0.48	1.51	1.35 to 1.63	2.37	2.20 to 2.60	2.23	2.11 to 2.35
	0 to 4,000 lb/in.²		0 to 15,000 lb/in.²		0 to 10,000 lb/in.²		0 to 2,500 lb/in.²						0 to 7,500 lb/in.²		0 to 15,000 lb/in.²	
200	1.03	0.97 to 1.08	2.02	1.93 to 2.15	2.83	2.76 to 2.93	0.44	0.40 to 0.47					1.64	1.47 to 1.75	1.93	1.87 to 1.96
	0 to 1,500 lb/in.²		0 to 5,000 lb/in.²		0 to 1,500 lb/in.²						0 to 7,500 lb/in.²				0 to 10,000 lb/in.²	
250	0.91	0.42 to 1.21	1.82	1.65 to 2.02	1.82	1.48 to 2.09					1.66	1.62 to 1.73	(e)		1.21	1.15 to 1.28
											0 to 7,500 lb/in.²				0 to 1,000 lb/in.²	
325[j]											1.61	1.50 to 1.76			[k]0.64	[k]0.52 to 0.75

[a] Specimens approximately ⅛ in. thick and 1 in. wide tested at 0.04 in./min relative head motion with a span of 2.0 in. Each value is the average for 5 specimens, unless otherwise noted. Specimens taken at random from the sheets, unless otherwise noted. The stress range for the secant modulus is shown above each set of values.

[b] Interpolated.

[c] Four specimens.

[d] Unless otherwise noted, all specimens that were heated for 200 hr were heated in open wide-mouthed bottles placed in a circulating-air oven.

[e] After removal from the oven, specimens kept over calcium chloride for 24 hr prior to testing.

[f] Specimens laid on asbestos board on oven shelf.

[g] The load-deflection records were too small to permit determination of the modulus.

[h] The normal tray is an aluminum tray. The asbestos-covered tray is the same aluminum tray covered with absestos paper about ⅛ in. thick. Unless otherwise noted, all tests at elevated temperature were made with the normal tray.

[i] Specimens not randomly selected but taken from at least 3 sheets.

[j] A muffle furnace controlled at 325°±10° C was used for conditioning these specimens.

[k] Two specimens.

IV. Results and Discussion

The flexural strength data for the various samples tested under different conditions of temperature and heating are shown in table 2. Some of the data in table 2 are shown graphically in figures 4 to 6; the data that are plotted are for normal conditioning and testing, except when the only tests made were with the tray covered with asbestos. The corresponding data for flexural secant modulus of elasticity are shown in table 3 and figures 7 to 9. The secant moduli selected for graphing are for a stress range from zero to one-half to two-thirds of the flexural strength; these secant moduli are expressed as percentages of the values for the controls for the corresponding stress range. The loss-of-weight data for the samples after heating for 200 hr at various temperatures are given in table 4. The precision of the data and other statistical points are discussed in the next section of this report.

In the detailed discussion of the results that follows, it must be noted that, except for the polyester laminates, only one sample of a given type laminate was tested. Hence only tentative

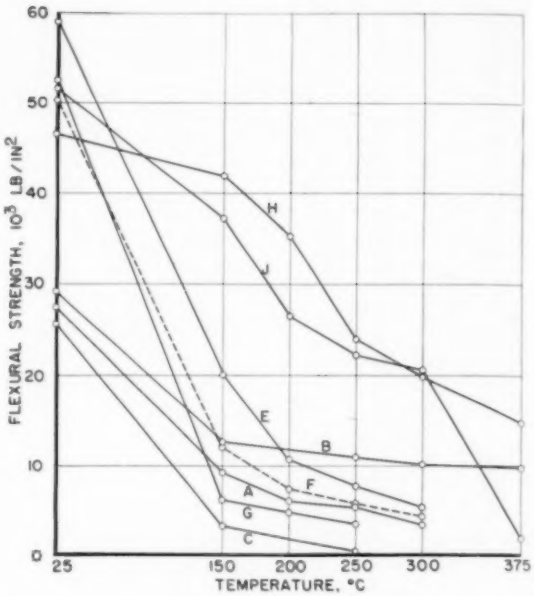

FIGURE 5. *Flexural strength of glass-fabric laminates at a temperature T after 0.5 hour of heating at T.*

A, E, F, G, Unsaturated polyester; *B,* silicone; *C,* acrylic addition; *H,* phenolic; *J,* melamine.

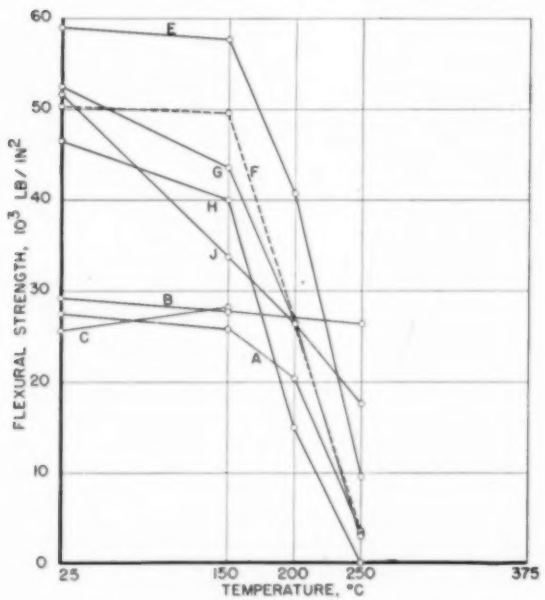

FIGURE 4. *Flexural strength of the laminates at 25° C after 200 hours of heating at various temperatures.*

A, E, F, G, Unsaturated polyester; *B,* silicone; *C,* acrylic addition; *H,* phenolic; *J,* melamine.

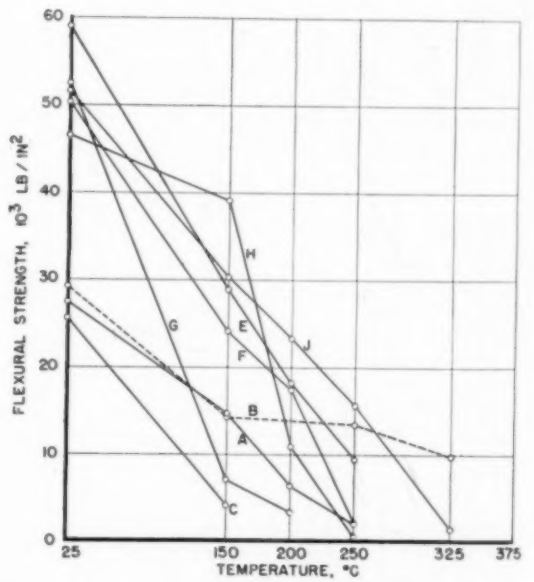

FIGURE 6. *Flexural strength of glass-fabric laminates at a temperature T after 200 hours of heating at T.*

A, E, F, G, Unsaturated polyester; *B,* silicone; *C,* acrylic addition; *H,* phenolic; *J,* melamine.

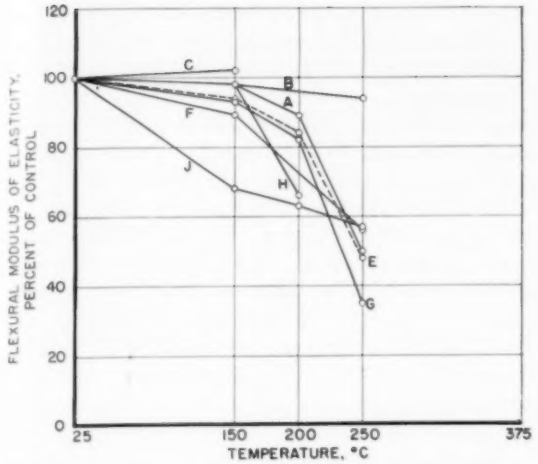

FIGURE 7. *Flexural secant modulus of elasticity of the laminates at 25° C after 200 hours at various temperatures.*

A, E, F, G, Unsaturated polyester; *B,* silicone; *C,* acrylic addition; *H,* phenolic; *J,* melamine.

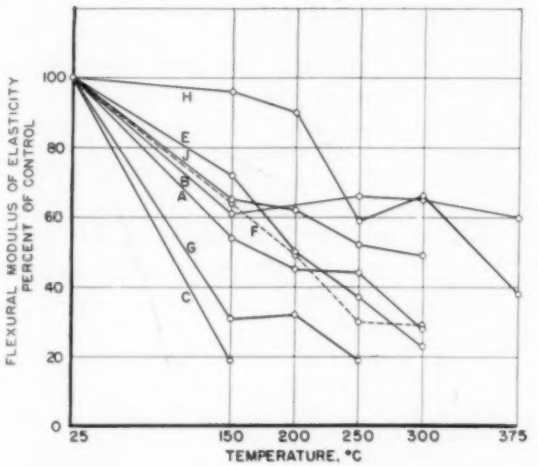

FIGURE 8. *Flexural secant modulus of elasticity of the laminates at a temperature T after 0.5 hour of heating at T.*

A, E, F, G, Unsaturated polyester; *B,* silicone; *C,* acrylic addition; *H,* phenolic; *J,* melamine.

inferences may be drawn regarding the behavior of the various types of materials.

1. Flexural Strength

The four polyester samples (figs. 4 to 6) show less than 20-percent loss in strength when tested at 25° C after 200 hr of heating at 150° C. When tested at 25° C after 200 hr of heating at temperatures above 150° C, the loss in strength increases rapidly, reaching about 90 percent at 250° C. These four polyester samples show losses in strength ranging from 50 to 90 percent when tested at 150° C after either 0.5 or 200 hr of

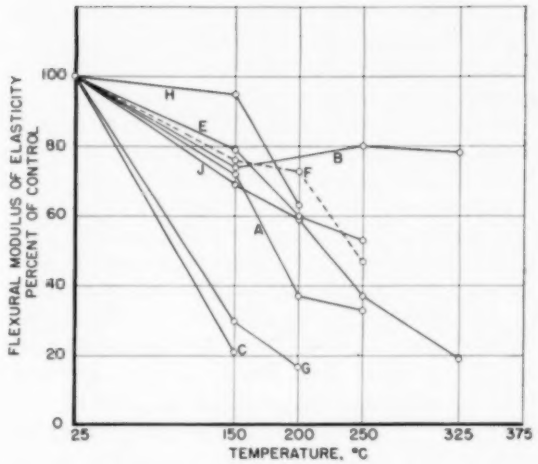

FIGURE 9. *Flexural secant modulus of elasticity of the laminates at a temperature T after 200 hours of heating at T.*

A, E, F, G, Unsaturated polyester; *B,* silicone, *C,* acrylic addition; *H,* phenolic; *J,* melamine.

TABLE 4. *Loss of weight and loss of resin by glass-fabric laminates after heating 200 hours at various temperatures* [a]

NBS sample designation	150° C		200° C		250° C		325° C	
	Weight loss	Resin loss [b]	Weight loss	Resin loss [b]	Weight loss	Resin loss [b]	Weight loss	Resin loss [b]
Unsaturated-polyester resin:	%	%	%	%	%	%	%	%
A	2.1	6.0	7.7	22.0	26.2	74.8	.....	.....
E	0.9	2.8	4.8	15.0	25.3	79.1	.....	.....
F	1.2	5.0	4.6	19.2	18.1	75.4	.....	.....
G	2.1	5.0	10.4	24.8	31.3	74.5	.....	.....
Acrylic addition resin:								
C	1.3	2.1	.....	.....	.....	.....	.....	.....
Silicone resin:								
B	0.13	0.33	.....	.....	0.51	1.3	2.1	5.4
Phenolic resin:								
H	2.1	4.8	8.9	20.2	34.7	79.0	.....	.....
Melamine resin:								
J	3.5	7.6	4.9	10.7	8.4	18.3	.....	.....

[a] The initial weights were determined after at least 7 days' conditioning at 25° C and 50% relative humidity; the final weights were obtained after the specimens had been reconditioned 7 days at 25° C and 50% relative humidity following the 200 hr of heating. Each value is the average for 5 specimens.

[b] Calculated on basis of NBS values for resin content except for laminate *B*, the assumption is made that total weight loss is resin.

heating at 150° C. For similar treatment at 250° C the loss in strength is at least 80 percent, even for samples tested after only 0.5 hr of heating.

The acrylic laminate *C*, when tested at 150° C after either 0.5 or 200 hr of heating, retained only about 15 percent of its initial strength.

The flexural strength at 25° C of silicone laminate *B* was reduced only 10 percent after heating 200 hr at 250° C; this was the least change observed for any sample for this test condition. In tests at elevated temperatures, after heating the samples for either 0.5 or 200 hr, the flexural strength dropped considerably between 25° and 150° C. The flexural strength at 150° C was about 13,000 lb/in.^{2} compared to a value of 29,000 lb/in.^{2} for the controls. Above 150° C the strength diminished very slowly with increase in temperature up to 250° C for the 200-hr and up to 375° C for the 0.5-hr heating period, respectively. It is of interest to compare the results obtained in this laboratory with data obtained by the New York Naval Shipyard [9] on two samples of 0.5-in. thick glass-fabric silicone laminate from two sources. Some of these results, as well as data for sample *B*, are shown in table 5.

TABLE 5. *Comparison of results for sample* B *with other flexural data on silicone laminates*

Temperature of conditioning and test	Flexural strength at *T* after heating at *T*					
	Sample *I* [9]		Sample *II* [9]		Sample *B*	
	Heated 1 hr	Heated 192 hr	Heated 1 hr	Heated 192 hr	Heated 0.5 hr	Heated 200 hr
°C	10^3 lb/in.^{2}	10^3 lb/in.^{2}	10^3 lb/in.^{2}	10^3 lb/in.^{2}	10^3 lb/in.^{2}	10^3 lb/in.^{2}
150	7.2	17.8	9.8	12.0	12.6	14.3
250	3.6	12.8	5.0	4.2	10.9	13.4
Control values	29.9		20.0		29.2	

Sample *I* was reported to be softened at 250° C when heated only a short time at that temperature; in view of the improvement on further heating, this behavior was believed to be caused by further cure [9]. To test this idea they report [9] that specimens of sample *I* were heated for 72 hr at 250° C, reconditioned for 72 hr at 25° C and 50-percent relative humidity, and then tested at 250° C after 1 to 4 hr at 250° C; flexural strengths of 11,000 lb/in.^{2} were obtained. These results give some indication of the variability in behavior of different silicone laminates and also show the possibility with such laminates of having an undercured material.

The sample of phenolic laminate *H* was outstanding in retention of flexural strength at elevated temperatures when heated only 0.5 hr at the test temperature. For example, the flexural strength at 375° C for this test condition was 15,000 lb/in.^{2} compared to 46,000 lb/in.^{2} for the control (fig. 5). The same sample, however, was seriously degraded by prolonged heating at 250° C; after such treatment it exhibited a flexural strength much less than 1,000 lb/in.^{2} when tested either at 250° or 25° C.

The melamine laminate *J* shows a nearly steady decline in strength from 25° to 250° C or more for the three heating and testing conditions. The flexural strength is reduced to about two-thirds, one-half, and one-third for heating at 150°, 200°, and 250° C, respectively. At a given temperature *T*, the strength at *T* after 0.5 hr of heating is slightly greater than that for tests at 25° C after 200 hr of heating, and the latter strength is slightly greater than that at a temperature *T* after 200 hr of heating. These flexural strength values were compared with data obtained by the New York Naval Shipyard [9]. The latter laboratory made tests similar to those described in this report on a 0.5-in.-thick melamine laminate. The general trend of the strength-temperature data given in [9] is similar to that shown in figures 4 to 6 for sample *J*.

2. Flexural Modulus of Elasticity

For a given sample the trend shown by the flexural secant modulus of elasticity versus temperature graph is quite similar to the plot of flexural strength versus temperature for the same condition of heating and testing. However, for each laminate the percentage loss in flexural modulus of elasticity for a given test condition is always less than the loss in flexural strength for that test condition.[3]

3. Correlation Between Changes in Flexural Strength and Modulus of Elasticity

In figure 10 the flexural strength in percentage of control is plotted against the flexural modulus of elasticity in percentage of control for all the lami-

[3] There were exceptions to this statement when the loss in the flexural property was 5% or less. Such losses are not considered significant.

nates except *C*. Data for all conditions in tables 2 and 3 were used, except that the values for "Special conditions" were not plotted unless no other data at a given temperature were available. The modulus of elasticity data for the lowest stress range was used in the case of tests at 150° C. It is evident that a correlation exists between these two quantities; furthermore, it appears that the correlation equation is probably different for the polyester laminates as compared to the melamine laminate *J*. A detailed analysis of the correlation was not made, as only in the case of the polyester laminates was there more than one sample of a given type of laminate.

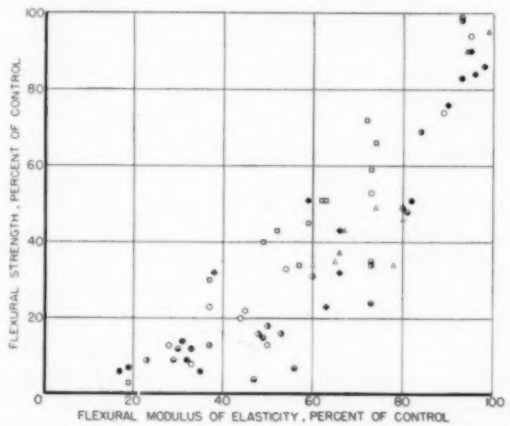

FIGURE 10. *Correlation between flexural strength and flexural secant modulus of elasticity.*

Data taken from tables 2 and 3. Sample A, ○; E, ◑; F, ◒; G, ●; B, △; J, □; H, ◆.

4. Relative Heat Resistance of the Laminates

To give a concise comparison of the laminates as regards their retention of flexural properties at elevated temperatures, a table was prepared in the following manner: For each sample the temperatures in figures 4 to 6 were noted for which the flexural strength was 30 percent or more of the flexural strength for the control for all three conditions of heating and testing. The same procedure was followed for the corresponding secant modulus of elasticity values, except that the percentage was 50 instead of 30. These temperature limits are shown in table 6. Since it was often necessary to interpolate the stress range as well as the modulus of elasticity, the temperatures given in table 6 for the modulus data are less accurate

TABLE 6. *Relative heat resistance of glass-fabric laminates, based on flexural properties*

NBS sample designation	Temperature T at which flexural strength is at least 30% of control value for the three types of tests [a]	Temperature T at which flexural secant modulus of elasticity is at least 50% of control value for the three types of test [a]	
		Temperature	Stress range
Unsaturated-polyester resin:	° C	° C	*lb/in.²*
A	150	150	0 to 6,000.
E	150	200	0 to 7,500.
F	140 (estimated)	200	0 to 4,000.
G	130 (estimated)	Less than 150	0 to 4,000.
Acrylic addition resin:			
C	Much less than 150	Much less than 150	0 to 5,000.
Silicone resin:			
B	325	325 (for 65%, estimated).	0 to 7,500.
Phenolic resin:			
H	200	220 (estimated)	0 to 5,000.
Melamine resin:			
J	250	220 (estimated)	0 to 10,000.

[a] Tests at 25° C after 200 hr of heating at temperature T, and tests at temperature T after 0.5 or 200 hr of conditioning at temperature T.

than the temperatures for the flexural strength. It must be emphasized in addition, that for the modulus of elasticity data, temperatures different from those given in table 6 would apply for other stress ranges; when the stress-strain diagram is nearly linear for the ranges considered, the effect of differing stress range is slight.

It is of interest to compare the values in table 6 with data obtained by Sieffert and Schoenborn [10]. The latter authors determined the weight loss as a function of time for a number of laminates at various temperatures; from these data curves were plotted of weight loss versus temperature. It was found that for each material the weight loss as a function of temperature began to increase rapidly beyond a certain temperature. By using an arbitrary criterion, a "critical thermal instability temperature" was determined from the plotted data. The values Sieffert and Schoenborn reported for several laminates are shown in table 7.

It is evident that there is close agreement between the critical thermal instability temperature and the temperatures given in table 5 for retention of 30 percent of original flexural strength.

5. Effect of Speed of Heated Air on Changes in Flexural Properties

The data in tables 2 and 3 for tests at 25° C after heating the specimens at 200° C either on the oven shelf or in open bottles were examined

TABLE 7. *Critical thermal instability temperature and resin loss data reported by Sieffert and Schoenborn [10] for glass-fabric laminates*

Glass-fabric laminate	Resin content	Critical thermal instability temperature (M=4,72-hr data)	Temperature for 5% resin loss (72 hr)
	Percent	° *C*	° *C*
Polyester	31	140	140
Silicone *A*	32	350	375
Silicone *B*	40	355	250
Low-pressure phenolic	28	210	220
Melamine-formaldehyde A	40	235	115
Melamine-formaldehyde B	45	240	100

statistically (see section V). It was found that both the flexural strengths and flexural moduli of elasticity for the polyester laminates and the phenolic laminate were significantly lower for the case of heating on the oven shelf, i. e., in rapidly moving air, as compared to heating in the open bottles. However, for the melamine laminate *J* the differences were not significant.

These results indicate that information on the effect of prolonged heating on the glass-fabric laminates under different atmospheric conditions is needed. The degradation of the resin may depend on the rate of removal of degradation products as well as the rate at which heated air containing oxygen, an important agent for some degradation reactions, is swept over the surface of the material. It follows that the use of data of the type presented in this report on the properties of laminates after prolonged heating should be used for design purposes with caution, since in practice the conditions of heating may differ widely from those that apply to the data given here. Likewise, interlaboratory comparisons of a given laminate may give discordant results if the heating conditions are not duplicated.

6. Loss of Weight on Heating

After 200 hr of heating at only 150° C, all the samples except the silicone exhibited losses in resin of 2 to 8 percent of the initial amount, with the melamine laminate showing the greatest loss. As the temperature of heating was raised, the loss in amount of resin increased very rapidly for all the polyester laminates and the one phenolic laminate. For these samples the resin loss is roughly four-fold at 200° C and twelve- to thirty-fold at 250° C, compared to the losses at 150° C. In contrast to this behavior the melamine laminate showed much less rapid increases in resin loss (see table 4).

V. Statistical Analysis

1. Precision of Results

The standard deviation was determined for the data in tables 2 and 3 for tests at various conditions. For a given sample it was observed that the standard deviation tended to be proportional to the mean value. For this reason, further analysis was made with the coefficient of variation instead of the standard deviation. The coefficient of variation is defined as 100 times the ratio of the standard deviation to the mean value.

The coefficient of variation was not reported for each flexural strength value in table 2 or each modulus of elasticity value in table 3 because such statistics, based on only five observations, are subject to wide variability. It was decided to analyze the individual coefficient of variation with respect to its variation from sample to sample and between the different temperatures. This was done to determine in what manner these data could best be combined for more reliable estimates of precision. The analyses are discussed in the following paragraphs.

(a) Flexural Strength

The coefficient of variation (C_v) was determined for all the values in table 2. A statistical analysis of some of these data indicates some variation of the value of C_v between samples. No consistent trend for the effect of conditioning or test temperature on the value of C_v for the samples was noted. Therefore, the estimates of C_v within each sample were pooled with the following results:

Laminate	C_v
Unsaturated polyester:	*Percent*
A	6.6
E	5.1
F	7.3
G	8.4
Acrylic addition:	
C	8.8
Silicone:	
B	5.2
Phenolic:	
H	10
Melamine:	
J	2.9

In a few instances, usually for the highest testing or conditioning temperature and when the flexural strength was a small fraction of the initial value, a very large value of C_v was obtained; such values were omitted in obtaining the above estimates of C_v.

(b) Flexural Modulus of Elasticity

The coefficient of variation was determined for the modulus values in table 3. A statistical analysis was carried out for the tests made either at 25° C or at a temperature T after 200 hr of heating at T. It was found that (1) the effect of conditioning temperature on C_v varies significantly from sample to sample; (2) C_v cannot be assumed to be the same for all samples; and (3) the effect of testing temperature, i. e., 25° C compared to T, on C_v varies significantly from sample to sample. The above effects do not seem to be important *except* the sample-to-sample variability. It was therefore decided to combine the estimates of C_v for the various samples. The estimated values of C_v for the modulus of elasticity are:

Laminate	C_v
Unsaturated polyester:	*Percent*
A	7.5
E	5.1
F	8.8
G	14
Acrylic addition:	
C	7
Silicone:	
B	4.5
Phenolic:	
H	10
Melamine:	
J	3.0

In a few instances, usually for the highest testing or conditioning temperature and when the modulus of elasticity was a small fraction of the initial value, a very large value of C_v was obtained; such values were omitted in obtaining the above estimates of C_v.

2. Thermal Shock in Tests After 0.5 Hour of Heating

A statistical analysis was made of the flexural data for the tests after 0.5 hr of heating in which duplicate sets of specimens were tested, one set with and one set without asbestos paper on the metal specimen tray. All the samples do not behave alike with respect to differences in flexural strength or modulus of elasticity for the two tray conditions. Although in some cases there appears to be a significant effect, the data as a whole do not support the assumption that the thermal shock is serious.

3. Effect of Heating in Still Air Compared to Heating in Rapidly Moving Air

A statistical analysis was made of the flexural data for the tests at 25° C after 200 hr of heating at 200° C with the specimens exposed (1) in open bottles, and (2) on the oven shelf. It was found that flexural strength and flexural modulus of elasticity were similarly affected for specimens contained in open bottles compared to those placed directly on the oven shelf during the heating period. The data for each sample were tested separately. Samples *A*, *G*, and *H* all show significantly greater losses in flexural strength and modulus of elasticity for shelf heating compared to bottle heating. For sample *E* the effect was significant for flexural strength but not for modulus of elasticity. For sample *J* no significant effect was noted.

VI. Conclusions

The silicone laminate is superior to the other laminates tested in retention of flexural properties at temperatures of 250° to 300° C. When tested at about 325° C after either 0.5 or 200 hr of heating at that temperature, this laminate retained at least 30 percent of its initial flexural strength and over 50 percent of its initial flexural modulus of elasticity.

The phenolic laminate showed good retention of its flexural properties when tested at elevated temperatures after heating for 0.5 hr at the test temperature. When tested in this way at 375° C, the flexural strength was 15,000 lb/in.^{2}, and the modulus of elasticity was 1.0×10^6 lb/in.^{2}, values roughly one-third of the corresponding values for the controls. The behavior of the phenolic laminate after prolonged heating was much less satisfactory; at 25° or 250° C after 200 hr of heating at 250° C the flexural strength was much less than 1,000 lb/in.^{2}.

The melamine laminate, although much inferior to the phenolic laminate when tested at a temperature of 375° C after 0.5 hr of heating, was superior to the phenolic in retention of flexural strength after 200 hr of heating at 250° C.

The four polyester laminates lost at least 80 percent of their flexural strengths when tested at 250° C after either 0.5 or 200 hr of heating.

The acrylic addition laminate lost at least 80 percent of its flexural strength when tested at 150° C after either 0.5 or 200 hr of heating.

For each laminate and each test condition, loss in flexural modulus of elasticity correlates with loss in flexural strength; the former loss is less than the latter.

The loss in flexural properties during prolonged heating may depend on the method of exposing the specimens in the oven. For specimens of the polyester and phenolic laminates, heating in a circulating-air oven in open bottles caused significantly less loss in flexural properties than did heating on the shelves of the oven.

These conclusions, except for the polyester laminates, are based on data for only one sample of each type of glass-fabric laminate and hence can be considered only tentatively as being representative of the various types of material.

The courtesy of the American Cyanamid Co., Dow Corning Corp., E. I. du Pont de Nemours & Co., Formica Co., Monsanto Chemical Co., Plaskon Division of the Libbey-Owens-Ford Glass Co., and the Resinous Products Division of the Rohm & Haas Co. in furnishing materials for use in this investigation is gratefully acknowledged. The cooperation of the following members of the staff of the National Bureau of Standards also is appreciated: M. N. Geib, who assisted in the design of the apparatus; H. W. Bailey and W. O. Bottamiller, who constructed the apparatus; and J. Mandel, who made the statistical analysis.

VII. References

[1] P. M. Field, Basic physical properties of laminates, Modern Plastics **20,** 91 (Aug. 1943).

[2] H. R. Meyer and E. C. O. Erickson, Factors affecting the strength of papreg. Some strength properties at elevated and subnormal temperatures. Forest Products Laboratory Report No. 1521 (Jan. 1945).

[3] W. C. Renwick, Properties of plastic laminates, Part VI. Naval Air Exp. Sta. Report TED NAM 25217.0 (June 3, 1944).

[4] D. A. Shinn, Impact data for plastic materials at various temperatures, Air Corps Tech. Report No. 5012 (Aug. 9, 1943); Modern Plastics **22,** 145 (July 1945).

[5] E. O. Hausmann, A. E. Parkinson, and G. H. Mains, Heat resistance of laminated plastics, Modern Plastics **22,** 151 (Nov. 1944).

[6] J. J. Lamb, I. Albrecht, and B. M. Axilrod, Impact strength and flexural properties of laminated plastics at high and low temperatures, NACA Tech. Note No. 1054 (1946).

[7] J. J. Lamb, I. Albrecht, and B. M. Axilrod, Tensile and compressive properties of laminated plastics at high and low temperatures, NACA Tech. Note No. 1550 (1948).

[8] P. Norelli and W. H. Gard, Temperature effect on strength of laminates. Ind. Eng. Chem. **37,** 580 (June 1945).

[9] Investigation of the effects of high and low temperature conditioning on properties of laminated thermosetting plastic materials. Report No. 4860–A, Special Summary; Material Laboratory, New York Naval Shipyard (Aug. 29, 1949).

[10] L. E. Sieffert and E. M. Schoenborn, Critical thermal instability temperature of laminated plastic electrical insulation. Navy Dept., Bureau of Ships; manuscript submitted to Ind. Eng. Chem. for publication.

Washington, February 23, 1950.

U. S. Department of Commerce
National Bureau of Standards

Research Paper RP2115
Volume 45, July 1950

Part of the Journal of Research of the National Bureau of Standards

Attenuation of Oscillatory Pressures in Instrument Lines[1]

By Arthur S. Iberall

A theoretical investigation has been made of the attenuation and lag of an oscillatory pressure variation applied to one end of a tube, when the other end is connected to a pressure-sensitive element.

An elementary theory based on incompressible viscous-fluid flow is first developed. The elementary solution is then modified to take into account compressibility; finite pressure amplitudes; appreciable fluid acceleration; and finite length of tubing (end effects). Account is taken of heat transfer into the tube.

The complete theory is derived in an appendix. The results are summarized in eight graphs in a form convenient for use in computing the lag and attenuation of a sinusoidal oscillation in a transmission tube.

1. Introduction

In many industrial processes, it is necessary to know or to utilize the pressure at one or more points in a fluid conduit. It is not always possible to connect an instrument directly into the conduit at those points. Instead, recourse must be had to remote indication or control. In the case that a fluid is used for transmitting the pressure, it is often of interest to the designer or user of such systems to know their response to variations in pressure. At the present time, the only solution easily available to the engineer is generally based on an elementary theory that considers the system as equivalent to an R–C electrical network. (See, for example, NACA Technical Note 593, Pressure drop in tubing in aircraft instrument installations, by W. A. Wildhack.) The main defect of the theory is that it does not provide criteria for the limits of its applicability.

In the present paper, a relatively complete treatment is given for the transmission of oscillatory pressures in tubing. Primary consideration is given to simplifying the design of high-quality transmission systems for relatively low frequencies.

The elementary solution is derived and then extended to apply for oscillatory pressures that are an appreciable fraction of the absolute mean pressure, for appreciable frequencies of oscillation, and for tubing short enough to require end corrections. The effect of heat transfer in modifying the oscillatory response of the tube is also discussed.

The chief utility of knowing these corrections is that it permits the designer to choose the size of tubing for specific applications with greater confidence than can otherwise be done.

In the next section, the elementary theory of transmission lags is developed, and the corrections are discussed. The complete theory is presented in graphical form for the convenience of the designer. A number of examples of the use of the design charts are also given. This section is then followed by a mathematical appendix in which the more exact results are derived. All mathematical symbols used in this paper are defined in section II and also when they are first used.

II. List of Mathematical Symbols

A=tube area.
C=velocity of sound.
D=inside diameter of tube.
E=elastic modulus of tube.
F=correction functions.
K=thermal conductivity of fluid.
L=tube length.
M=mass flow.
N=dimensionless parameter of fluid regime.
Q=volumetric flow.

[1] This work was supported by the Office of Naval Research under a project on "Basic Instrumentation for Scientific Research."

R=a volume ratio.
R_e=Reynolds number.
T=absolute temperature.
V=instrument volume.
b=compressibility factor for liquid.
c=any arbitrary constant.
c_p=specific heat of fluid.
f=any arbitrary function.
g=a Bessel function argument.
h=a Bessel function argument.
k=compressibility of a liquid.
l=entrance length.
m=exponent of "polytropic" expansion in instrument volume.
n=exponent of "polytropic" expansion in tube.
p=pressure.
s=tube wall thickness.
t=time.
u=axial velocity.
x=axial distance along tube.
y=a dimensionless axial distance variable.
z=dimensionless parameter of fluid regime.
γ=ratio of specific heats.
δ=phase angle.
η=density ratio.
λ=time constant.
μ=fluid viscosity.
ν=kinematic viscosity.
ξ=fractional pressure excess.
ρ=fluid density.
σ=Prandtl number.
ϕ=velocity potential.
χ=attenuation factor.
ψ=attenuation parameter.
ω=angular frequency.

III. Elementary Theory

Figure 1 is a schematic drawing of the system that will be discussed throughout the paper. A tube transmits fluid pressure from a conduit to a pressure-sensitive instrument. The conduit applies an oscillatory (sinusoidal) pressure to the entrance of the transmission tube. The tube, which transmits the pressure, is characterized by a constant cross-sectional area and its length. The pressure-sensitive instrument, which receives the pressure, is characterized by its enclosed volume. It is assumed that if the walls enclosing the instrument volume are flexible (either elastic or piston-like), the enclosed volume can be replaced by a larger equivalent rigid volume that will store the same mass of fluid per unit pressure change. It is further assumed that the pressure-sensitive instrument will be so chosen that its indication is independent of the frequency of expected pressure oscillations.

In deriving the elementary theory, it is assumed that Poiseuille's law of viscous resistance holds at each point in the tube; that the fluid is incompressible in the tube; that the sinusoidal pressure oscillations at the beginning of the tube are of small amplitude compared to the mean absolute pressure; and that, if the fluid is a gas, it expands and contracts isothermally in the instrument volume.

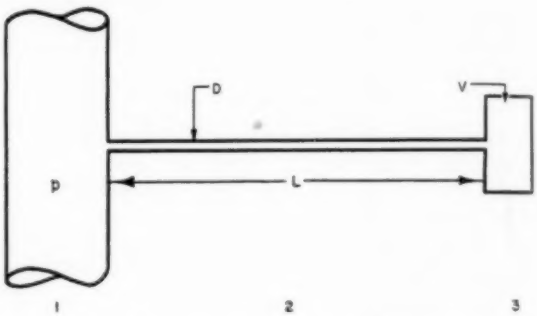

FIGURE 1. *Schematic diagram of a fluid transmission system (1-conduit, 2-transmission tube, 3-pressure instrument).*

$p=p_0+\Delta p \cos \omega t$.

The same assumptions applied to an incompressible fluid (e.g., a liquid) lead to the conclusion that there is no loss in amplitude or lag in a liquid-filled system as a liquid would not expand or contract in the instrument volume.

We may write

$$\frac{\partial p}{\partial x}=-\frac{128}{\pi}\frac{\mu_0}{D^4}Q \tag{1}$$

for Poiseuille's law, and

$$\frac{\partial M}{\partial x}=-A\frac{\partial \rho}{\partial t} \tag{2}$$

for the equation of continuity. Here

p=instantaneous pressure at any point in the tube
x=distance along the tube measured from its entrance

μ_0 = mean fluid viscosity
D = tube diameter
Q = volumetric flow at any point in the tube
ρ = instantaneous density at any point in the tube
M = mass flow at any point in the tube
A = cross-sectional area of the tube
t = time.

We infer from the equation of continuity and the assumption that the fluid is incompressible in the tube (i. e., $\partial\rho/\partial t=0$) that the mass flow, and therefore the volumetric flow, does not vary along the tube, but at most varies only with time (the fluid motion is piston-like).

By differentiating eq 1, we then obtain

$$\frac{\partial^2 p}{\partial x^2}=0 \tag{3}$$

along the tube.

Our boundary conditions are that at $x=0$

$$p=p_0+\Delta p e^{j\omega t}, \tag{4}$$

a sinusoidal pressure variation about the mean pressure, and that at $x=L$

$$\left.\begin{aligned} Q&=\frac{V}{p_0}\frac{\partial p}{\partial t}\\ \frac{\partial p}{\partial x}&=-\frac{128}{\pi}\frac{\mu_0}{D^4}Q \end{aligned}\right\}. \tag{5}$$

The first line of eq 5 expresses the rate at which a compressible fluid entering a rigid volume builds up pressure, whereas the second line of eq 5 states that the flow into the volume is limited by the pressure gradient at the end of the tube. Here

p_0 = mean pressure at the entrance
Δp = amplitude of the pressure oscillation at the conduit
V = instrument volume
ω = angular frequency of the pressure oscillation
L = length of the tube.

It is convenient to introduce a new variable ξ, the fractional pressure excess, defined as

$$\xi=\frac{p-p_0}{p_0}, \tag{6}$$

so that eq 3, 4, and 5 become, respectively,

$$\frac{\partial^2\xi}{\partial x^2}=0 \tag{7}$$

at $x=0$

$$\xi=\xi_0 e^{j\omega t}, \tag{8}$$

and at $x=L$,

$$\left.\begin{aligned} \frac{\partial\xi}{\partial x}&=-\frac{128}{\pi}\frac{\mu_0}{p_0}\frac{V}{D^4}\frac{\partial\xi}{\partial t}\\ &=-\frac{\lambda_0}{L}\frac{\partial\xi}{\partial t} \end{aligned}\right\}. \tag{9}$$

where

$$\left.\begin{aligned} \lambda_0&=\frac{128}{\pi}\frac{\mu_0}{p_0}\frac{L}{D^4}V\\ &=32\frac{\mu_0}{p_0}\left(\frac{L}{D}\right)^2\frac{V}{AL} \end{aligned}\right\}. \tag{10}$$

Here

ξ = fractional pressure excess
ξ_0 = amplitude of the fractional pressure excess at the origin ($=\Delta p/p_0$)
λ_0 = a time constant of the system.

It is of further convenience to separate the pressure excess into a part that varies with x and one that varies with t.

Let

$$\xi=\tilde{\xi}e^{j\omega t}, \tag{11}$$

where $\tilde{\xi}$ is the maximum amplitude of the pressure excess at any point of the tube.

Our equations then become

$$\frac{d^2\tilde{\xi}}{dx^2}=0 \tag{12}$$

at $x=0$,

$$\tilde{\xi}=\xi_0, \tag{13}$$

and at $x=L$

$$\frac{d\tilde{\xi}}{dx}=-\frac{\lambda_0\omega}{L}j\tilde{\xi}. \tag{14}$$

The solution of eq 12, which satisfies eq 13 and 14, is

$$\tilde{\xi}=\xi_0 \frac{1+\lambda_0\omega\left(1-\frac{x}{L}\right)j}{1+\lambda_0\omega j}. \tag{15}$$

The ratio of the amplitude of the pressure excess at the end of the tube to that at the beginning of the tube is then given by

$$\left.\begin{aligned}\frac{\tilde{\xi}_L}{\xi_0}&=\frac{1}{1+\lambda_0\omega j}\\ &=\frac{1}{1+\chi_0 j}\end{aligned}\right\} \tag{16}$$

where

$$\chi_0=\lambda_0\omega. \tag{17}$$

Here

$\tilde{\xi}_L$ = maximum amplitude of the pressure excess at the instrument volume

χ_0 = an attenuation factor.

The real part of eq 16 is the attenuation in amplitude of the pressure excess, whereas the imaginary part is the phase lag, or

$$\left.\begin{aligned}\left|\frac{\tilde{\xi}_L}{\xi_0}\right|&=\frac{1}{[1+\chi_0^2]^{\frac{1}{2}}}\\ \tan\delta_0&=\chi_0,\end{aligned}\right\} \tag{18}$$

where δ_0 is the lagging phase angle.

We will regard eq 18 as the elementary solution of our problem. It indicates that a transmission system is characterized by a time constant λ_0, which can be computed from a knowledge of the dimensions of the tube, the internal volume of the end device, and the average conditions of the gas in the tube; and an attenuation factor χ_0, for each angular frequency, from which one can compute the attenuation and phase lag in a tube. The tube dimensions and the instrument volume furnish the analog to the resistance and capacitance of an electrical network.

In principle, although difficult in practice, from a knowledge of the response to a sine wave, one can obtain the response to square waves, step function, etc., by Fourier analysis.

IV. Discussion of Corrections

The assumptions made in the elementary theory are restrictive, and in the appendix we shall modify them, one at a time, until finally we arrive at a complete solution that accurately takes into account all first-order phenomena, and partially takes into account second-order phenomena. Complete results are presented in convenient graphical form in figures 2 to 9.

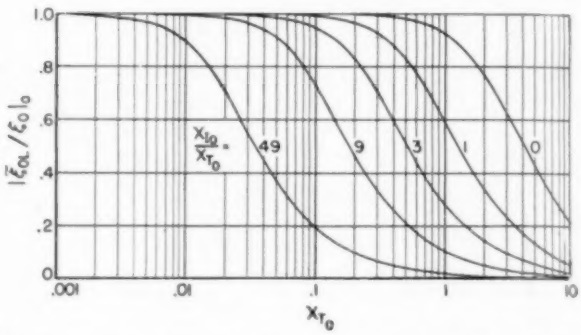

FIGURE 2. *Amplitude ratio of the fundamental $|\tilde{\xi}_{0L}/\xi_0|_0$ in a volume terminated tube as a function of a parameter proportional to frequency (χ_{T_0}) for various ratios of instrument volume to tube volume (χ_{I_0}/χ_{T_0}) with large damping ($z\leq 1$).*

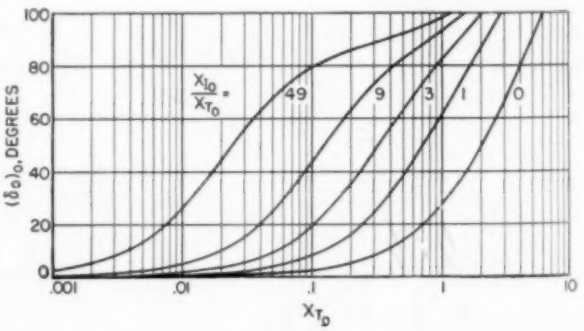

FIGURE 3. *Phase lag of the fundamental $(\delta_0)_0$ in a volume terminated tube as a function of a parameter proportional to frequency (χ_{T_0}) for various ratios of instrument volume to tube volume ($\chi_{I_0/\chi_{T_0}}$) with large damping ($z\leq 1$).*

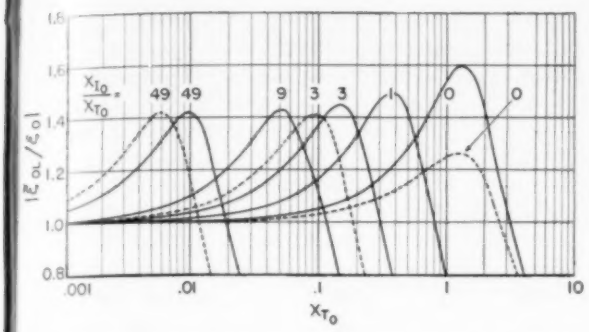

FIGURE 4. *Amplitude ratio of the fundamental* $|\bar{\xi}_{OL}/\xi_0|$ *in a volume terminated tube as a function of a parameter proportional to frequency* (χ_{T0}) *for various ratios of instrument volume to tube volume* (χ_{I0}/χ_{T0}) *and for two values of specific heat ratio* (γ) *with intermediate damping* ($z=6.25$).

———, $\gamma=1$; — — —, $\gamma=2$.

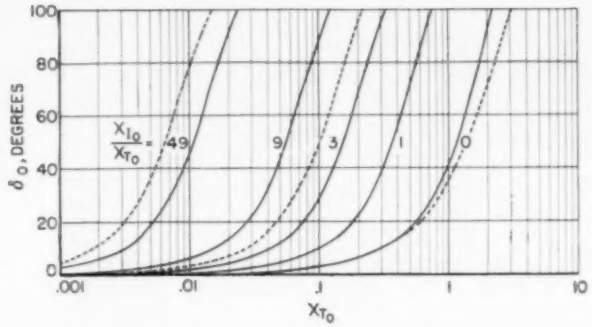

FIGURE 5. *Phase lag of the fundamental* (δ_0) *in a volume terminated tube as a function of a parameter proportional to frequency* (χ_{T0}) *for various ratios of instrument volume to tube volume* (χ_{I0}/χ_{T0}) *and for two values of specific heat ratio* (γ) *with intermediate damping* ($z=6.25$).

———, $\gamma=1$; — — —, $\gamma=2$.

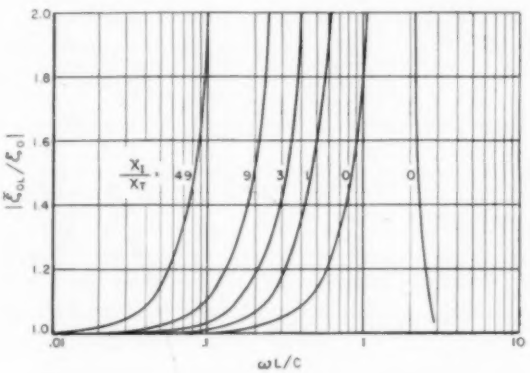

FIGURE 6. *Amplitude ratio of the fundamental* $|\bar{\xi}_{OL}/\xi_0|$ *in a volume terminated tube as a function of a parameter proportional to frequency* ($\omega L/C$) *for various ratios of instrument volume to tube volume* (χ_I/χ_T) *with little damping* ($z\geq 100$).

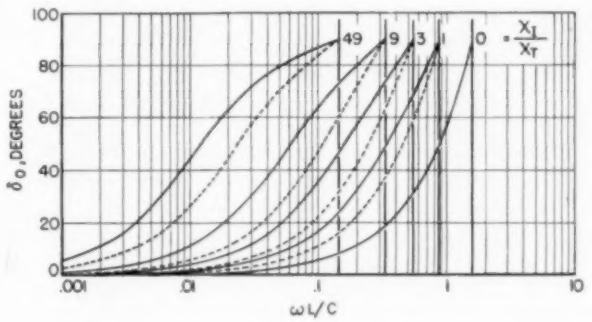

FIGURE 7. *Phase lag of the fundamental* (δ_0) *in a volume terminated tube as a function of a parameter proportional to frequency* ($\omega L/C$) *for various ratios of instrument volume to tube volume* (χ_I/χ_T) *indicating the difference between no damping* ($[\gamma\chi_{T0}/16]^{1/2}=0$) *and small damping* ($[\gamma\chi_{T0}/16]^{1/2}=1$) *for two values of specific heat ratio* (γ) *with small damping* ($z\geq 100$).

———, $\gamma=1$; — — —, $\gamma=2$. For curved lines $\sqrt{\frac{\gamma\chi_{T0}}{16}}=1$; for solid straight lines $\sqrt{\frac{\gamma\chi_{T0}}{16}}=0$.

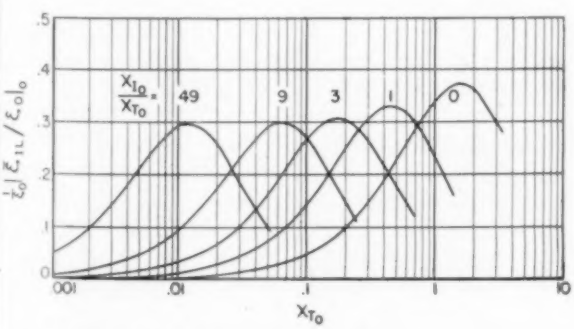

FIGURE 8. *Relative amplitude of the double harmonic distortion* ($\frac{1}{\xi_0}|\bar{\xi}_{1L}/\xi_{0L}|_0$) *in a volume terminated tube as a function of a parameter proportional to frequency* (χ_{T0}) *for various ratios of instrument volume to tube volume* (χ_{I0}/χ_{T0}) *with large damping* ($z\leq 1$).

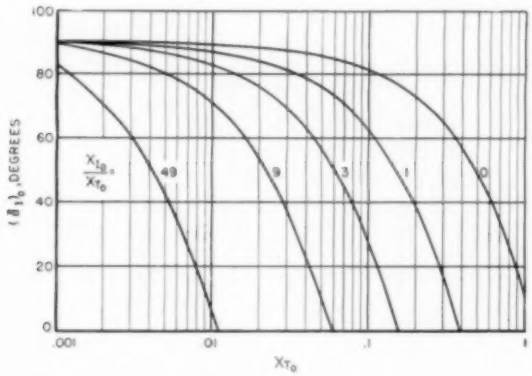

FIGURE 9. *Phase lead (as measured on the fundamental time scale) of the double harmonic distortion $(\delta_1)_0$ in a volume terminated tube as a function of a parameter proportional to frequency (χ_{T_0}) for various ratios of instrument volume to tube volume (χ_{I_0}/χ_{T_0}) with large damping $(z \leq 1)$.*

The factors that must be taken into account are:

1. *Compressible flow in the tube.* The effect of fluid compressibility is to introduce a time constant and corresponding attenuation factor (λ_T, χ_T) depending on the tube volume in addition to the ones depending on the instrument volume. (The time constant and attenuation factor depending on the instrument volume will be referred to as λ_I and χ_I henceforth instead of λ_0 and χ_0). In terms of the electrical analog, the tube volume represents a distributed capacitance in addition to the equivalent capacitance of the instrument volume.

2. *Finite pressure excess.* The effect of the application of a finite pressure excess to a compressible fluid in a transmission tube is to introduce harmonic distortion and to modify the mean pressure. However, the attenuation of the fundamental is essentially independent of the magnitude of the pressure excess. The percentage of distortion is approximately proportional to the applied pressure excess.

3. *Fluid acceleration.* The effect of fluid inertia is to modify the time constants of the system. Both the attenuation of the fundamental and the magnitude of harmonic distortion are affected. A dimensionless parameter z analagous to the "Q" of an electrical system characterizes the fluid regime and determines whether fluid inertia may or may not be neglected.

When fluid inertia is negligible, a transmission tube acts like a highly damped system; when fluid inertia is large a transmission tube acts like an undamped system, and elementary acoustic theory is applicable.

4. *Finite length of tubing.* The effect of fluid acceleration at the ends of the tube results in further distortion of wave form, which must be taken into account in short tubes.

5. *Heat conduction.* If there were no heat transfer from outside the tube to inside, the oscillatory processes would take place adiabatically; if there were perfect heat transfer into and through the tube, the processes would take place isothermally. The effect of finite heat conduction is to make the real process occur in between these extremes, although in a rather complicated fashion. At low frequencies the process may be regarded as isothermal.

Although an exact result is given in the appendix, it is advantageous to utilize the thermodynamic equation of condition, discussed in the following section, for elucidating the problem of attenuation in tubing.

V. Thermodynamic Equation of Condition

In the case of an oscillatory variation of fluid flow, the equation relating the thermodynamic parameters of the fluid lie between the adiabatic and the isothermal equations of condition. For high frequencies, as in sound waves, it is well known that the adiabatic equation holds. However, for viscously damped motion, the adiabatic relation is not, in general, attained.

For a gas, we assume and justify in the appendix the processes can be described as "polytropic", that is, characterized by a constant exponent n, in the expression

$$\left.\begin{aligned} p &= c\rho^n \\ 1+\xi &= \eta^n \end{aligned}\right\} \tag{19}$$

with

$$1 \leqq |n| \leqq \gamma,$$

where

n = exponent of the "polytropic" expansion in the tube

γ = ratio of specific heats

η = density ratio (ρ/ρ_0)

ρ_0 = average density in the tube.

c is used to indicate any constant.

The viscosity of gases is independent of the pressure, and, as an approximation, proportional to

the absolute temperature. (The more rigorous approximation is that the viscosity is proportional to $[T]^{1/2}/[1+c/T]$ but over a small range this can be approximated by the temperature to a power close to one. For example, for air at room temperature, a power of 0.8 fits experimental data quite well. The difference from unity is unimportant for our purpose.)

Therefore,

$$\left.\begin{aligned} \mu &= cT, \\ \frac{\mu}{\mu_0} &= (1+\xi)^{\frac{n-1}{n}}, \\ \frac{\mu}{\mu_0} &= \eta^{n-1}, \end{aligned}\right\} \tag{20}$$

follows from the gas laws and eq 19. Here μ is the instantaneous fluid viscosity. and T is the absolute temperature.

Equations 19 and 20 thus express the variation of viscosity, density, and pressure in a polytropic process in a gas. At low frequencies, the polytropic exponent may be taken as equal to unity.

For liquids, we assume that the equation of condition in a polytropic process is given by

$$\rho = \rho_0 + cp^n, \tag{21}$$

where

$$1 \leqq |n| \leqq \gamma.$$

For liquids, however, γ lies so close to unity that we may satisfactorily assume $n=1$.

Equation 21 can then be written in the form

$$\eta = 1 + b\xi, \tag{22}$$

where b=a compressibility factor $(=k_0 p_0)$

k_0=liquid compressibility at average conditions in the tube.

The variation in viscosity of a liquid over a small range of temperature can be neglected, so that in a polytropic process

$$\mu = \mu_0. \tag{23}$$

Actually the implication in eq 22 and 23 is that in a liquid-filled transmission line, the effect of conditions appreciably different from isothermal is negligible.

It is also necessary to take into account heat exchange at the pressure element.

For an isothermal process with a gas in the instrument volume, we previously assumed that

$$Q = \frac{V}{p_0}\frac{\partial p}{\partial t} \tag{5}$$

represents the influx of fluid. If, instead, a polytropic process in the instrument is assumed, characterized by an exponent, m (the heat exchange may differ in the tube and instrument volume so that m is not necessarily equal to n), then eq. 5 should be modified to

$$\left.\begin{aligned} Q &= \frac{V}{mp}\frac{\partial p}{\partial t} \\ Q &= \frac{n}{m}\frac{V}{\rho}\frac{\partial \rho}{\partial t} \end{aligned}\right\} \tag{24}$$

in the case of gases; or to

$$Q = \frac{Vb}{p_0}\frac{\partial p}{\partial t}, \tag{25}$$

for liquids.

If the fluid is regarded as a spring, the exponent of the polytropic process for a gas, or the compressibility of a liquid may be viewed as quantities that make the fluid spring stiffer in the case of gases, or almost infinitely stiff in the case of liquids. It is shown in the appendix that these polytropic exponents modify the time constants of the tube and volume.

VI. General Procedure, with Examples, for Computing Transmitted Pressure

The computation of the attenuation and phase lag at one end of a transmission tube of a sinusoidal pressure variation imposed at the other end can be carried out with the aid of figures 2 to 9, These figures are based upon the theory largely developed in the appendix. The computations are made primarily for the attenuation at the fundamental frequency. An estimate of the distortion arising from finite input amplitudes with high damping is made in the appendix. The computation for the first harmonic in the distorted output can be made with the aid of figures 8 and 9. An outline of procedure for making computations follows.

1. Compute

$$z = \frac{D^2}{4}\frac{\omega}{\nu_0}, \tag{26}$$

a dimensionless parameter of the fluid regime that characterizes the amount of damping present. When this parameter is less than 1 (large damping), use figures 2 and 3; when greater than 100 (small damping), use figures 6 and 7. For inter-

mediate values of this parameter, use figures 4 and 5 as an aid to interpolation.

2. Compute the attenuation factors

$$\chi_{T_0}=\frac{32\mu_0\omega}{p_0}\left(\frac{L}{D}\right)^2, \tag{27}$$

$$\frac{\chi_{I_0}}{\chi_{T_0}}=\frac{1}{m}\left(\frac{V}{AL}\right), \tag{28}$$

for a gas, or

$$\chi_{T_0}=32\mu_0 k_0\omega\left(\frac{L}{D}\right)^2\left(1+\frac{p_0-p_a}{p_0}\frac{1}{k_0E}\frac{D}{s}\right), \tag{29}$$

$$\frac{\chi_{I_0}}{\chi_{T_0}}=\frac{V}{AL}\frac{1}{\left(1+\frac{p_0-p_a}{p_0}\frac{1}{k_0E}\frac{D}{s}\right)}, \tag{30}$$

for a liquid. These quantities, χ_{T0} and χ_{I0}, are factors based on the tube volume and instrument volume, respectively. The zero subscript means that they are values for the case of large damping.

3. Compute the input pressure excess

$$\xi_0=\frac{\Delta p}{p_0}. \tag{31}$$

4a. For values of z less than 1, enter figure 2 with χ_{T0} and χ_{I0}/χ_{T0} to find the amplitude ratio $|\tilde{\xi}_{OL}/\xi_0|_0$ and enter figure 3 to find the lagging phase angle $(\delta_O)_0$.

4b. The output pressure excess is then computed from

$$|\tilde{\xi}_{OL}|_0=\xi_0\left|\frac{\tilde{\xi}_{OL}}{\xi_0}\right|_0. \tag{32}$$

5a. For values of z greater than 100, compute

$$\frac{\omega L}{C}=\left[\frac{z\chi_{T0}}{8\gamma}\right]^{\frac{1}{2}}, \tag{33}$$

$$\frac{\chi_I}{\chi_T}=\gamma\left(\frac{\chi_{I0}}{\chi_{T0}}\right). \tag{34}$$

For liquids, assume $\gamma=1$.

The quantities χ_I and χ_T are the attenuation factors for the case of low damping. With low damping, it is convenient to use the dimensionless parameter $\omega L/C$, which is proportional to frequency, as the independent variable.

5b. Enter figure 6 with $\omega L/C$ and χ_I/χ_T to find the amplitude ratio $|\tilde{\xi}_{OL}/\xi_0|$ and enter figure 7 to find the lagging phase angle δ_O. It is necessary to estimate the phase angle by interpolation. For very small values of χ_{T0} compared to 1, the lagging phase angle is zero up to the first resonance. In figure 7, curves have been presented to indicate the phase angle for $[\gamma\chi_{T0}/16]^{1/2}=0$ and $[\gamma\chi_{T0}/16]^{1/2}=\infty$. One may linearly interpolate between these curves on the basis of $[\gamma\chi_{T0}/16]^{1/2}$ for values lying between 0 and 1.

6a. For values of z lying between 1 and 100, one may interpolate between the values of amplitude ratio and lagging phase angle obtained in step 4a and those obtained in step 5b by the use of figures 4 and 5. Enter figures 4 and 5 with χ_{T0} and χ_{I0}/χ_{T0} to find the amplitude ratio $|\tilde{\xi}_{OL}/\xi_0|$ and lagging phase angle δ_O. These are the values for $z=6.25$. In order to interpolate, plot a logarithmic graph with z as abscissa and the amplitude ratio or phase angle as ordinate. Plot the values from step 4a at $z=1$, from step 6a at $z=6.25$, and from step 5b at $z=100$, draw a curve through these three points, and interpolate on this curve for the intermediate value of z.

1. Computation of Double Frequency Distortion

1. This computation represents only an estimate of the double frequency distortion and is strictly valid only for values of z less than 1.

Compute χ_{T0} and χ_{I0}/χ_{T0}. Enter figures 8 and 9 to obtain the relative amplitude ratio $|\tilde{\xi}_{1L}/\xi_0|_0/\xi_0$ and leading phase angle $(\delta_1)_0$ for the double frequency wave. The leading phase angle is measured on the time scale of the fundamental, where both the fundamental and double frequency waves are cosine terms.

2. Compute the pressure excess of the double frequency $|\tilde{\xi}_{1L}|_0$ from

$$|\tilde{\xi}_{1L}|_0=\left(\frac{1}{\xi_0}\left|\frac{\tilde{\xi}_{1L}}{\xi_0}\right|\right)_0\xi_0^2. \tag{35}$$

The various quantities in the above section are defined below:

μ_0 = mean fluid viscosity.
ν_0 = mean kinematic viscosity.
p_0 = mean fluid pressure.
p_a = ambient pressure external to the tube.
Δp = amplitude of the applied sinusoidal pressure.
ξ_0 = applied fractional pressure excess.
$\tilde{\xi}_{OL}$ = pressure excess of the fundamental at the instrument volume.
$\tilde{\xi}_{1L}$ = pressure excess of the double frequency at the instrument volume.
δ_O = lagging phase angle of the fundamental at the instrument volume.
δ_1 = leading phase angle of the double frequency at the instrument volume.

k_0=mean fluid compressibility.

V=equivalent rigid internal volume of the instrument.

A=internal cross section of the tube.

D=internal diameter of the tube.

s=wall thickness of the tube (assumed small compared to the diameter).

E=elastic modulus of the tube material.

L=length of the tube.

C=velocity of sound in the fluid.

γ=ratio of specific heats of the fluid (assumed to be one for liquids).

m=coefficient of the polytropic process in the instrument volume. (In lieu of other information, it may be assumed to be one.)

z=dimensionless parameter characterizing the fluid regime.

ω=angular frequency applied.

χ_T=attenuation factor based on the tube volume.

χ_I=attenuation factor based on the instrument volume.

Subscript T refers to parameters based on tube volume; subscript I refers to parameters based on end volume; O or 1 following a T or I denotes the fundamental or first harmonic; an end subscript of 0 denotes a value for the case of large damping.

The attenuation of the fundamental may be validly computed from the formulas developed in this paper when

$$\left.\begin{aligned}\frac{\nu_0}{CD}&<1\\ \frac{\nu_0\omega}{C^2}&<1\end{aligned}\right\} \tag{36}$$

The second harmonic distortion, which was only estimated approximately, may be validly computed from the formulas developed when

$$z=\frac{\omega D^2}{4\nu_0}<1, \tag{37}$$

and when the applied pressure amplitude is sufficiently small at the applied frequency to permit laminar flow. 3. Compute the mean pressure in the instrument volume, which is larger than the mean pressure at the tube entrance by

$$\xi_0\Delta p[1-|\tilde{\xi}_{OL}/\xi_0|_0^2]/4$$

2. Examples of Computations

The calculation of attenuation by the general procedure outlined above will be illustrated by a number of examples.

(a) What is the longest length of 3/16-in.-inside-diameter tubing that can be used to transmit air pressure to a Bourdon pressure gage (equivalent internal volume assumed negligible) up to a frequency of ½ c/s with a loss in amplitude not greater than 25 percent? What will be the double frequency distortion? For air assume $\mu_0=2\times10^{-4}$ poise, $\nu_0=1/6$ stokes, $m=1$, $\gamma=1.4$, $p_0=10^6$ dynes/cm^2 (atmospheric pressure), angular frequency $\omega=\pi$.

Using eq 26, $z=1.1$ (computed in consistent units). This value is sufficiently close to unity to permit the use of figures 2 and 3. Enter figure 2 with $|\tilde{\xi}_{OL}/\xi_0|_0=0.75$ and $\chi_{I0}/\chi_{T0}=0$, since the instrument volume is negligible, to find $\chi_{T0}=2.1$. Compute L in eq 27 to be 160 feet.

Entering figure 3 with $\chi_{T0}=2.1$, to find that the maximum phase lag will be 53 degrees.

Entering figure 8 to find that the relative amplitude of the double frequency $|\tilde{\xi}_{1L}/\xi_0|_0/\xi_0=0.35$. For initial pressure excesses of 0.1, 0.3, and 1, respectively, the double frequency amplitude, relative to the input amplitude, will be 3½, 10½, and 35 percent, while the mean pressure will increase 0.0010, 0.010, and 0.11 of an atmosphere, respectively.

(b) What lengths of 0.1-in.-inside-diameter tubing (nominally 3/16-in.-outside-diameter tubing) can be used for quality transmission of air pressure for frequencies up to 1, 10, 100, 1,000 c/s into pressure instruments with equivalent rigid volumes of 0.1 and 1 in.^{3}?

We will define quality transmission as that in which there is no more than ±5-percent change in fundamental amplitude or more than ±30° phase shift (whichever is more stringent).

Assume that $\mu_0=2\times10^{-4}$ poise, $\nu_0=1/6$ stokes, $m=1$, $\gamma=1.4$, $D=0.1$ in., $A=0.0079$ in.^{2}, $p_0=10^6$ dynes/cm^2, $\rho_0=0.0012$ g/cm^3.

We will calculate for each frequency separately.

b (1). *$f=1$ c/s:*

Using eq 26, $z=0.61$; therefore, use figures 2 and 3.

Assume $AL=\infty$, therefore, by eq 28, $\chi_{I0}/\chi_{T0}=0$.

Enter figure 2 for $|\tilde{\xi}_{OL}/\xi_0|_0=0.95$ to find $\chi_{T0}=0.80$.

Enter figure 3 for $(\delta_0)_0=30°$ to find $\chi_{T0}=1.1$; use 0.80 since it is more stringent.

Calculate L from eq 27 to be 450 in.

Calculate AL to be 3.5 in.^{3}

Compute χ_{I0}/χ_{T0} from eq 28 to be 0.029 for $V=0.1$ in.^{3}; 0.29 for $V=1$ in.^{3}

On figure 2, χ_{T0} is modified negligibly for $V=0.1$ in.^{3}

Therefore, $L=450$ in. $=37$ ft for $V=0.1$ in.^{3}

Reenter figure 2 for $|\tilde{\xi}_{0L}/\xi_0|_0=0.95$, $\chi_{I0}/\chi_{T0}=0.29$ to find $\chi_{T0}=0.5$

Calculate L to be 350 in. $=29$ ft for $V=1$ in.^{3}

b (2). *$f=1{,}000$ c/s:*

Using eq 26, $z=610$; therefore, use figures 6 and 7.

Assume $\chi_I/\chi_T=49$ (the line volume will probably be small).

Enter figure 6 for $|\tilde{\xi}_{0L}/\xi_0|=1.05$ to find $\omega L/C=0.031$.

Calculate L from eq 33, 26, and 27 to be 0.066 in.

Calculate AL to be 0.00052 in.^{3}

Using eq 34, it is seen that χ_{I0}/χ_{T0} is greater than assumed, so that $\omega L/C$, and therefore L, is less than the previous estimate. One may note that the estimated length will be so small that the theory essentially predicts that no transmission tubing at all may be used. In fact, the acoustic impedance of the entrance orifice into the pressure instrument or the mechanical impedance of the pressure instrument itself will probably govern the response at this high frequency.

b(3). *$f=10$ c/s:*

Using eq 26, $z=6.1$; therefore, use figures 4 and 5.

Assume $AL=\infty$, therefore, $\chi_{I0}/\chi_{T0}=0$.

Enter figure 4 with $|\tilde{\xi}_{0L}/\xi_0|=1.05$ and $\gamma=1.4$ to find $\chi_{T0}=0.12$.

Compute L from eq 27 to be 58 in.

Compute AL to be 0.45 in.^{3}.

Compute χ_{I0}/χ_{T0} from eq 28 to be 0.22 for $V=0.1$ in.^{3}, $=2.2$ for $V=1$ in.^{3}

In figure 4, χ_{T0} is modified to about 0.07 for $V=0.1$ in.^{3}

Therefore, L is reduced to about 4 ft for $V=0.1$ in.^{3}

Enter figure 4 for $|\tilde{\xi}_{0L}/\xi_0|=1.05$, and $\chi_{I0}/\chi_{T0}=2$ to find $\chi_{T0}=0.018$.

Compute L to be 22 in. for $V=1$ in.^{3}

Compute AL to be 0.17 in.^{3}

Compute $\chi_{I0}/\chi_{T0}=6$.

Enter figure 4 to find $\chi_{T0}=0.007$.

Compute L to be 14 in.

Compute AL to be 0.11 in.^{3}

Compute $\chi_{I0}/\chi_{T0}=9$.

Enter figure 4 to find $\chi_{T0}=0.004$.

Compute L to be 11 in.

Compute AL to be 0.09 in.^{3}

Compute $\chi_{I0}/\chi_{T0}=11$.

In figure 4, χ_{T0} is modified negligibly.

Therefore $L=$about 1 ft for $V=1$ in.^{3}

To check the phase angle, enter figure 5 with $\chi_{I0}/\chi_{T0}=11$, and $\chi_{T0}=0.005$, to find 4°.

b(4). *$f=100$ c/s.*

$z=61$ (interpolation is necessary).

First estimate from figure 6 and 7.

Assume $\chi_I/\chi_T=9$.

Enter figure 6 to find $\omega L/C=0.068$

As in b (2), compute L to be 1.5 in.

Compute AL to be 0.011 in.

Compute $\chi_I/\chi_T=9.1$ for $V=0.1$ in.^{3}; $=91$ for $V=1$ in.^{3}

By figure 6, $\omega L/C$ is negligibly modified for $V=0.1$ in.^{3};

Therefore $L=1.5$ in. for $V=0.1$ in.^{3} is our first estimate.

For $V=1$ in.^{3}, we find again that an extremely small tube is predicted, so that the impedance of the entrance orifice will probably govern.

For $V=0.1$ in.^{3} and $L=1.5$ in., estimate $[\gamma\chi_{T0}/16]^{1/2}$ to be .01.

From figure 7 we find that the phase lag is negligible.

Compute $\chi_{T0}=0.0009$, from (8.2) for $\omega=200\pi$.

Enter figure 4 for $\chi_{I0}/\chi_{T0}=9$ to find $|\tilde{\xi}_{0L}/\xi_0|=1.00$.

Interpolating between $|\xi_{0L}/\xi_0|=1$ at $z=6.25$ and $|\xi_{0L}/\xi_0|=1.05$ at $z=100$ for $z=61$, we find $|\tilde{\xi}_{0L}/\xi_0|$ is negligibly affected.

Therefore $L=1.5$ in. for $V=0.1$ in.^{3}

VII. Appendix. Development of the Theory

1. Introduction

The difficulties of deriving, elucidating, and comprehending the mathematical results of transmission in tubing from a rigorous point of view, have led the author to treat the problem in a series of somewhat artificial steps. Thus in the previous sections, the elementary solution was presented, to give the reader a general view of the problem, even though many of the details of the solution were slurred over. Here steps are taken, one at a time, to remove the restrictive assump-

tions made in deriving the elementary solution. Nevertheless, a complete solution to the problem is not obtained. All first-order effects are treated to the point where the solution is correct to frequencies well into the sonic region. However, only an elementary treatment is given for the second-order distortion effects. It is felt that when these second-order effects become appreciable, the solution presented is of no quantitative utility to the instrument system designer or user, but is only indicative as to order of magnitude.

2. Theory Corrected for Compressibility

(Infinitesimal Oscillatory Pressures)

In this approximation, the assumptions are Poiseuille's law of viscous resistance; small fractional pressure excess; and that density, pressure, and viscosity are related by the equation of condition.

For gases one can then write

$$\left.\begin{aligned} \frac{\partial p}{\partial x} &= -\frac{128}{\pi}\frac{\mu}{D^4}Q, \\ \text{or} \\ \rho\frac{\partial p}{\partial x} &= -\frac{128}{\pi}\frac{\mu}{D^4}M, \end{aligned}\right\} \tag{1}$$

for Poiseuille's law, and

$$\frac{\partial M}{\partial x} = -A\frac{\partial p}{\partial t} \tag{2}$$

for the equation of continuity.

One can eliminate the mass flow M, to obtain

$$\frac{\partial}{\partial x}\left(\frac{\rho}{\mu}\frac{\partial p}{\partial x}\right) = \frac{32}{D^2}\frac{\partial \rho}{\partial t}. \tag{38}$$

By virtue of the assumption of small pressure excess, and the equations of condition (eq 19 and 20), we can disregard the differentiation of ρ/μ in eq. 38, and replace it by its mean value. Equation 38 then becomes

$$\left.\begin{aligned} \frac{\partial^2 p}{\partial x^2} &= \frac{32\mu_0}{np_0D^2}\frac{\partial p}{\partial t}, \\ \text{or} \\ \frac{\partial^2 \xi}{\partial x^2} &= \frac{32\mu_0}{np_0D^2}\frac{\partial \xi}{\partial t}. \end{aligned}\right\} \tag{39}$$

Utilizing the previous definition of λ_0 (eq 10), eq 39 becomes

$$\left.\begin{aligned} \frac{\partial^2 \xi}{\partial x^2} &= \left(\frac{AL}{V}\frac{\lambda_0}{n}\right)\frac{1}{L^2}\frac{\partial \xi}{\partial t} \\ \text{or} \\ \frac{\partial^2 \xi}{\partial x^2} &= \frac{\lambda_{T0}}{L^2}\frac{\partial \xi}{\partial t} \end{aligned}\right\} \tag{40}$$

where

$$\lambda_{T0} = \frac{AL}{V}\frac{\lambda_0}{n}. \tag{41}$$

The significance of the new time constant λ_{T0} can be understood by inspection of the definition of λ_0 (eq 10). One may note that λ_{T0} is a time constant based on the tube volume, AL, instead of the instrument volume, V; and that it gives weight to the exponent of the polytropic process in the tube. It is thus related to the equivalent distributed electrical capacitance of the tube. The weighting by the exponent, n, arises from the fact that it represents the additional "stiffness" of the air column in the tube as a polytropic spring.

If, as in the elementary solution, we separate our pressure variable into a space and time part

$$\xi = \tilde{\xi}e^{j\omega t}, \tag{11}$$

eq 40 becomes

$$\left.\begin{aligned} \frac{d^2\tilde{\xi}}{dx^2} &= \frac{\lambda_{T0}\omega}{L^2}j\tilde{\xi} \\ \text{or} \\ \frac{d^2\tilde{\xi}}{dx^2} &= \frac{\chi_{T0}}{L^2}j\tilde{\xi} \end{aligned}\right\} \tag{42}$$

where

$$\chi_{T0} = \lambda_{T0}\omega \tag{43}$$

The quantity χ_{T0} is an attenuation factor based on the tube volume.

Equation 42 may be compared with the corresponding equation of the elementary solution, eq 12. It may be noted that it is necessary that χ_{T0} be small in order for the elementary solution to be valid.

Referring now to eq 42, the boundary conditions are

at $x=0$

$$\tilde{\xi} = \xi_0, \tag{13}$$

and at $x=L$

$$\frac{d\tilde{\xi}}{dx} = -\left(\frac{\lambda_0\omega}{m}\right)j\frac{\tilde{\xi}}{L}, \tag{44}$$

(see eq 5, 9, and 24).

886334—50——7

We may redefine a time constant and attenuation factor for the instrument volume, which takes into account the polytropic process as

$$\left.\begin{aligned}\lambda_{I0}&=\frac{\lambda_0}{m}\\ \chi_{I0}&=\lambda_{I0}\omega\end{aligned}\right\} \tag{45}$$

At $x=L$, eq 44 therefore becomes

$$\frac{d\tilde{\xi}}{dx}=-\frac{\chi_{I0}}{L}j\tilde{\xi} \tag{46}$$

The solution to eq 42, which satisfies boundary conditions (eq 13 and 46) is

$$\frac{\tilde{\xi}}{\xi_0}=\frac{e^{-\psi_{T0}}(\psi_{T0}-\psi_{I0})e^{\psi_{T0}\frac{x}{L}}+e^{\psi_{T0}}(\psi_{T0}+\psi_{I0})e^{-\psi_{T0}\frac{x}{L}}}{e^{\psi_{T0}}(\psi_{T0}+\psi_{I0})+e^{-\psi_{T0}}(\psi_{T0}-\psi_{I0})}, \tag{47}$$

where

$$\left.\begin{aligned}\psi_{T0}&=\left[\frac{\chi_{T0}}{2}\right]^{1/2}(1+j)\\ \psi_{I0}&=j\chi_{I0}\end{aligned}\right\} \tag{48}$$

The new ψ's, which shall be referred to as attenuation parameters, are

ψ_{T0} an attenuation parameter depending on tube volume;

ψ_{I0} an attenuation parameter depending on the instrument volume.

The ratio of the fractional pressure excess at the end of the tube $\tilde{\xi}_L$ to that at the beginning of the tube ξ_0 is then

$$\frac{\tilde{\xi}_L}{\xi_0}=\frac{\psi_{T0}}{\psi_{T0}\cosh\psi_{T0}+\psi_{I0}\sinh\psi_{T0}} \tag{49}$$

It is instructive to examine the limiting values of this equation. For small ψ_{T0}, the attenuation approaches

$$\frac{\tilde{\xi}_L}{\xi_0}=\frac{1}{1+\psi_{I0}}=\frac{1}{1+j\chi_{I0}}, \tag{50}$$

the same result as in the elementary theory (see eq 16).

For small values of ψ_{I0}, the attenuation approaches

$$\frac{\tilde{\xi}_L}{\xi_0}=\frac{1}{\cosh\psi_{T0}}, \tag{51}$$

which for small ψ_{T0} becomes

$$\frac{\tilde{\xi}_L}{\xi_0}=\frac{1}{1+\frac{\psi_{T0}^2}{2}}=\frac{1}{1+\frac{\chi_{T0}}{2}j}. \tag{52}$$

The form of eq 50 and 52 is similar. In fact, for small values of both ψ_{T0} and ψ_{I0} it is possible to define a composite attenuation factor χ by the relation

$$\left.\begin{aligned}\chi&=\chi_{I0}+\frac{\chi_{T0}}{[6]^{1/2}}\\ \lambda&=\lambda_{I0}+\frac{\lambda_{T0}}{[6]^{1/2}}\end{aligned}\right\} \tag{53}$$

or

such that the real magnitude of the attenuation is approximately

$$\left|\frac{\tilde{\xi}_T}{\xi_0}\right|=\frac{1}{[1+\chi^2]^{1/2}}, \tag{18}$$

which preserves the form of the elementary solution.

Equation 18 can be interpreted as meaning that the "proper" time constant of the system can be obtained by adding to the n weighted volume of the instrument, $1/[6]^{1/2}$ of the m weighted volume of the tube, and substituting this in the elementary formula for the time constant of the system.

In principle, for larger values of ψ_{T0} or ψ_{I0}, a coupling coefficient (of approximately unity) could be introduced as an addition to the coefficient $1/[6]^{1/2}$, which would vary somewhat with the relative magnitude of ψ_{T0} and ψ_{I0}, to permit strict preservation of the elementary form. It is, however, simpler to compute attenuation from eq 49.

For liquids, we start from eq 38.

$$\frac{\partial}{\partial x}\left(\frac{\rho}{\mu}\frac{\partial p}{\partial x}\right)=\frac{32}{D^2}\frac{\partial\rho}{\partial t}. \tag{38}$$

As before, with the aid of eq 22 and 23, we obtain the result

$$\left.\begin{aligned}\frac{\partial^2\xi}{\partial x^2}&=\frac{32\mu_0 b}{p_0 D^2}\frac{\partial\xi}{\partial t}\\ \frac{\partial^2\xi}{\partial x^2}&=\frac{\lambda_{T0}}{L^2}\frac{\partial\xi}{\partial t}\\ \frac{d^2\tilde{\xi}}{dx^2}&=\frac{\chi_{T0}}{L^2}j\tilde{\xi}\end{aligned}\right\} \tag{54}$$

or

where

$$\left.\begin{aligned}\lambda_{T0}&=\frac{AL}{V}\,b\lambda_0\\ \chi_{T0}&=\lambda_{T0}\omega.\end{aligned}\right\} \qquad (55)$$

The boundary condition at $x=0$ is

$$\bar{\xi}=\xi_0 \qquad (13)$$

and at $x=L$

$$\left.\begin{aligned}\frac{d\bar{\xi}}{dx}&=-(\lambda_0 b\omega)j\,\frac{\bar{\xi}}{L}\\ \text{or}\qquad \frac{d\bar{\xi}}{dx}&=-\chi_{T0}j\,\frac{\bar{\xi}}{L}\end{aligned}\right\} \qquad (56)$$

where

$$\left.\begin{aligned}\lambda_{T0}&=\lambda_0 b\\ \chi_{T0}&=\lambda_{T0}\omega\end{aligned}\right\} \qquad (57)$$

(see eq 5, 9, and 25).

The form of eq 54 and 56 is identical with eq 42 and 46, with the difference that the coefficient in the λ's is the very small compressibility factor rather than the reciprocal of the exponent of the polytropic process. Physically, this simply means that the liquid is a spring of almost infinite stiffness compared to the gas.

Because of the formal identity of the equations, the previous solution holds in toto, with the modified value of λ_{T0}. The following interpretation is now possible for the elementary result that there is no attenuation with liquids. The λ_0 time constant of elementary theory did not take into account the effect of liquid compressibility, which is small. If, however, λ_0 is weighted by b (i. e., $\lambda=b\lambda_0$) then the same attenuation curve holds for both liquids and gases, but with liquids we operate on the very beginning portion of the attenuation curve for gases.

There is one complication that should be considered in liquid tube attenuation. Because of the small compressibility of liquids, it is often possible that the flexibility of the tube gives rise to a compressibility comparable to that of the liquid. The simplest way of taking into account the flexibility of the tube is to define and replace the compressibility factor of the liquid by an effective value $\bar{b}$ and $\bar{k}$.

$$\left.\begin{aligned}\bar{b}&=b+\frac{p_0-p_a}{E}\,\frac{D}{s}\\ \bar{k}&=k+\frac{p_0-p_a}{p_0E}\,\frac{D}{s}\end{aligned}\right\}, \qquad (58)$$

where

p_0=mean liquid pressure;
p_a=ambient external pressure (usually atmospheric);
E=elastic modulus of the tube material;
s=wall thickness of the tube.

In the derivation of eq 58, the assumption has been made that the thickness of the tube wall is small compared to the tube diameter.

3. Theory Corrected for Finite Oscillatory Pressures

In this section, we will determine the effect of finite fractional pressure excess on the attenuation in a tube. We assume only that the Poiseuille velocity distribution holds. We will show that the effect of finite pressure excesses is to excite higher harmonics, resulting in a distortion of wave form, and to raise the mean pressure along the tube. The higher harmonics are excited because of the nonlinearity of the equations.

The method of solution selected will be that of expansion in harmonic series in which the excitation of sum frequencies only are considered and the difference frequencies are neglected, so that the solutions obtained are only valid for the leading term of each harmonic. The second order term in the variation of the mean pressure will be estimated separately. We will assume open functions of the distance coordinate for the coefficients of each harmonic term of the series and show that the expansion is valid for moderate values of the initial pressure excess. It is obvious that these distance dependent coefficients must be the solutions of second-order differential equations in order to provide two sets of adjustable constants to satisfy the boundary conditions at the two ends of the tube. However, by considering the solution for an infinite tube (for which only one set of boundary conditions is required) we shall be able to discuss the question of convergence of the solutions.

For the purposes in view, it will turn out to be convenient to derive the equations on a density basis. Density and pressure are, of course, related through the equation of condition.

For gases, we start from

$$\frac{\partial}{\partial x}\left(\frac{\rho}{\mu}\frac{\partial p}{\partial x}\right)=\frac{32}{D^2}\frac{\partial \rho}{\partial t}. \tag{38}$$

By algebraic manipulation, in which eq 19 and 20 are used to eliminate viscosity and pressure, we obtain

$$\left.\begin{aligned}\frac{\partial}{\partial x}\left(\eta\frac{\partial \eta}{\partial x}\right)&=\frac{\lambda_{T0}}{L^2}\frac{\partial \eta}{\partial t},\\ \text{or}\qquad \frac{\partial^2 \eta^2}{\partial x^2}&=\frac{2\lambda_{T0}}{L^2}\frac{\partial \eta}{\partial t},\end{aligned}\right\} \tag{59}$$

a nonlinear partial differential equation.

Assume as solution for the density ratio

$$\eta=1+\eta_1 e^{j\omega t}+\eta_2 e^{2j\omega t}+\eta_3 e^{3j\omega t}+\ \ldots\ , \tag{60}$$

where η_i is the fractional density amplitude ratio of each harmonic (functions of x).

At the moment assume that the applied pressure wave has all the mathematical properties necessary to make the Fourier expansion of eq 60 valid. We will discuss this point again.

When eq 60 is substituted in eq 59 and the coefficients of like terms in the respective harmonics equated, the following system of differential equations result for the coefficients η_i.

$$\left.\begin{aligned}
1\left(\frac{\psi_{T0}}{L}\right)^2\eta_1&=\frac{1}{2}\frac{d^2}{dx^2}(\eta_1\eta_0+\eta_0\eta_1)\\
2\left(\frac{\psi_{T0}}{L}\right)^2\eta_2&=\frac{1}{2}\frac{d^2}{dx^2}(\eta_2\eta_0+\eta_1\eta_1+\eta_0\eta_2)\\
3\left(\frac{\psi_{T0}}{L}\right)^2\eta_3&=\frac{1}{2}\frac{d^2}{dx^2}(\eta_3\eta_0+\eta_2\eta_1+\eta_1\eta_2+\eta_0\eta_3)\\
&\ \ \vdots\qquad\qquad\ \ \vdots\\
i\left(\frac{\psi_{T0}}{L}\right)^2\eta_i&=\frac{1}{2}\frac{d^2}{dx^2}(\eta_i\eta_0+\eta_{i-1}\eta_1+\cdots+\eta_1\eta_{i-1}+\eta_0\eta_i)
\end{aligned}\right\} \tag{61}$$

The coefficient $\eta_0(=1)$ has been added for completeness.

From eq 61 it can be shown that the coefficients η_i for an infinite tube are equal to

$$\left.\begin{aligned}\eta_i=\overline{\eta}_i e^{-(0+[0]^{1/2})y}&-\frac{\overline{\eta}_{i-1}\overline{\eta}_1 e^{-(1+[i-1]^{1/2})y}}{(1\times 0+1\times 2[i-1]^{1/2})}+\\ &\frac{\overline{\eta}_{i-2}\overline{\eta}_1^2 e^{-(2+[i-2]^{1/2})y}}{(1\times 0+1\times 2[i-2]^{1/2})\ (2\times 1+2\times 2[i-2]^{1/2})}-\\ &\frac{\overline{\eta}_{i-3}\overline{\eta}_1^3 e^{-(3+[i-3]^{1/2})y}}{(1\times 0+1\times 2[i-3]^{1/2})\,(2\times 1+2\times 2[i-3]^{1/2})\,(3\times 2+3\times 2[i-3]^{1/2})}+\cdots\end{aligned}\right\} \tag{62}$$

The solution of these equations consists of a complementary part that introduces two new constants for each coefficient η_i, and a particular solution that depends upon the solutions for coefficients with lower values of i. The latter part represents the excitation of higher sum frequency modes.

Detailed investigation of the convergence of the solutions for the various coefficients leads to the following conclusions:

The differential equations of eq 61 will admit physically admissible and convergent solutions for *any* bounded periodic pressure or density wave at the origin because (1) either the wave at the origin has a derivative that is of limited variation, in which case the solution of eq 59 in series (eq 60) is always valid; or (2) if it does not, spatial attenuation of viscous waves occurs so rapidly for higher harmonics that the wave will have a derivative of limited variation at a short distance beyond the origin, so that as far as effects downstream are concerned, the given input wave can be replaced *at the origin* by a similar looking function (i. e., a finite polynomial instead of an infinite Fourier series) whose derivative is of limited variation. As illustrations, we can replace a square wave by its first few harmonics, or a Weierstrass function by a smooth integrable function. In simpler language this means that in a viscous transmission tube, detailed or sharp wiggles in the initial disturbance (high harmonics) are not transmitted.

The more practical question as to the rapidity of convergence of the series solution for the attenuation of a given entrance disturbance can be answered approximately by recourse to the solution for an infinite tube, for which only one set of boundary conditions must be satisfied.

where

$$y=\psi_{r0}\frac{x}{L}. \tag{63}$$

Here $\bar{\eta}_i$ is the constant of integration for the complementary solution of each η_i, and y is a dimensionless distance variable.

Substituting the value of the coefficients from eq 62 into eq 60, we obtain the result that, if at the origin ($y=0$), the density is written in the form

$$\left.\begin{aligned}\eta=1+&\bar{\eta}_1e^{j\omega t}+\\&\left(\bar{\eta}_2-\frac{\bar{\eta}_1\bar{\eta}_1}{1\times0+1\times2[1]^{1/2}}\right)e^{2j\omega t}+\\&\left(\bar{\eta}_3-\frac{\bar{\eta}_2\bar{\eta}_1}{1\times0+1\times2[2]^{1/2}}+\right.\\&\left.\frac{\bar{\eta}_1\bar{\eta}_1^2}{(1\times0+1\times2[1]^{1/2})(2\times1+2\times2[1])^{1/2}}\right)e^{3j\omega t}+\cdots\end{aligned}\right\} \tag{64}$$

at any other point y, the density wave will be

$$\left.\begin{aligned}\eta=1+&\bar{\eta}_1e^{-(0+[1]^{1/2})y}e^{j\omega t}+\\&\left(\bar{\eta}_2e^{-(0+[2]^{1/2})y}-\frac{\bar{\eta}_1\bar{\eta}_1e^{-(1+[1]^{1/2})y}}{1\times0+1\times2[1]^{1/2}}\right)e^{2j\omega t}+\\&\left(\bar{\eta}_3e^{-(0+[3]^{1/2})y}-\frac{\bar{\eta}_2\bar{\eta}_1e^{-(1+[2]^{1/2})y}}{1\times0+1\times2[2]^{1/2}}+\right.\\&\left.\frac{\bar{\eta}_1\bar{\eta}_1^2e^{-(2+[1]^{1/2})y}}{(1\times0+1\times2[1]^{1/2})(2\times1+2\times2[1]^{1/2})}\right)e^{3j\omega t}\\&+\cdots\end{aligned}\right\} \tag{65}$$

Our previous conclusion permits us to assume that expression 64 is manageable (i. e., of limited variation with a time derivative of limited variation) so that it must converge. We may therefore infer the following relations:

For large enough i

$$\left.\begin{aligned}0<&\left|\frac{\bar{\eta}_{i+1}}{\bar{\eta}_i}\right|<1\\\left|\frac{\eta_{i+1}}{\eta_i}\right|\leqq&\left|\frac{\bar{\eta}_{i+1}}{\bar{\eta}_i}e^{-\frac{y}{2[i]^{1/2}}}\right|\\0<&\left|\frac{\bar{\eta}_i}{\bar{\eta}_1}\right|<1\\\left|\frac{\eta_i}{\eta_1}\right|\leqq&\left|\frac{\bar{\eta}_i}{\bar{\eta}_1}e^{-y[i]^{1/2}}\right|.\end{aligned}\right\} \tag{66}$$

The last line in eq 66 contains our desired conclusion. We can infer from it the maximum number of terms that must be carried along in order to know the distortion to within any desired accuracy. If we assume, for example, that we are interested in only those harmonics whose content at the end of the tube is greater than 1 percent of the applied first harmonic, we can neglect all harmonics greater than the one for which

$$\left.\begin{aligned}\left|\frac{\bar{\eta}_i}{\bar{\eta}_1}\right|e^{-\psi_{r0}[i]^{1/2}}=0.01,\\\text{or}\\\left|\frac{\bar{\eta}_i}{\bar{\eta}_1}\right|e^{-\left[\frac{x_{r0}i}{2}\right]^{1/2}}=0.01.\end{aligned}\right\} \tag{67}$$

For most practical problems, it can be shown that adequate information can be obtained from a knowledge of the first and second harmonic, and rarely, the third harmonic.

To compute the harmonic distortion for a volume terminated tube, we go back to eq 61. The solution for the density wave becomes

$$\left.\begin{aligned}\eta=1+&(\bar{\eta}_{1+}e^{y}+\bar{\eta}_{1-}e^{-y})e^{j\omega t}+\\&(\bar{\eta}_{2+}e^{[2]^{1/2}y}-\bar{\eta}_{1+}^2e^{2y}+\bar{\eta}_{2-}e^{-[2]^{1/2}y}-\\&\bar{\eta}_{1-}^2e^{-2y})e^{2j\omega t}+\left(\bar{\eta}_{3+}e^{[3]^{1/2}y}-\right.\\&\bar{\eta}_{2+}\bar{\eta}_{1+}\left(\frac{3+2[2]^{1/2}}{2[2]^{1/2}}\right)e^{([2]^{1/2}+1)y}+\\&\bar{\eta}_{1+}^3\left(\frac{3}{2}\right)e^{3y}+\bar{\eta}_{3-}e^{-[3]^{1/2}y}-\\&\bar{\eta}_{2-}\bar{\eta}_{1-}\left(\frac{3+2[2]^{1/2}}{2[2]^{1/2}}\right)e^{-([2]^{1/2}+1)y}+\\&\bar{\eta}_{1-}^3\left(\frac{3}{2}\right)e^{-3y}+\bar{\eta}_{1+}\bar{\eta}_{2-}\left(\frac{3-2[2]^{1/2}}{2[2]^{1/2}}\right)e^{(1-[2]^{1/2})y}+\\&\bar{\eta}_{2+}\bar{\eta}_{1-}\left(\frac{3-2[2]^{1/2}}{2[2]^{1/2}}\right)e^{(-1+[2]^{1/2})y}-\\&\left.\bar{\eta}_{1+}\bar{\eta}_{1-}^2\left(\frac{1}{2}\right)e^{-y}-\bar{\eta}_{1-}\bar{\eta}_{1+}^2\left(\frac{1}{2}\right)e^{y}\right)e^{3j\omega t}+\cdots\end{aligned}\right\} \tag{68}$$

Here $\bar{\eta}_{i+}$, $\bar{\eta}_{i-}$ represent the two sets of integration constants necessary to take care of an outgoing and reflected wave in the tube. They are fractional density excesses.

We will consider the boundary conditions to be, for the moment, at $x=0$ ($y=0$)

$$\eta=1+\bar{\eta}_1e^{j\omega t}+\bar{\eta}_2e^{j\omega t}+\bar{\eta}_3e^{j\omega t}+\cdots \tag{69}$$

where $\bar{\eta}_i$ is the amplitude of each input harmonic in the density wave (it differs from $\bar{\eta}_i$, which represents both the input harmonic and the excitation amplitudes of that harmonic), and at

$$x=L\ (y=\psi_{T0})$$

$$\left.\begin{aligned}\eta=1+&\left[\bar{\eta}_1\frac{\psi_{T0}}{\psi_{T0}\cosh\psi_{T0}+\psi_{I0}\sinh\psi_{T0}}\right]e^{j\omega t}+\\&\left[\bar{\eta}_2\frac{[2]^{1/2}\psi_{T0}}{[2]^{1/2}\psi_{T0}\cosh[2]^{1/2}\psi_{T0}+2\psi_{I0}\sinh[2]^{1/2}\psi_{T0}}+\right.\\&\bar{\eta}_1^2\left.\frac{[2]^{1/2}\psi_{T0}^3(\cosh 2\psi_{T0}-\cosh[2]^{1/2}\psi_{T0})+2\psi_{T0}^2\psi_{I0}([2]^{1/2}\sinh 2\psi_{T0}-\sinh[2]^{1/2}\psi_{T0})+[2]^{1/2}\psi_{T0}\psi_{I0}^2(\cosh 2\psi_{T0}-\cosh[2]\psi_{T0})}{2([2]^{1/2}\psi_{T0}\cosh[2]^{1/2}\psi_{T0}+2\psi_{I0}\sinh[2]^{1/2}\psi_{T0})(\psi_{T0}\cosh\psi_{T0}+\psi_{I0}\sinh\psi_{T0})^2}\right]e^{2j\omega t}+\cdots\end{aligned}\right\}\quad(71)$$

This result is for a given input density wave. It will be shown later that the results shown in eq 71 are only valid when the equation of condition is isothermal (i. e. the "polytropic" coefficient is unity). It therefore follows that if the input pressure wave is given by

$$\xi=\xi_0e^{j\omega t}+\xi_1e^{2j\omega t}+\cdots.\quad(72)$$

the wave at the end of the tube is

$$\left.\begin{aligned}\xi=&\left[\xi_0\frac{\psi_{T0}}{\psi_{T0}\cosh\psi_{T0}+\psi_{I0}\sinh\psi_{T0}}\right]e^{j\omega t}+\frac{[2]^{1/2}\psi_{T0}}{[2]^{1/2}\psi_{T0}\cosh[2]^{1/2}\psi_{T0}+2\psi_{I0}\sinh[2]^{1/2}\psi_{T0}}\\&\left[\xi_1+\xi_0^2\frac{\left[\begin{array}{l}\psi_{T0}^2(\cosh 2\psi_{T0}-\cosh[2]^{1/2}\psi_{T0})+[2]^{1/2}\psi_{T0}\psi_{I0}([2]^{1/2}\sinh 2\psi_{T0}-\\\sinh[2]^{1/2}\psi_{T0})+\psi_{I0}^2(\cosh 2\psi_{T0}-\cosh[2]^{1/2}\psi_{T0})\end{array}\right]}{2(\psi_{T0}\cosh\psi_{T0}+\psi_{I0}\sinh\psi_{T0})^2}\right]e^{j\omega t}+\cdots\end{aligned}\right\}\quad(73)$$

For liquids, we can start from eq 38

$$\frac{\partial}{\partial x}\left(\frac{\rho}{\mu}\frac{\partial p}{\partial x}\right)=\frac{32}{D^2}\frac{\partial\rho}{\partial t}.\quad(38)$$

By the use of eq 22 and 23, we obtain

$$\frac{\partial^2\eta^2}{\partial x^2}=\frac{2\lambda_{T0}}{L^2}\frac{\partial\eta}{\partial t},\quad(59)$$

where

$$\lambda_{T0}=\frac{AL}{V}b\lambda_0\quad(55)$$

The equation is exactly the same as before with the single modification that $1/b$ is substituted for n and m, so that our previous result (eq 73) holds.

The change in mean density along the tube can be estimated from eq 59 and 70. The equation of motion (eq 59) requires that the second derivative of the mean square density vanishes, or that the first derivative is constant. However, the end boundary condition (eq 70) requires that the first derivative of the mean square density vanishes at the end of the tube, and therefore along the entire tube, so that the mean square density and therefore the mean square pressure must remain constant along the tube. The leading part of the second order change in mean pressure arises, therefore, from the steady state portion of the square of the amplitude of the fundamental. It can be simply shown that the increase in mean pressure at the instrument is given by

$$\xi_0\Delta p[1+|\tilde{\xi}_{0L}/\xi_0|^2]/4$$

$$\eta\frac{\partial\eta}{\partial x}=-\frac{\psi_{I0}}{\omega L}\frac{\partial\eta}{\partial t}\quad(70)$$

(see eq 1, 19, 20, and 24).

The application of these two boundary conditions leads to the result that at the end of the tube

4. Theory Corrected for Acceleration

In this section, we will remove the main restrictive assumption—the assumed Poiseuille velocity distribution. In order to do this, it is necessary to go back to the equations of hydrodynamics. Since the complete theory is too extensive to be treated in this paper, we will simply state the results.

It is possible to take the Navier-Stokes equations of hydrodynamics (the equations of motion), combine them with the equation of continuity, and with the energy equation, which represents a detailed energy balance among thermal and kinetic energies, to arrive at the Kirchoff equations of sound. (See Rayleigh, Theory of sound, volume 2, article 348.) These equations are valid to first order. This procedure was followed, making no assumption as to the form of equation of state for the fluid, and the following results were obtained for the attenuation parameter, and the velocity in an infinite tube:

$$\left(\frac{\psi_T}{L}\right)^2=-\frac{\omega^2}{C^2}\frac{1+\dfrac{2(\gamma-1)J_1\left(g\dfrac{D}{2}\right)}{g\dfrac{D}{2}J_0\left(g\dfrac{D}{2}\right)}}{1-\dfrac{2J_1\left(h\dfrac{D}{2}\right)}{h\dfrac{D}{2}J_0\left(h\dfrac{D}{2}\right)}} \tag{74}$$

where

$$g\frac{D}{2}=(1-j)\frac{D}{2}\left[\frac{\omega\sigma_0}{2\nu_0}\right]^{1/2}$$

$$h\frac{D}{2}=(1-j)\frac{D}{2}\left[\frac{\omega}{2\nu_0}\right]^{1/2}$$

and

$$Q=-\frac{\pi D^2}{4j\omega\rho_0}\left(1-\frac{2J_1\left(h\dfrac{D}{2}\right)}{h\dfrac{D}{2}J_0\left(h\dfrac{D}{2}\right)}\right)\frac{\partial p}{\partial x}, \tag{75}$$

where

C is the Laplacian velocity of sound in the fluid;

g and h are arguments of the Bessel functions for unit tube radius;

J_0 and J_1 are the zeroth and first order Bessel functions;

σ_0 is the mean Prandtl number of the fluid $\left(=\dfrac{c_{p_0}\mu_0}{K_0}\right)$;

K_0 is the mean thermal conductivity of the fluid;

c_{p_0} is the mean specific heat at constant pressure of the fluid;

ν_0 is the kinematic viscosity of the fluid $\left(=\dfrac{\mu_0}{\rho_0}\right)$.

The attenuation parameter in eq 74 is to be interpreted as before (see eq 47) as the exponent in the form $e^{\pm\psi_T\frac{x}{L}}$.

Equal 64 and 65 are of doubtful value for

$$\frac{\nu_0}{CD}>1 \tag{76}$$

or

$$\frac{\nu_0\omega}{C^2}>1.$$

These restrictions are violated at high vacuum or very high frequencies.

It is instructive to evaluate eq 74 and 75 for small values of the Bessel function arguments. They become

$$\left.\begin{aligned}\left(\frac{\psi_T}{L}\right)^2&=\frac{32j\omega\nu_0\gamma}{C^2D^2}\\ Q&=-\frac{\pi D^4}{128\mu_0}\frac{\partial p}{\partial x}\end{aligned}\right\} \tag{77}$$

which are precisely the results assumed in eq 1 and 42 under the condition in eq 42 that the "polytropic" coefficient is unity. This arises because the value C^2/γ in eq 77 is the square of the Newtonian velocity of sound, which for gases is p_0/ρ_0. Eq 74 and 75, which take into account the heat conduction, thus demonstrate that, when the previous results are valid, the equation of condition is the isothermal. At higher frequencies the modifying term in eq 74 may be regarded as the "polytropic" coefficient. To bring this out explicitly, eq 74 and 75 may be written as

$$\left(\frac{\psi_T}{L}\right)^2=\frac{32j\omega\nu_0\gamma}{C^2D^2}\left[\frac{\dfrac{\left(h\dfrac{D}{2}\right)^2}{8}}{\dfrac{2J_1\left(h\dfrac{D}{2}\right)}{h\dfrac{D}{2}J_0\left(h\dfrac{D}{2}\right)}-1}\right]\left[\frac{1+\dfrac{2(\gamma-1)J_1\left(g\dfrac{D}{2}\right)}{g\dfrac{D}{2}J_0\left(g\dfrac{D}{2}\right)}}{\gamma}\right]\quad Q=-\frac{\pi D^4}{128\mu_0}\frac{\partial p}{\partial x}\left[\frac{\dfrac{2J_1\left(h\dfrac{D}{2}\right)}{h\dfrac{D}{2}J_0\left(h\dfrac{D}{2}\right)}-1}{\dfrac{\left(h\dfrac{D}{2}\right)^2}{8}}\right] \tag{78}$$

We may regard eq 78 as an extended definition of the attenuation parameter ψ_T, and as the modified velocity that replaces Poiseuilles law. It is therefore used without the zero subscript, which is used to denote the Poiseuille regime.

If we now bring in the end boundary condition, namely

$$Q=\frac{V}{mp_0}\frac{\partial p}{\partial t}, \tag{24}$$

for a gas, or

$$Q=\frac{Vb}{p_0}\frac{\partial p}{\partial t} \tag{25}$$

for a liquid, we obtain

$$\frac{d\tilde{\xi}}{dx}=-\frac{128\mu_0 Vj\omega}{\pi D^4 m p_0}\tilde{\xi}\left[\frac{\frac{\left(h\frac{D}{2}\right)^2}{8}}{\frac{2J_1\left(h\frac{D}{2}\right)}{h\frac{D}{2}J_0\left(h\frac{D}{2}\right)}-1}\right] \tag{79}$$

for a gas, or

$$\frac{d\tilde{\xi}}{dx}=-\frac{128\mu_0 Vj\omega b}{\pi D^4 p_0}\tilde{\xi}\left[\frac{\frac{\left(h\frac{D}{2}\right)^2}{8}}{\frac{2J_1\left(h\frac{D}{2}\right)}{h\frac{D}{2}J_0\left(h\frac{D}{2}\right)}-1}\right] \tag{80}$$

for a liquid.

Let

$$\chi_I=\frac{128\mu_0 V\omega L}{\pi D^4 m p_0}\left[\frac{\frac{\left(h\frac{D}{2}\right)^2}{8}}{\frac{2J_1\left(h\frac{D}{2}\right)}{h\frac{D}{2}J_0\left(h\frac{D}{2}\right)}-1}\right] \tag{81}$$

for a gas, or

$$\chi_I=\frac{128\mu_0 V\omega Lb}{\pi D^4 p_0}\left[\frac{\frac{\left(h\frac{D}{2}\right)^2}{8}}{\frac{2J_1\left(h\frac{D}{2}\right)}{h\frac{D}{2}J_0\left(h\frac{D}{2}\right)}-1}\right] \tag{82}$$

for a liquid.

We have thus corresponding extensions of our definition of χ_I to cover all frequencies. The limiting value of χ_I for small arguments obviously becomes the previous value for χ_{I0}.

Since the only modification has been to extend the definitions of ψ_T and ψ_I without changing the form of the equations to be solved (namely eq 42 and 46), the previous result (eq 49) is strictly valid. The results however are now correct for frequencies well into the audio range.

It is not possible to use the results of this section to extend the range of validity of the calculated distortion for finite pressure amplitudes. To do this rigorously would require going back to the second-order terms neglected in Kirchoff's equations, which is an extremely arduous procedure. It must therefore be concluded that the distortion calculated in section (3) is valid whenever the Poiseuille regime holds, which also means that the "polytropic" coefficient in the distortion must be taken as unity. The distortion may be validly calculated from eq 73 when

$$\frac{\omega D^2}{4\nu_0}<1, \tag{83}$$

and when the applied pressure amplitude is sufficiently small at the applied frequency (sufficiently small enough Reynolds number) to permit laminar flow.

5. Theory Corrected for Finite Length-End Effects

There is one additional factor that must be considered for completeness—the end effect. An estimate of its magnitude will be made for the Poiseuille regime. It arises from the fact that it takes an appreciable length of tubing to set up the Poiseuille velocity distribution in the transmission tube. The character of the entrance flow is that the axial velocity is flat at the entrance, gradually developing an approximately parabolic (laminar) boundary with a core of uniform velocity, until the approximately parabolic distribution fills the tube. It is evident that boundary layer theory may be used, and for our purposes an extremely crude boundary layer theory.

We go back to the equations of hydrodynamics and make the following assumptions: (1) that the entrance flow is incompressible, (2) that the variation of pressure in the radial direction is negligible in the entrance portion, (3) that quadratic terms in velocity are negligible in the boundary layer, (4) that the core of the velocity distribution is potential.

For our purposes we need only write the equations of motion for the potential core as

$$\frac{\partial u_p}{\partial t}+u_p\frac{\partial u_p}{\partial x}=-\frac{1}{\rho_0}\frac{\partial p}{\partial x}, \tag{84}$$

where u_p is the axial velocity in the potential core.

Let

$$u_p=\frac{\partial\phi}{\partial x} \tag{85}$$

where ϕ is the velocity potential

then

$$\frac{\partial}{\partial x}\left(\frac{\partial\phi}{\partial t}\right)+\frac{1}{2}\frac{\partial u_p^2}{\partial x}+\frac{1}{\rho_0}\frac{\partial p}{\partial x}=0$$

or

$$\frac{\partial\phi}{\partial t}+\frac{1}{2}u_p^2+\frac{p}{\rho_0}=f(t), \tag{86}$$

where $f(t)$ is an arbitrary function of time.

Eq (86) represents the Bernoulli integral. It can be written in the form

$$p(x,t)+\frac{1}{2}\rho_0 u_p^2=f(t)-\frac{\partial\phi(x,t)}{\partial t}. \tag{87}$$

The boundary conditions are a prescribed pressure variation at $x=0$, the entrance, with a flat velocity profile ($\overline{u}_p=\overline{u}$ where $\overline{u}$ is the average velocity across the section) and a parabolic distribution of velocity at some point $x=l$ downstream $\left(\frac{u_p}{2}=\overline{u}\right)$. The assumption of incompressible flow makes $\overline{u}$ the same at both sections. these conditions lead to the result that

$$p(0,t)=p(l,t)+\frac{3}{2}\rho_0\overline{u}^2+\frac{\partial\phi}{\partial t}(l,t)-\frac{\partial\phi(0,t)}{\partial t}. \tag{88}$$

If we now refer to the arguments given in Goldstein "Modern Developments in Fluid Mechanics," vol. 1, pp 299 to 308 for the static case, we find on p. 302 that

$$p(0)=p(l)+\frac{3}{2}\rho_0\overline{u}^2+\frac{16\rho_0\overline{u}^2}{\frac{D}{2}R_e}\left(l-.0575\frac{D}{2}R_e\right), \tag{89}$$

where R_e is the Reynolds number.

It follows from these two equations that the leading term for the entrance loss in the oscillatory case is the usual $\rho_0\overline{u}^2$ loss.

We may therefore adopt the exact static result (see p. 308 of Goldstein) that

$$p(0,t)=p(l,t)+2.41\left(\frac{1}{2}\rho_0\overline{u}^2\right)+\frac{16x}{\frac{D}{2}R_e}\rho_0\overline{u}^2, \tag{90}$$

where the last term represents the Poiseuille viscous resistance.

Therefore the effect of the entrance is to cause a pressure drop given by

$$\Delta p=\rho_0\overline{u}^2, \tag{91}$$

the exact coefficient 1.2 being unimportant for our purposes. We will regard eq 91, not as being exact, but as indicating the order of magnitude of the entrance correction.

If we substitute the Poiseuille velocity into eq (91) and evaluate the pressure gradient of the Poiseuille distribution from eq (47), we arrive at the result that the pressure excess just inside the tube ξ^1 is approximately given by

$$\xi^1=\xi_0 e^{j\omega t}-\frac{jD^2\omega}{32\,\nu_0}\left(\frac{\psi_{T0}\tanh\psi_{T0}+\psi_{I0}}{\psi_{T0}+\psi_{I0}\tanh\psi_{T0}}\right)^2\xi_0^2\,e^{2j\omega t}. \tag{92}$$

Equation 92 is the desired result. It shows that the approximate effect of the entrance is to distort each input harmonic. It can be interpreted as meaning that the effect of the entrance is the same as if it did not exist, but with the fundamental harmonic generator replaced by a fundamental and a second harmonic generator. The first-order terms are thus left unaffected, and the only equation requiring modification is the attenuated second harmonic.

If eq 92 is used as the input pressure for a pure sinusoidal input in the fluid conduit, eq 73 becomes

$$\left.\begin{aligned}\xi=\xi_0\left[\frac{\psi_{T0}}{\psi_{T0}\cosh\psi_{T0}+\psi_{I0}\sinh\psi_{T0}}\right]e^{j\omega t}+\frac{[2]^{1/2}\psi_{T0}\xi_0^2}{[2]^{1/2}\psi_{T0}\cosh[2]^{1/2}\psi_{T0}+2\psi_{I0}\sinh[2]^{1/2}\psi_{T0}}\,e^{2j\omega t}\times\\ \left[\frac{\psi_{T0}^2([1+N^2]\cosh 2\psi_{T0}-N^2-\cosh[2]^{1/2}\psi_{T0})+[2]^{1/2}\psi_{T0}\psi_{I0}([2]^{1/2}[1-N^2]\sinh 2\psi_{T0}-\sinh[2]^{1/2}\psi_{T0})+\psi_{I0}^2([1-N^2]\cosh 2\psi_{T0}-N^2-\cosh[2]^{1/2}\psi_{T0})}{2(\psi_{T0}\cosh\psi_{T0}+\psi_{I0}\sinh\psi_{T0})^2}\right]\\ +\ldots\end{aligned}\right\} \tag{93}$$

where

$$N^2=\frac{jD^2\omega}{32\,\nu_0}=-\frac{\left(h\frac{D}{2}\right)^2}{8}. \tag{94}$$

N is a dimensionless parameter.

The second term in eq 93 gives the second harmonic distortion.

Actually from the condition under which eq 93 is valid (namely eq 83), the value of N^2 must be small, so that it is a matter of indifference whether it is used in eq 93 or not, and we will therefore neglect it.

6. Summary

There only remains the task of recapitulating the pertinent results and presenting them for

computational convenience. To accomplish this some minor notational changes will be made.

In eq 49, it was shown that the complex attenuation of the fundamental is given by

$$\frac{\bar{\xi}_{OL}}{\xi_0}=\frac{\psi_T}{\psi_T\cosh\psi_T+\psi_L\sinh\psi_T}. \tag{95}$$

where ξ_{OL} is the complex amplitude of the fractional pressure excess of the fundamental at the end of the tube, and the subscript O refers to the fundamental.

In eq 93, it was shown that the complex amplitude of the second harmonic distortion due to a pure sinusoidal pressure input is given in the form of its ratio to the input amplitude of the fundamental by

$$\left(\frac{\bar{\xi}_{IL}}{\xi_0}\right)_0=\frac{\left[\begin{array}{l}\xi_0\psi_{T0}[\psi_{T0}^2(\cosh 2\psi_{T0}-\cosh [2]^{1/2}\psi_{T0})+[2]^{1/2}\psi_{T0}\psi_{I0}([2]^{1/2}\sinh 2\psi_{T0}-\\ \sinh [2]^{1/2}\psi_{T0})+\psi_{I0}^2(\cosh 2\psi_{T0}-\cosh [2]^{1/2}\psi_{T0})]\end{array}\right]}{[2]^{1/2}[\psi_{T0}\cosh\psi_{T0}+\psi_{I0}\sinh\psi_{T0}][[2]^{1/2}\psi_{T0}\cosh [2]^{1/2}\psi_{T0}+2\psi_{I0}\sinh[2]^{1/2}\psi_{T0}]}, \tag{96}$$

where $\bar{\xi}_{IL}$ is the complex amplitude of the fractional pressure excess of the second harmonic at the end of the tube; ψ_{T0} and ψ_{I0} are the values of the attenuation parameter computed on the basis of the Poiseuille velocity distribution.

In eq 76, it was shown that eq 95 is valid if

$$\left.\begin{array}{l}\dfrac{v_0}{CD}<1\\ \dfrac{v_0\omega}{C^2}<1\end{array}\right\} \tag{97}$$

In eq 83, it was shown that eq 96 is valid if

$$\frac{\omega D^2}{4\nu_0}<1 \tag{98}$$

In eq 48, the attenuation parameters were defined as

$$\left.\begin{array}{l}\psi_T^2=j\chi_T\\ \psi_I=j\chi_I\end{array}\right\} \tag{99}$$

In eq 78, 81, and 82, with slight modifications for generality, the attenuation factors were determined to be most generally

$$\left.\begin{array}{l}\chi_T=\dfrac{32\nu_0\omega}{C_T^2}\left(\dfrac{L}{D}\right)^2\left[\dfrac{1+\dfrac{2(\gamma-1)J_1\left(g\frac{D}{2}\right)}{g\frac{D}{2}J_0\left(g\frac{D}{2}\right)}}{\gamma}\right]\times\\ \qquad\left[\dfrac{\dfrac{\left(h\frac{D}{2}\right)^2}{8}}{\dfrac{2J_1\left(h\frac{D}{2}\right)}{h\frac{D}{2}J_0\left(h\frac{D}{2}\right)}-1}\right]\\ \chi_I=\dfrac{32\nu_0\omega}{C_I^2}\left(\dfrac{L}{D}\right)^2\dfrac{V}{AL}\left[\dfrac{\dfrac{\left(h\frac{D}{2}\right)^2}{8}}{\dfrac{2J_1\left(h\frac{D}{2}\right)}{h\frac{D}{2}J_0\left(h\frac{D}{2}\right)}-1}\right]\end{array}\right\} \tag{100}$$

while the attenuation factors for Poiseuille flow are

$$\left.\begin{array}{l}\chi_{T0}=\dfrac{32\nu_0\omega}{C_T^2}\left(\dfrac{L}{D}\right)^2\\ \chi_{I0}=\dfrac{32\nu_0\omega}{C_I^2}\left(\dfrac{L}{D}\right)^2\dfrac{V}{AL}\end{array}\right\} \tag{101}$$

From eq 75

$$\left.\begin{aligned} g\frac{D}{2}&=(1-j)\frac{D}{2}\left[\frac{\omega\sigma_0}{2\nu_0}\right]^{1/2}\\ h\frac{D}{2}&=(1-j)\frac{D}{2}\left[\frac{\omega}{2\nu_0}\right]^{1/2}\end{aligned}\right\} \tag{102}$$

Here C_T is the velocity of sound appropriate to the tube;

C_I is the velocity of sound appropriate to the instrument volume.

For computational purposes, the attenuation factors can be made less complicated by the introduction of two new functions.

Let

$$\left[\frac{1+\dfrac{2(\gamma-1)J_1\left(g\frac{D}{2}\right)}{g\frac{D}{2}J_0\left(g\frac{D}{2}\right)}}{\gamma}\right]\left[\frac{\dfrac{\left(h\frac{D}{2}\right)^2}{8}}{\dfrac{2J_1\left(h\frac{D}{2}\right)}{h\frac{D}{2}J_0\left(h\frac{D}{2}\right)}-1}\right] \tag{103}$$

and

$$F_2=\left[\frac{\gamma}{1+(\gamma-1)\dfrac{2J_1\left(g\frac{D}{2}\right)}{g\frac{D}{2}J_0\left(g\frac{D}{2}\right)}}\right],$$

where F_1 and F_2 are correction functions to the Poiseuille attenuation factors.

The attenuation factors then become

$$\left.\begin{aligned}\chi_T&=\frac{32\nu_0\omega}{{C_T}^2}\left(\frac{L}{D}\right)^2F_1\\ \chi_I&=\frac{32\nu_0\omega}{{C_I}^2}\left(\frac{L}{D}\right)^2\left(\frac{V}{AL}\right)F_1F_2.\end{aligned}\right\} \tag{104}$$

In order to obtain consistency with our previous results, we introduce the following definitions:

For a gas:

It can be shown both from kinetic theory and from experimental data that the value of the Prandtl number for a gas is approximately unity. Differences from unity are unimportant for our purposes Therefore g and h in eq (102) may be regarded as equal. We may therefore define F_1 and F_2 as

$$F_1\left(h\frac{D}{2},\gamma\right)=\left[\frac{1+\dfrac{2(\gamma-1)J_1\left(h\frac{D}{2}\right)}{h\frac{D}{2}J_0\left(h\frac{D}{2}\right)}}{\gamma}\right]\left[\frac{\dfrac{\left(h\frac{D}{2}\right)^2}{8}}{\dfrac{2J_1\left(h\frac{D}{2}\right)}{h\frac{D}{2}J_0\left(h\frac{D}{2}\right)}-1}\right]$$

$$F_2\left(h\frac{D}{2},\gamma\right)=\left[\frac{\gamma}{1+(\gamma-1)\dfrac{2J_1\left(h\frac{D}{2}\right)}{h\frac{D}{2}J_0\left(h\frac{D}{2}\right)}}\right]. \tag{105}$$

These functions therefore depend only on two variables, instead of three as in eq (103).

Equation 78 shows that the velocity of sound appropriate to the tube for eq 104 is the Newtonian velocity, which for a gas is $[p_0/\rho_0]^{1/2}$. Equation 81 indicates that the velocity of sound appropriate to the instrument volume for eq 104 is the "polytropic" velocity or $[mp_0/\rho_0]^{1/2}$. Therefore for a gas, the attenuation factors may be computed from

$$\left.\begin{aligned}\chi_T&=\frac{32\mu_0\omega}{p_0}\left(\frac{L}{D}\right)^2F_1\left(h\frac{D}{2},\gamma\right)\\ \chi_I&=\frac{32\mu_0\omega}{mp_0}\left(\frac{L}{D}\right)^2\left(\frac{V}{AL}\right)F_1\left(h\frac{D}{2},\gamma\right)F_2\left(h\frac{D}{2},\gamma\right)\end{aligned}\right\} \tag{106}$$

where F_1, F_2, and $h\dfrac{D}{2}$ may be computed from eq 102 and 105.

It is convenient to utilize one more variable, the ratio χ_I/χ_T, which from eq 106 has the value

$$\frac{\chi_I}{\chi_T}=\frac{1}{m}\frac{V}{AL}F_2\left(h\frac{D}{2},\gamma\right) \tag{107}$$

For a liquid:

It has been stated that γ can be satisfactorily taken as unity for a liquid. This similarly makes the functions F_1 and F_2 (see eq. 103) independent of g (or really of the Prandtl number). In that case, the definition of F_1 and F_2 for a gas (eq. 105) holds for a liquid, if γ is taken as unity. Continuity of definition is thus provided for both liquid and gas attenuation.

Equation 78 shows that the velocity of sound appropriate to the tube for eq 104 is the Newtonian velocity of sound. However, consistent with eq.

55 and 58, the Newtonian velocity must be based on the effective compressibility of the liquid and tube. From eq 82 it is seen that the velocity of sound appropriate to the instrument volume, however, is based on the real compressibility of the fluid (the difference between adiabatic, "polytropic," and isothermal compressibilities is assumed negligible). It has been assumed that the compressibility of the instrument volume is included in the definition of the effective instrument volume. It follows therefore that the attenuation factors for a liquid can be computed from

$$\left.\begin{aligned}\chi_T &= 32\mu_0 k_0 \omega \left(\frac{L}{D}\right)^2 \left(1+\frac{p_0-p_a}{p_0}\frac{1}{k_0 E S}\right) F_1\left(h\frac{D}{2},1\right)\\ \chi_I &= 32\mu_0 k_0 \omega \left(\frac{L}{D}\right)^2 \frac{V}{AL} F_1\left(h\frac{D}{2},1\right) F_2\left(h\frac{D}{2},1\right)\\ \frac{\chi_T}{\chi_I} &= \frac{V}{AL}\left(\frac{1}{1+\frac{p_0-p_a}{p_0}\frac{1}{k_0 E S}}\right) F_2\left(h\frac{D}{2},1\right)\end{aligned}\right\} \quad (108)$$

and

$$\left.\begin{aligned}\chi_{T0} &= 32\mu_0 k_0 \omega \left(\frac{L}{D}\right)^2 \left(1+\frac{p_0-p_a}{p_0}\frac{1}{k_0 E S}\right)\\ \chi_{I0} &= 32\mu_0 k_0 \omega \left(\frac{L}{D}\right)^2 \frac{V}{AL}\end{aligned}\right\} \quad (109)$$

It is now possible to compute the real attenuation and lagging phase angle for the first and second harmonics. If the attenuation parameters in eq 95 are regarded as the low frequency parameters based on the Poiseuille distribution (i. e. the ones with zero subscripts), then the real attenuation and lagging phase angle can be computed from

$$\left.\begin{aligned}\left|\frac{\xi_{OL}}{\xi_0}\right|_0 &= \left[\frac{2}{\begin{aligned}&\cosh[2\chi_{T0}]^{1/2}+\cos[2\chi_{T0}]^{1/2}+\left(\frac{\chi_{I0}}{\chi_{T0}}\right)[2\chi_{T0}]^{1/2}(\sinh[2\chi_{T0}]^{1/2}-\\ &\sin[2\chi_{T0}]^{1/2})+\left(\frac{\chi_{I0}}{\chi_{T0}}\right)^2\chi_{T0}(\cosh[2\chi_{T0}]^{1/2}-\cos[\chi_{T0}]^{1/2})\end{aligned}}\right]\\ (\tan\delta_O)_0 &= \frac{\tanh\left[\frac{\chi_{T0}}{2}\right]^{1/2}\tan\left[\frac{\chi_{T0}}{2}\right]^{1/2}+\left(\frac{\chi_{I0}}{\chi_{T0}}\right)\left[\frac{\chi_{T0}}{2}\right]^{1/2}\left(\tanh\left[\frac{\chi_{T0}}{2}\right]^{1/2}+\tan\left[\frac{\chi_{T0}}{2}\right]^{1/2}\right)}{1+\left(\frac{\chi_{I0}}{\chi_{T0}}\right)\left[\frac{\chi_{T0}}{2}\right]^{1/2}\left(\tanh\left[\frac{\chi_{T0}}{2}\right]^{1/2}-\tan\left[\frac{\chi_{T0}}{2}\right]^{1/2}\right)}\end{aligned}\right\} \quad (110)$$

The zero subscript means that these are the values for the Poiseuille flow regime. Graphs of these equations are quite useful for computing attenuation. Since χ_{T0} is proportional to frequency (see eq 101), while χ_{I0}/χ_{T0} is proportional to the ratio of instrument volume to line volume (see eq 107), a family of curves of attenuation or phase angle plotted against χ_{T0} for different values of χ_{I0}/χ_{T0} are frequency response curves for different volume ratios. These curves are presented as figures 2 and 3.

At higher frequencies, where the functions F_1 and F_2 take on values appreciably different from unity, the expressions become extremely complicated. It is therefore of utility to examine their high frequency behavior.

At high frequency, we will use the approximation

$$\frac{2J_1(y)}{yJ_0(y)} = \frac{1}{y^2} - \frac{2j}{y} \quad (111)$$

If we define a new parameter $z\left(\text{related to } h\frac{D}{2}\right)$, which characterizes the fluid regime, as

$$z = \frac{D^2\omega}{4\nu_0}, \quad (112)$$

a frequency parameter $\omega L/C$, where

$$\frac{\omega L}{C} = \left[\frac{\chi_{T0}z}{8\gamma}\right]^{1/2}, \quad (113)$$

and a volume ratio R defined as

$$R = \gamma\frac{\chi_{I0}}{\chi_{T0}}, \quad (114)$$

it can be shown that at high frequency

$$\left|\frac{\tilde{\xi}_{OL}}{\xi_0}\right|=\left[\frac{2}{1+\cos\frac{2\omega L}{C}-R\left(\frac{2\omega L}{C}\right)\sin\frac{2\omega L}{C}+\frac{R^2}{4}\left(\frac{2\omega L}{C}\right)^2\left(1-\cos\frac{2\omega L}{C}\right)}\right]^{1/2}$$

$$\tan\delta_O=\left[\frac{\gamma\chi_{T0}}{16}\right]^{1/2}\frac{\left(1+R\frac{2-\gamma}{\gamma}\right)\tan\frac{\omega L}{C}+R\frac{\omega L}{C}}{1-R\frac{\omega L}{C}\tan\frac{\omega L}{C}}. \tag{115}$$

This is the solution for the undamped acoustic resonance of a tube and instrument.

In computing these quantities in eq 115, it is assumed that χ_{T0} is smaller than $\chi_{T0}\,z_a$, or that χ_{T0} is small compared to $\omega L/C$. In the solution for the undamped case, the phase angle lag is usually regarded as zero up to the first resonance. However, the given expression permits first-order computation of the phase angle lag valid for values of χ_{T0} small compared to $\omega L/C$, even though the overshoot is given as undamped. Practically, this means for values of $\left[\frac{\gamma\chi_{T0}}{16}\right]^{1/2}$ of the order of one or less.

These quantities are presented in figures 6 and 7. It can be shown that they are valid for values of $z\geq 100$, whereas the low frequency curves (figs. 2 and 3) are valid for $z\leq 1$ (see eq 98). We will state without proof that the parameter z, which characterizes the flow regime, is closely related to a damping coefficient. Figures 2 and 3 will therefore be referred to as the large damping curves, and figures 6 and 7 will be referred to as the undamped curves.

Unfortunately, in many instances, a knowledge of the highly damped behavior (figs. 2 and 3) and the undamped behavior is not sufficient. Curves have therefore been drawn for a value of z about "half-way" between 1 and 100, namely $z=6.25$ (see figs. 4 and 5). In order to preserve a scale proportional to frequency, the quantity χ_{T0} is used as abscissa.

These curves were computed from the formulas

$$\left|\frac{\tilde{\xi}_{OL}}{\xi_0}\right|=\left[\frac{2}{\cosh 2c_1+\cos 2c_2+2c_3\sinh 2c_1-2c_4\sin 2c_2+(c_3^2+c_4^2)(\cosh 2c_1-\cos 2c_2)}\right]^{1/2}$$

$$\tan\delta_O=\frac{\tanh c_1\tan c_2+c_3\tan c_2+c_4\tanh c_1}{1+c_3\tanh c_1-c_4\tan c_2} \tag{116}$$

where

$$c_1=[1-\sin c_5]^{1/2}\left[\frac{\chi_{T0}}{2}|F_1|\right]^{1/2}$$

$$c_2=[1+\sin c_5]^{1/2}\left[\frac{\chi_{T0}}{2}|F_1|\right]^{1/2}$$

$$c_3=(\cos c_6[1-\sin c_5]^{1/2}-\sin c_6[1+\sin c_5]^{1/2})\left[\frac{\chi_{T0}}{2}|F_1|\right]^{1/2}\frac{\chi_{I0}}{\chi_{T0}}|F_2|$$

$$c_4=(\cos c_6[1+\sin c_5]^{1/2}-\sin c_6[1-\sin c_5]^{1/2})\left[\frac{\chi_{T0}}{2}|F_1|\right]^{1/2}\frac{\chi_{I0}}{\chi_{T0}}|F_2|$$

$$F_1=f_1+g_1 j$$

$$F_2=f_2+g_2 j$$

$$\cos c_5=\frac{f_1}{|F_1|}$$

$$\sin c_5 = \frac{g_1}{|F_1|}$$

$$\cos c_6 = \frac{f_2}{|F_2|}$$

$$\sin c_6 = \frac{g_2}{|F_2|}$$

Equation 116 is valid at all frequencies, and is presented without further explanation for completeness and the use of those with great computational fortitude.

The amplitude ratio and leading phase angle (angle of lead on the time scale of the fundamental where both the fundamental and double frequency waves are cosine terms) of the double frequency distortion at low frequencies (neglecting the end effect) are presented in figures 8 and 9. The formula used in their computation was

$$\frac{1}{\xi_0}\left(\frac{\tilde{\xi}_{IL}}{\xi_0}\right) = \frac{1}{2}\left(\frac{\tilde{\xi}_{OL}}{\xi_0}\right)^2\left(\frac{c_1+jc_2}{c_3+jc_4}\right), \qquad (117)$$

where

$$c_1 = \cosh [2\chi_{T0}]^{1/2} \cos [2\chi_{T0}]^{1/2} - \cosh [\chi_{T0}]^{1/2} \cos [\chi_{T0}]^{1/2} + \frac{\chi_{I0}}{\chi_{T0}} [\chi_{T0}]^{1/2}([2]^{1/2} \sinh [2\chi_{T0}]^{1/2} \cos [2\chi_{T0}]^{1/2} -$$

$$[2]^{1/2} \cosh [2\chi_{T0}]^{1/2} \sin [2\chi_{T0}]^{1/2} - \sinh [\chi_{T0}]^{1/2} \cos [\chi_{T0}]^{1/2} + \cosh [\chi_{T0}]^{1/2} \sin [\chi_{T0}]^{1/2}) +$$

$$\left(\frac{\chi_{I0}}{\chi_{T0}}\right)^2 \chi_{T0}(-\sinh [2\chi_{T0}]^{1/2} \sin [2\chi_{T0}]^{1/2} + \sinh [\chi_{T0}]^{1/2} \sin [\chi_{T0}]^{1/2})$$

$$c_2 = \sinh [2\chi_{T0}]^{1/2} \sin [2\chi_{T0}]^{1/2} - \sinh [\chi_{T0}]^{1/2} \sin [\chi_{T0}]^{1/2} + \frac{\chi_{I0}}{\chi_{T0}} [\chi_{T0}]^{1/2} ([2]^{1/2} \sinh [2\chi_{T0}]^{1/2} \cos [2\chi_{T0}]^{1/2} +$$

$$[2]^{1/2} \cosh [2\chi_{T0}]^{1/2} \sin [2\chi_{T0}]^{1/2} - \sinh [\chi_{I0}]^{1/2} \cos [\chi_{I0}]^{1/2} - \cosh [\chi_{I0}]^{1/2} \sin [\chi_{I0}]^{1/2}) +$$

$$\left(\frac{\chi_{I0}}{\chi_{T0}}\right)^2 \chi_{T0} (\cosh [2\chi_{T0}]^{1/2} \cos [2\chi_{T0}]^{1/2} - \cosh [\chi_{T0}]^{1/2} \cos [\chi_{T0}]^{1/2})$$

$$c_3 = \cosh [\chi_{T0}]^{1/2} \cos [\chi_{T0}]^{1/2} + \frac{\chi_{I0}}{\chi_{T0}} [\chi_{T0}]^{1/2}(\sinh [\chi_{T0}]^{1/2} \cos [\chi_{T0}]^{1/2} - \cosh [\chi_{T0}]^{1/2} \sin [\chi_{T0}]^{1/2})$$

$$c_4 = \sinh [\chi_{T0}]^{1/2} \sin [\chi_{T0}]^{1/2} + \frac{\chi_{I0}}{\chi_{T0}} [\chi_{T0}]^{1/2}(\sinh [\chi_{T0}]^{1/2} \cos [\chi_{T0}]^{1/2} + \cosh [\chi_{T0}]^{1/2} \sin [\chi_{T0}]^{1/2})$$

The author expresses his appreciation to D. P. Johnson for his assistance in the mathematical development.

Washington, August 2, 1949.